The dark side of the Universe

Ph.D. Thesis
Scuola di Dottorato "Vito Volterra" - XXVII ciclo

University of Rome *La Sapienza*

Candidate: Najla Said

Supervisor: Prof. A. Melchiorri
Coordinator: Prof. R. Capuzzo Dolcetta

To my beloved family

'...Finally I've found that I belong here...'

Depeche Mode - Home

Contents

Introduction

The knowledge of the Universe surrounding us, nevertheless the big steps forward of the last decade, presents a lot of obscure or not well understood parts, that are usually indicated with the adjective *dark*. These parts touch every component of the Universe: we have well known radiation in form of photons, and its dark counterpart in form of neutrinos, dark matter beside the ordinary (baryonic) matter and also an obscure form of energy whose nature is completely unknown.

In this context the big challenge of the next generation cosmology is to determine the intrinsic properties of these exotic components by working on available observables and by determining new ways to look at our Universe. Astrophysicists and Cosmologists developed during the years different techniques to observe the sky, some of which focus on the static properties of the Universe (distances and topology, actual composition), while others point towards a description of its dynamics (evolution of the components' perturbations, expansion of the background and so on).

Nowadays measuring distances and in this way the geometry of the Universe represents quite a trivial task, given the years of observations and data analysis in this field. It is worth noticing, indeed, that a major complication of the cosmological research is to reliably reduce the data obtained by the observations and robustly analyse them in a statistical prospective. We cannot reproduce the Universe itself, so it is important to determine optimal ways to collect data and analyse them, keeping in account the fact that we are not working in laboratory, well-controlled experiments, but that different effects can merge in different observations and in a certain sense obscure or bias the properties or characteristics that we are looking for.

Another milestone of the cosmological research is the study of the Cosmic Microwave Background (CMB). This particular observable contains indeed both statical and dynamical information on the Universe as a whole and on its particular components and, maybe much surprising, can tell us about Universe's primordial epoch, when everything was in form of plasma, and about present time, when each component developed its own story and evolution.

The efforts on observing at best the CMB have been one of the crucial point of last years of cosmological research, culminated recently with the results obtained from the Planck experiment, capable of measuring this radiation at a precision mostly limited by statistical arguments than by experimental limits.

As we will see in detail in this thesis, the general relativity that rules the Universe evolution works in such a way to link statical and dynamical behaviour. This feature gives the Cosmologists the possibility to infer dynamical properties starting from simple geometrical measurements, and this, in last analysis, leads to development of new techniques to study directly also the evolutionary part of the Cosmo. We already have some measurements of this kind, but the best is to come with recently developed experiments that started in the last couple of years or that should start soon. This kind of observations will concentrate on precise and complete dynamical data that hopefully will lead us to comprehend also the darkest part of our knowledge: the dark energy.

My Ph.D. work has been principally focused on the study of the properties of the *dark sector* of the Universe using all probes actually available. In the first Chapter, after a brief introduction on general cosmology, I will present the state of art of the research, namely the standard ΛCDM model, with its lights and shadows, and the observables I have used for my research.

In the second Chapter I will focus on the dark sector itself, presenting each component and its impact on the overall behaviour of the Universe.

Chapter three will be dedicated to the analysis methods used, introducing Bayesian inference, Monte-Carlo Markov Chains (MCMC) methods and Principal Component Analysis (PCA).

The fourth Chapter will present my research about dark radiation: I will expose results on its general and specific properties, obtained using different aspect of its behaviour, namely its interaction in the primordial plasma imprinted in the CMB and strongly related with other CMB features, and its fundamental role in the formation of the light chemical elements of our Universe, in a process known as Big Bang Nucleosynthesis (BBN).

Chapter five will instead be focused on my research on dark energy, in particular on its possible time evolution, right now the best way to make assumption on its nature. I used the PCA to decorrelate information on the equation of state of dark energy at different epochs, in order to understand how likely are a constant or an evolutionary behaviour.

Finally the sixth Chapter will be dedicated to my research on possible interaction between dark energy and dark matter, a promising model that in principle can explain some awkward aspects of our Universe (coincidence

problem), and can give reason of some inconsistencies among late and recent time observations. Beside an introductory work on some theoretical models, I performed a parametric analysis that led to the identification of a best fit model, on which several consistency tests were applied. Finally I will drop my conclusions and expectations for the future.

As last word of this introduction I would like to state that a lot of my work has been devoted also for the Planck experiment. As part of the Low Frequency Instrument (LFI) Core Team and of the Cosmological Parameter Group, I worked actively on the likelihood validation and testing and the data analysis. Unfortunately, I cannot disclose any of these results before the official Planck release.

Chapter 1

A brief overview

'...If I told you that I knew about the sun and the moon,
I'd be untrue,
The only thing I know for sure
Is what I wanna do...'

Queens of the Stone Age - Make it wit chu

1.1 Cosmology

Standard cosmology is founded on a fundamental principle, the *cosmological principle* indeed: the Universe is homogeneous and isotropic at large scales ($> 100Mpc$). This simple sentence can reduce the complexity of the study of the Universe at high degree. Working in a homogeneous and isotropic environment, at least for what concerns the large scales, makes indeed the calculations straightforward and simplifies extremely also the interpretation and comprehension of the theory. This clearly does not mean that the principle was chosen ad hoc to make things easy. The observable Universe, and in particular the CMB, agrees with this principle, showing us a picture in which peculiarity are meaningful only at small scales. One of the most important implications of this principle is the that we can consider different areas of the sky that we observe as different statistical realizations of the Universe itself, giving us the fundamental possibility to use a statistical approach at large scales.

1.1.1 The Big Bang Theory

The theory of the Big Bang is right now quite overall accepted [1]. The presence of the CMB itself, the expansion the Universe is undergoing, and

the precise predictions of the BBN about the primordial abundance of the light elements, all concur to indicate the Big Bang as the starting point of our Universe. The idea is that everything starts from a singularity, a dimensionless point in which all the content of the Universe was condensed. At the beginning of time (and space) this singularity starts to expand, giving rise after billions of years to the Universe that we know. All that concerns the Big Bang and the very early times of the Universe is unknown. It regards such small spatial scales and such high energy scales that quantum and relativistic effects are bound together, and still we do not have a comprehensive theory to study this kind of physics.

The Universe was born in a very small, dense and hot state in which the very fundamental particles (quarks and leptons as far as we know) interact with each other at high rate. As the expansion goes on, and as the temperature lowers, high-energy interactions among particles begin to disappear. In this way strong interactions fade and quarks remain bound in baryons[1]. In this plasma made on of baryons and leptons (and their antimatter counterparts), the photons generated by their interactions are strongly scattered, so that they cannot stream away. The result is that they cannot reach us and carry information on what is going on there, making that primordial age of the Universe for us is simply not observable. The Universe is said to be *optically thick*. When all the baryons annihilate the anti-baryons and the relic of matter starts to form atomic nuclei we are in the middle of the BBN process. Finally, when the temperature lower further, the nuclei and the electrons merge to form neutral atoms, making finally possible for the photons to stream freely and reach us. This epoch is called *recombination*, the Universe is now *optically thin* and its picture of this epoch is exactly the image that we see observing the CMB.

1.1.2 The Friedmann equations

The Universe obeys the laws of general relativity, and to study its evolution we need to define a metric that represents a four-dimensional expanding space-time, homogeneous and isotropic. This kind of metric was proposed by Friedmann, Lemaitre, Robertson and Walker (FLRW) and its line element can be written:

$$ds^2 = g_{\mu\nu} dx^\mu dx^\nu = -dt^2 + a(t)^2 d\sigma^2 \tag{1.1}$$

[1] In equilibrium conditions, the conservation of the CP symmetry (Charge conjugation Parity symmetry) requires that particles and antiparticles are created together, and annihilate each other. The reason why the annihilation gave rise to a matter relic is one of the most important question of modern cosmology, known as the *baryonic asymmetry*, cfr. [2].

where $a(t)$ is the scale parameter that encodes the expansion and

$$d\sigma^2 = \gamma_{ij}dx^i dx^j = \frac{dr^2}{1-Kr^2} + r^2(d\theta^2 + sin^2\theta d\phi^2) \tag{1.2}$$

is the standard expression for a three-dimensional metric characterized by a curvature K, which values $0, +1, -1$ indicates respectively a flat, closed or open space.

This metric is used to solve the Einstein equations in this particular framework. The Ricci tensor is given by:

$$R_{\mu\nu} = \Gamma^{\alpha}_{\mu\nu,\alpha} - \Gamma^{\alpha}_{\mu\alpha,\nu} + \Gamma^{\alpha}_{\mu\nu}\Gamma^{\beta}_{\alpha\beta} - \Gamma^{\alpha}_{\mu\beta}\Gamma^{\beta}_{\alpha\nu} \ . \tag{1.3}$$

where the $\Gamma^{\mu}_{\nu\lambda}$ are the Christoffel symbols obtained from the FLRW metric. From the Ricci tensor one obtains the Einstein tensor in this way:

$$G_{\mu\nu} = R_{\mu\nu} - \frac{1}{2}g_{\mu\nu}R \tag{1.4}$$

where R is the scalar curvature. At this point you can solve the Einstein equation[2]:

$$G^{\mu}_{\nu} = 8\pi G T^{\mu}_{\nu} \ . \tag{1.5}$$

The components of the equation are [3]:

$$G^0_0 = -3\Big(H^2 + \frac{K}{a^2}\Big)$$

$$G^0_i = G^i_0 = 0$$

$$G^i_j = -3\Big(H^2 + 2\dot{H} + \frac{K}{a^2}\Big)\delta^i_j \ .$$

where I introduced the Hubble parameter H representing the ratio between the temporal derivative of the scale factor and the scale factor itself.

The energy-momentum tensor of the matter is that of a perfect fluid

$$T^{\mu}_{\nu} = (\rho + P)u^{\mu}u_{\nu} + P\delta^{\mu}_{\nu} \tag{1.6}$$

where $u^{\mu} = (-1, 0, 0, 0)$ is the fluid four-velocity in co-moving coordinates and the tensor components are $T^0_0 = -\rho$ and $T^i_j = P\delta^i_j$.

Using the temporal component of the Einstein equation we obtain the *I Friedmann equation*:

$$H^2 = \left(\frac{\dot{a}}{a}\right)^2 = \frac{8\pi G}{3}\rho - \frac{K}{a^2} \tag{1.7}$$

[2]The gravitational constant is $G = 1/m^2_{pl}$ where $m_{pl} = 1.2211 \cdot 10^{19} GeV$ is the Planck mass.

while using the others we find the *II Friedmann equation*:

$$\frac{\ddot{a}}{a} = -\frac{4\pi G}{3}(\rho + 3P) \ . \tag{1.8}$$

Starting from these two relations we can obtain the continuity equation for a perfect fluid:

$$\dot{\rho} + 3H(\rho + P) = 0 \ . \tag{1.9}$$

1.1.3 Hubble law and red-shift

It is time to define one of the fundamental quantity for cosmology: the red-shift. Looking at emission and absorption lines of known chemical elements present in the light spectra of distant objects one can see an interesting fact. The central wavelength of these lines seems to be shifted towards the red part of the spectrum with respect to its position as observed in laboratory, and much important, this shift is proportional to the distance of the object observed.

This is a direct consequence of the relativistic expansion of the Universe. We can see it in this way: as light travels, the space-time expands and the wavelength of the radiation is kind of stretched. This in turn means that radiation loses part of its energy travelling in an expanding space-time. This is also the reason why we see the photons of the CMB today at a temperature of about ~ 2.7 K nevertheless they come from an epoch of the Universe in which the mean temperature was about ~ 3000 K.

The red-shift is expressed by this formula:

$$z = \frac{\lambda_0 - \lambda}{\lambda} = \frac{a_0 - a}{a} \tag{1.10}$$

and if we are dealing with velocities (between us and the source) much lower than the speed of light c ($z \ll 1$) we can use the Doppler effect approximation, obtaining:

$$\lambda_0 \sim \Big(1 + \frac{v}{c}\Big)\lambda \quad \rightarrow \quad z \sim \frac{v}{c} \ .$$

Parametrizing distances with a co-moving, constant distance multiplied by the scale factor ($\vec{r} = a(t)\vec{x}$) and time deriving, we get a line of sight velocity that is sum of two terms: one refers to the whole Universe expansion, and the other to the peculiar velocity of the object.

$$v = Hr + \frac{\vec{v_p} \cdot \vec{r}}{r} \ .$$

In the limit of small and negligible peculiar velocities one obtains the *Hubble law*:

$$v = H_0 r \tag{1.11}$$

where H_0 is the Hubble constant, the present value of the Hubble parameter $H(t)$ introduced in previous section[3]. The Hubble constant is another fundamental number of cosmology; starting from its value one can determine approximate estimates of age, observable radius and mean density of the Universe.

1.1.4 Evolution of the components

To study the fundamental properties of the components of the Universe we need to familiarize with the concept of Equation of State (EOS). To well parametrize the behaviour of a perfect fluid one can use the EOS, namely the ratio among pressure and density of the fluid:

$$w_x = \frac{P_x}{\rho_x} \ . \tag{1.12}$$

Our universe underwent different dynamical epochs, in each of which its evolution was principally dominated by the evolution of a particular component, the predominant one. The evolution of each component with respect to the scale factor can be determined using the continuity equation 1.9. substituting its density as the total one $\rho(a)$ in the first Friedmann equation 1.7:

$$\rho_x \propto a^{-3(1+w_x)} \ . \tag{1.13}$$

This leads us to determine also the evolution of the scale factor with respect to time:

$$a \propto t^{\frac{2}{3(1+w_x)}} \ . \tag{1.14}$$

where w_x is the EOS of the dominant component of the Universe in the specific epoch. This means that the expansion of the Universe changes in time accordingly to the behaviour of the dominating component. The composition of the Universe, so, drives its evolution, as Einstein equation implicitly states.

From the prospective of the EOS we can distinguish between 3 Universal components: relativistic particles (photons and neutrinos), non relativistic particles (ordinary and dark matter) and dark energy. The relativistic part (radiation) is characterized by an EOS of $w_r = 1/3$, it dominated the first epoch of the Universe (radiation era) and now represents a negligible part of the total. The non relativistic part (matter) is instead described by an

[3]This only holds for $z \ll 1$.

EOS of $w_m \sim 0$, that leads to a matter domination of the Universe (matter era) after the radiation one. The present value of the matter density is of the same order of the dominant component of our time: the dark energy. Characterized by an unknown EOS, that should be not too distant from $w_v = -1$ at least recently, the dark energy is the most important and less known component of the present day Universe.

1.2 The ΛCDM model

The standard model of modern cosmology is the so-called ΛCDM model. Starting from different measurements of different observables research has pointed to a concordance model that can more or less reproduce all cosmological data available until now. Before going into detail we should however recall some conventions.

Densities in cosmology are usually expressed with an dimensionless parameter Ω_x that represents the ratio between the density of the species ρ_x and the so-called critical density $\rho_{c,0}$, namely the density needed to have a flat Universe:

$$\rho_{c,0} = \frac{3H_0^2}{8\pi G} = 1.88h^2 \cdot 10^{-29} g\ cm^{-3}\ .$$

We will distinguish among the general density parameter of a species $\Omega_x(a)$, that is function of the scale factor, and its present value that will be indicated as $\Omega_{x,0}$, as in the case for the Hubble parameter $H(a)$ and the Hubble constant H_0. In ΛCDM model, the Universe is well represented by a set of 6 cosmological parameters:

$\Omega_{c,0}$ the density parameter of the cold dark matter present in the Universe;

$\Omega_{b,0}$ the density parameter of the baryons;

H_0 the value of the Hubble constant;

z_{re} the red-shift at which global re-ionization of the Universe started;

n_s the spectral index of the primordial perturbation spectrum;

A_s the normalization of the primordial perturbation spectrum.

These parameters carry some implicit assumptions: dark matter is cold, reionization can be thought as instantaneous, the primordial spectrum of the fluctuations is a power law. As we can see densities are expressed only for matter (ordinary and dark). This comes from the fact that the ΛCDM is a

flat model. $\Omega_{tot,0}$ is indeed the ratio between the total density and the critical density today, so for a flat Universe $\Omega_{tot,0} = 1$. Given that radiation density is negligible at present, the only other component is dark energy, whose value is equal to $1 - \Omega_m$. The fact that dark energy is identified by its sole density implies another fact: dark energy is a cosmological constant, characterized by an EOS always equal to -1. The cosmological constant is identified with the letter Λ, and from here the name of the model.

What about the values of these parameters? For the densities we find that a 5% of the total in form of ordinary matter, a 25% in form of dark matter and finally a 70% in form of cosmological constant. In practise the 95% of our Universe is unobserved: its existence has never been proved directly, but inferred from other evidences. Fig.1.1 sketches the values measured for these densities by WMAP and Planck, the two fundamental dataset of CMB spectrum.

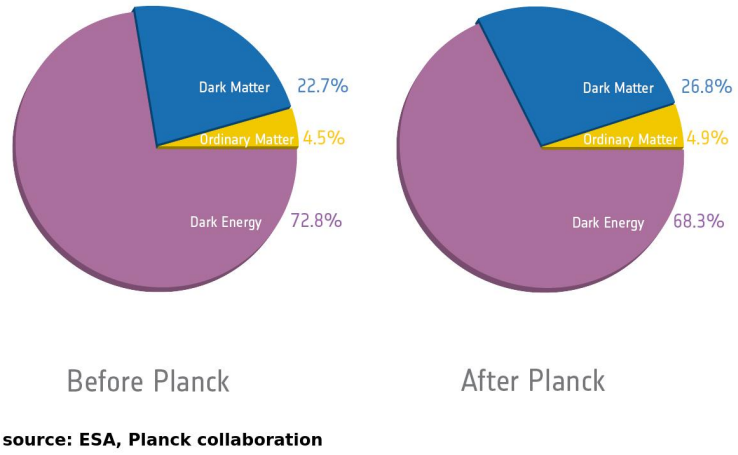

Figure 1.1: The plot shows the values of the densities of baryons, dark matter and dark energy in our Universe. On the left results from WMAP 9 years [4] are reported, on the right values from Planck [5].

For what concerns the value of the other parameters the Hubble constant is something around 70 km/s/Mpc[4], the re-ionization red-shift should be around $z = 10$, and the primordial spectrum spectral index is about $n_s = 0.96$, a little lower than the unity value that makes it scale-independent.

[4] H_0 is one of the more debated parameters in that its value is much higher if measured by local observations with respect to the one derived from CMB analysis.

In general the ΛCDM offers a simple model that fit well with the observations. With present datasets, however, the Bayesian approach cannot completely rule out some *extensions* of this model (dark energy models different from the cosmological constant and modified gravity theories, non-standard neutrino scenario, higher-order scale dependence of the primordial power spectrum, tensor modes, iso-curvature modes for different species, non standard dark matter behaviour and so on [6]). ΛCDM model is the preferred in that is the simpler, as Bayesian analysis states.

Recently, with the precision of the observations getting better and better, some inconsistencies came into light, in particular the discrepancy between clustering measurements from local Universe and clustering prediction derived from the CMB following the standard ΛCDM evolution [7, 9, 8]. We will look at some of this weaknesses in the last three sections of this thesis.

1.3 Observables

After this brief review of the most important laws and properties of cosmology I list the observables that will be used in this work.

1.3.1 Distance measurements

The word distance in cosmology has not a trivial meaning. We can indeed define different types of distance measures, that directly relate to different types of observables. I start by defining the line element of the 3D space with curvature K as the variable χ:

$$d\sigma^2 = d\chi^2 + (f_k(\chi))^2(d\theta^2 + sin^2\theta d\phi^2) \tag{1.15}$$

that relates to the r of equation 1.2 in this way:

$$r = \begin{cases} sin\chi & K = +1 \\ \chi & K = 0 \\ sinh\chi & K = -1 \end{cases}$$

and $f_k(\chi)$ is:

$$f_k(\chi) = \frac{1}{\sqrt{-K}} sinh(\sqrt{-K}\chi) \ . \tag{1.16}$$

Using this parametrization we can easily define the following distances.

- Co-moving distance
  Is referred to a light ray that travels along χ and satisfies the geodetic equation:
  $$ds^2 = -c^2dt^2 + a(t)^2d\chi^2 = 0 \ .$$

If the light is emitted at $t = t_1$ and $\chi = \chi_1$ and received at $t = t_0$ and $\chi = 0$, integrating on $d\chi$ we obtain d_c:

$$d_c = \chi_1 = \int_0^{\chi_1} d\chi = -\int_{t_0}^{t_1} \frac{cdt}{a(t)} \,.$$

Recalling the red-shift definition of 1.10 one ends up with:

$$d_c = \frac{c}{a_0 H_0} \int_0^z \frac{dz'}{E(z')} \,. \tag{1.17}$$

The function $E(z)$ encloses the importance of distance measurements for cosmological research. Its form is:

$$E^2(z) = H^2(z)/H_0^2 = \\ = \left[\Omega_{r,0}(1+z)^4 + \Omega_{m,0}(1+z)^3 + \Omega_{DE,0}\, e^{\int_0^z \frac{3(1+w_{DE})}{1+z} dz} + \Omega_k(1+z)^2\right] . \tag{1.18}$$

As we can see, it contains the density parameters of all the components of the Universe: radiation, matter, dark energy and curvature (for which we can define an effective density). Tracking how the distance depends on the red-shift we are able to make predictions about the composition of our Universe.

- Luminosity distance
  This distance comes from the relation between the absolute luminosity L of a source and the flux Φ received at a distance d_L:

$$d_L^2 = \frac{L}{4\pi\Phi} = (a_0 f_k(\chi))^2 \frac{L}{L_0} \tag{1.19}$$

because the flux received is related to the observed luminosity L_0 in this way:

$$\Phi = \frac{L_0}{S} = \frac{L_0}{4\pi(a_0 f_k(\chi))^2} \tag{1.20}$$

with S the area of the sphere centred in $z = 0$. Given that the energy ΔE_1 is emitted in the time interval Δt_1, it follows that the emitted luminosity is $L = \Delta E_1/\Delta t_1$. Similarly the observed luminosity is defined as $L_0 = \Delta E_0/\Delta t_0$. The red-shift lets us calculate the energy loss of a photon emitted at $z = z_1$ and received at $z = 0$:

$$\frac{\Delta E_1}{\Delta E_0} = \frac{\lambda_0}{\lambda_1} = 1 + z \,.$$

Imposing the conservation of the speed of light c:

$$c = \frac{\lambda_1}{\Delta t_1} = \frac{\lambda_0}{\Delta t_0}$$

and putting all together we find:

$$\frac{L}{L_0} = \frac{\Delta E_1 \Delta t_0}{\Delta E_0 \Delta t_1} = (1+z)^2$$

that lets us define the luminosity distance:

$$d_L = a_0 f_k(\chi)(1+z) \ . \tag{1.21}$$

substituting $f_k(\chi)$ from 1.16, we find:

$$d_L = \frac{c(1+z)}{H_0\sqrt{\Omega_{k,0}}} sinh\left(\sqrt{\Omega_{k,0}} \int_0^z \frac{dz'}{E(z')}\right) \tag{1.22}$$

In flat space the formula simplifies in:

$$d_L = \frac{c(1+z)}{H_0} \int_0^z \frac{dz'}{E(z')} \ . \tag{1.23}$$

- Angular diameter distance
  This distance is related to the observation of extended objects, whose dimension is measurable. We define the real dimension of the object Δx, and $\Delta\theta$ the angle that it subtends. Identifying χ as the radius of the sphere centred on the observer, with the object on its surface, we can compute the distance in this way:

  $$d_A = \frac{\Delta x}{\Delta \theta} \ . \tag{1.24}$$

  The effective dimension at the time of emission t_1 is:

  $$\Delta x = a(t_1) f_k(\chi) \Delta\theta \ . \tag{1.25}$$

  It is easy now to compute d_A and its relation with d_L:

  $$d_A = a(t_1) f_k(\chi) = \frac{d_L}{(1+z)^2} \ . \tag{1.26}$$

  For low red-shifts the two distances d_L and d_A coincide.

The distances we just defined are useful to be used with objects known as *standard candles* and *standard rulers*.

Supernovae Ia Supernovae Ia (SN) are the most used standard candles. SN events are explosive disruptions of very massive stars. Starting from different mechanisms of accretion and collapse these events can be classified in several categories [10, 11, 12]. The one of great importance for cosmology is the Ia subclass, because all the SN of this category have the same absolute luminosity at their peak[5]. The high luminosity of these events, then, makes it possible to see them at very high distances, allowing to measure distances up to $z \sim 1.4$.

With this information, remembering the form of the function $E(z)$ in 1.18 we can try to determine what composes the Universe and in which amount. In Fig.1.2 we report the typical evolution of the luminosity distances in our Universe as mapped by the SN of the Union2 compilation [15]. Left panel of Fig.1.3 shows the expected behaviour for the luminosity distance in the standard model of the Universe (with a 70% of the total composition made up of dark energy) in comparison with the one expected for a Universe with no dark energy at all and 100% of matter.

Baryonic Acoustic Oscillations The Baryonic Acoustic Oscillations (BAO) are a fundamental feature of the matter spectrum of the Universe. With a method analogous to the one used to compute the CMB power spectrum (well explained in next section), we can determine the correlation function of the matter density field of the Universe [16, 17]. Poorly speaking, one can map the positions of galaxies and clusters in the Universe and ask at which separation is more likely to find formed structures. These preferred separations are peaks in the correlation function of the Large Scale Structures (LSS), and the oscillatory shape of these peaks recalls the oscillations of the primordial plasma in past epochs (CMB). The change of this peaks at different red-shifts traces the change in separation at different times, and so is a direct way to measure the angular diameter distance evolution. Fig.1.4 reports the BAO as measured from the WiggleZ survey [18], while Fig.1.3 reports the change in angular diameter distance evolution for a standard ΛCDM Universe and a flat Universe fulfilled with sole matter.

Datasets used in my works Here I report some information about datasets of distance measurements used in the following works. The SN data come from different compilations and are usually reported in terms of distance

[5]This is not as easy as it seems. In real world SN Ia present some differences in their peak luminosities, in their light-curve evolutions and in their colors, but the important fact is that is possible to reliably calibrate them in order to obtain a shared absolute luminosity [13, 14].

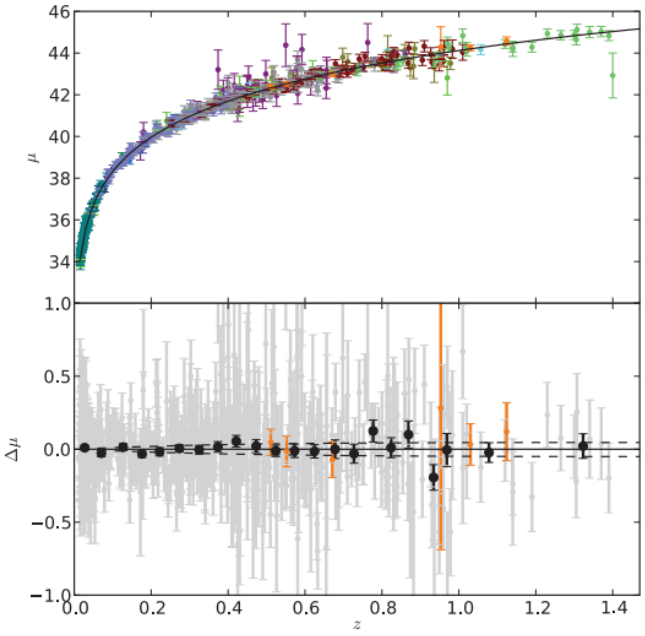

Figure 1.2: The plot shows the mapping of the luminosity distance up to $z \sim 1.4$ as measured by the Union2 compilation in terms of the distance modulus μ, refer to equation 1.27.

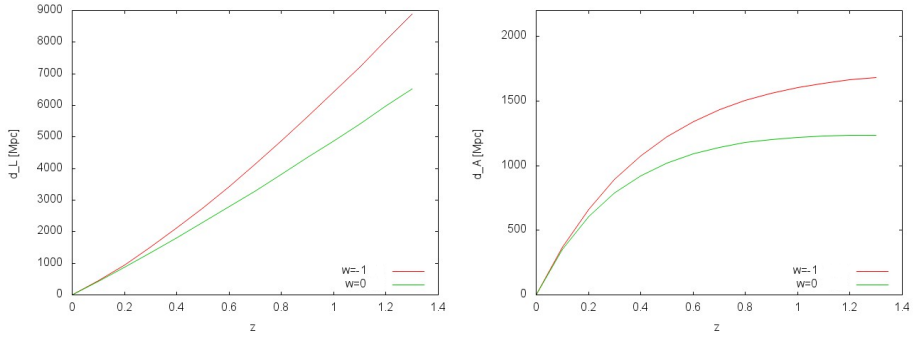

Figure 1.3: The plot shows the behaviours expected in a ΛCDM Universe (red line) and in a flat Universe with no dark energy (green line) for the luminosity distance (left panel) and the angular diameter distance (right panel).

modulus μ:

$$\mu = 2.5 log_{10}\left(\frac{L}{L_0(z)}\right) = m(z) - M - 25 \tag{1.27}$$

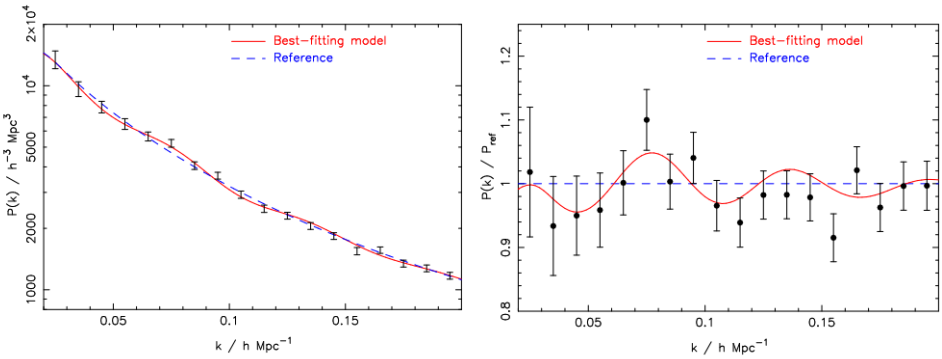

Figure 1.4: Left panel shows the matter power spectrum as measured by the WiggleZ survey in units of inverse scale length k [18]; right panel shows the wiggles obtained by subtracting a constant reference spectrum to the one measured.

where $m(z)$ and M are relative and absolute magnitude of the object.

- Super Novae Legacy Survey
  The SNLS [19] contains 427 SN data from different surveys. It goes from $z \sim 0.01$ to $z \sim 1.4$. Light-curves are fitted using both SALT2 and SiFTO [20, 21];

- Union1
  Made up of 307 SN from 13 different surveys [22], covering a red-shift range of $0.003 < z < 1.4$. Light-curve fitter is SALT [23];

- Union2
  Contains 557 SN from different surveys [15]. It covers a red-shift range from $z \sim 0.01$ to $z \sim 1.4$, and uses as light-curve fitter SALT2;

- Union2.1
  A compilation that add to Union2 25 SN [24]. They reach $z = 1.415$, and were analysed with SALT2.

For what concerns BAO measurements, data are usually reported in terms of different quantities. Beside the angular diameter distance $d_A(z)$ one can use the ratio $d_s(z) = r_s(z_d)/d_V(z)$ where $r_s(z_d)$ is the radius of the sound horizon at decoupling and:

$$d_V(z) = \left[(1+z)^2 D_A(z)^2 \frac{cz}{H(z)}\right]^{1/3}. \tag{1.28}$$

Some others use the acoustic parameter $A_s(z)$ defined as:

$$A_s(z) = \frac{D_V(z)}{cz}\sqrt{\Omega_m H(z)^2}\ . \tag{1.29}$$

- 6dFGRS
  This is a measurement at $z = 0.01$ [25], in form $d_s(z)$;
- SDSS-DR7
  Two measurements at $z = 0.20$ and at $z = 0.35$ [26], in form $d_s(z)$;
- SDSS-DR9
  One measurement at $z = 0.57$ [27], in form $d_A(z)$;
- WiggleZ
  Three measurements at $z = 0.40, 0.66, 0.73$ [18], in form $A_s(z)$.
- WiggleZ2
  Three measurements at $z = 0.40, 0.66, 0.73$ [28], in form $d_s(z)$.

1.3.2 Cosmic Microwave Background

As previously stated, during recombination, the photons finally became free to stream away from the primordial plasma and reach us. Nevertheless the temperature during recombination was something between 4000 and 3000 K, the red-shift is so high that we see it now at 2.72 K. The spectrum of this radiation is in practice the most precise black-body spectrum ever seen.

The mean temperature of this radiation is important to determine the red-shift at which recombination took place ($z \sim 1100$), but the crucial fact for cosmological research are the small anisotropies that it presents. This radiation, visible all over the sky, is indeed highly homogeneous: differences in temperature are always below 10^{-5} K. Moving to resolutions below this limit it is possible to see the small fluctuations in temperature, as the Planck map in Fig.1.5 shows. These temperature fluctuations map the small over and under densities present in the primordial Universe, from which all the LSS that we see today had birth. Performing a statistical study of these anisotropies allows us to understand the dynamics of the primordial plasma, and then to make precise predictions about the content of the primordial Universe.

The CMB power spectrum An efficient way to compute the CMB correlation function is to move in Fourier Space and work in terms of power spectra. As the Wiener–Khinchin theorem demonstrates power spectra are

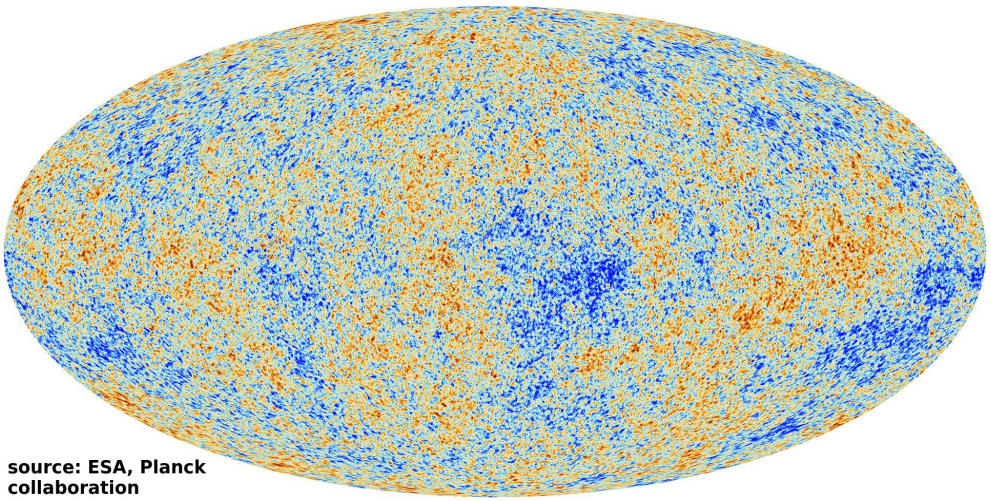

Figure 1.5: The image reports a map of the CMB as measured by Planck experiment [5].
.

the Fourier transform of correlation functions. Following [29] we define a dimensionless quantity that encodes fluctuations of the temperature field:

$$\Theta(\hat{\mathbf{n}}) = \frac{T(\hat{\mathbf{n}}) - < T >}{< T >} .$$

Dealing with a 2D representation of a sphere it is useful to work in terms of spherical harmonics $Y_{\ell m}$, where ℓ is the multipole, and represents a given angular scale in the sky, $\alpha \sim \pi/\ell$. We can expand our field in this way:

$$\Theta(\hat{\mathbf{n}}) = \sum_{\ell=0}^{\ell=\infty} \sum_{m=-\ell}^{m=\ell} a_{\ell m} Y_{\ell m}(\hat{\mathbf{n}}) \tag{1.30}$$

We can define now the power spectrum of the temperature field fluctuations as the variance of these harmonic coefficients, mediate over different realizations:

$$< a_{\ell m} a^*_{\ell' m'} >= \delta_{\ell \ell'} \delta_{m m'} C_\ell \ . \tag{1.31}$$

We cannot reproduce the Universe, so there is an inner limitation of the m-modes for each multipole that we can measure that is $(2\ell+1)$. Knowing this we can express the power spectrum as:

$$C_\ell = \frac{1}{2\ell+1} \sum_{m=-\ell}^{\ell} < |a_{\ell m}|^2 > \tag{1.32}$$

and this leads to an unavoidable uncertainty ΔC_ℓ known as *cosmic variance*. The cosmic variance comes from the actual difference between the expectation value of the observed spectrum $\hat{C}_\ell$ and its theoretical value C_ℓ:

$$< (\hat{C}_\ell - C_\ell)^2 >= \frac{2}{2\ell + 1} C_\ell^2. \tag{1.33}$$

An image of the CMB power spectrum as measured by Planck is reported in Fig.1.6.

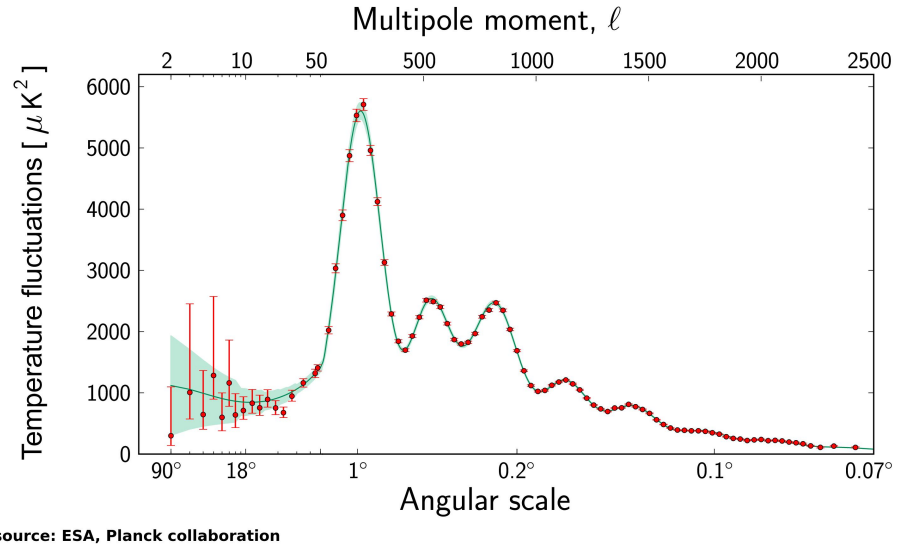

Figure 1.6: CMB power spectrum as measured by Planck experiment [5].

.

Meaning of anisotropies Following Tegmark [30] one can identify three levels of anisotropies in the CMB: primary, coming from plasma physics; secondary, coming from the interaction between CMB photons and structures in the Universe; tertiary, better known as foregrounds.

- Primary
  These are due to plasma physics. Oscillations of plasma are caused by gravity, Doppler effect and density field. In formulas, the three effects give:

$$\Theta(\hat{\mathbf{n}}) = \phi(\mathbf{n}) - \hat{\mathbf{n}} \cdot \mathbf{v}(\mathbf{n}) + \frac{1}{3}\delta(\mathbf{n}) \tag{1.34}$$

where the first term on the right is the red-shift due to the potential well ϕ, the second is the Doppler red-shift due to the peculiar velocity of the matter scattering the photon and the last is the intrinsic higher temperature of the over-dense regions. In this category fall also effects that damp the acoustic oscillations in the high-ℓ part of the spectrum, like the free streaming of relativistic particles, that tends to smear out oscillations at small scales.

- Secondary
  Secondary anisotropies are due to the interactions the photon undergoes while streaming towards us. The most important are reported in left panel of Fig.1.7 The *Integrated Sachs-Wolf effect* (ISW) describes

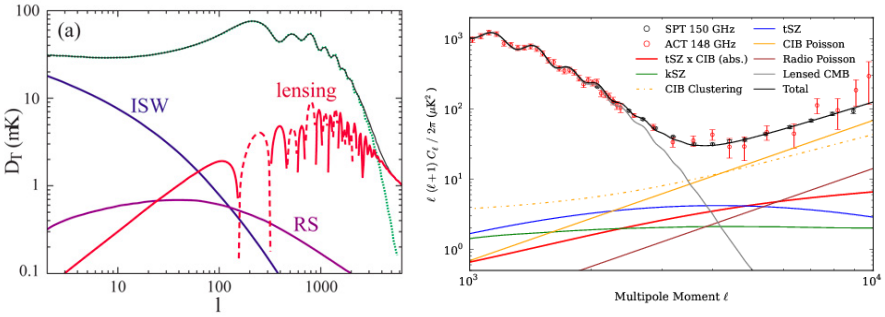

Figure 1.7: The left panel of the plot shows most important secondary anisotropies (ISW, RS, lensing) of the CMB [31], the right panel depicts typical foregrounds, besides CMB damping tail data from ACT and SPT experiments [32].

the fact that modifications of the gravitational potential imprint temperature anisotropies, following that, for a photon:

$$\Theta(\hat{\mathbf{n}}) = \int \dot{\phi}[\mathbf{n}(t), t]dt \ . \tag{1.35}$$

The ISW contains the Early ISW (due to transition from radiation to matter era), the Late ISW (due to transition to dark energy era) and the *Rees-Sciama effect* (RS, due to local non-linearities of structures). The ISW effect enhances the power at very high scales.

The *weak lensing* of the CMB makes photons change path due to LSS encountered during their travelling. This causes a damping of the high-ℓ tail of the spectrum: the total power is conserved but is redistributed from peaks to troughs.

The *Sunyaev-Zel'dovich effect* depends on local big structures like clusters. Photons of the CMB passing through clusters are Thomson scattered by the gas and this causes a distortion in the shape of the CMB power spectrum. The effect is called kinematic if it comes from a Doppler shift due to the peculiar velocity of the cluster, and thermal if due to the scattering with the energetic electrons forming the hot gas.

The *global re-ionization* of the Universe at red-shift $z \sim 10$ causes a loss of power at small scales due to the probability of the photons to be scattered by electrons, loss that is proportional to the optical depth of the Universe.

- Tertiary
  Tertiary anisotropies are identified as foregrounds. At large scales we have point sources that emit in radio or IR, at galactic scales there are dust, free-free and synchrotron emissions, and finally we have local effects like noise or atmosphere interactions that can be removed using space missions. Point sources are usually mapped and eliminated from the analysis (the masking of the sky), like also the strong galactic emissions of our and nearby galaxies. Relic contamination is usually fitted out using empirical power laws. The process of masking implies that we do not use the entire sky to analyse the CMB. This reduces the accuracy of the predictions. The fraction of the sky used in the analysis is typically indicated as f_{sky}, and is included in the likelihoods used to determine cosmological parameters. An explicative image is reported in right panel of Fig.1.7

Other CMB spectra Beside the temperature spectrum we can determine other spectra from the CMB. Other two-point correlation functions that we can compute are the polarization spectra. We can also compute higher-order statistics moving to three-point correlation function (bi-spectrum, useful for checks on the Gaussianity of the CMB) or four-point correlation function (tri-spectrum, linked to the lensing of the CMB).

Polarization of the CMB comes from scattering phenomena only [33]. Photons scattered by electrons acquire a polarization. To produce polarization a quadrupole anisotropy is needed, and this can be generated by scalar perturbation of density, vector perturbations due to vorticity or tensor perturbations due to gravitational waves. The polarization spectra of the CMB are particularly indicated to study the re-ionization history (scalar perturbations) and inflationary scenarios (tensor perturbations). The polarization is usually decomposed in two components:

EE component
gradient-like mode, due to scalar and tensor perturbations;

BB component
curl-like mode, due to vector and tensor perturbations.

In this way one can compute other three spectra: C_ℓ^{EE}, C_ℓ^{TE} and C_ℓ^{BB}, because, due to parity reasons, C_ℓ^{TB} and C_ℓ^{BB} vanish. In particular the E spectrum can give important information on re-ionization and the B spectrum contains the contribution of possible inflationary gravitational waves and weak lensing effects. All the polarization spectra are contaminated by foregrounds that polarize radiation at small scales. In Fig.1.8 are reported polarization data.

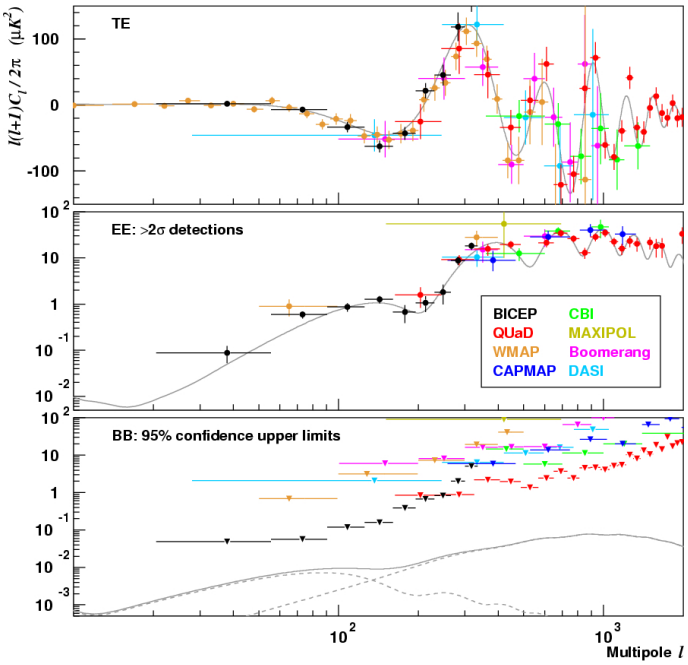

Figure 1.8: This plot shows polarization data from several experiments [34].

The CMB observed spectrum is lensed, in the sense that the photons we see have been deflected by the LSS during their travelling. This deflection is indicated as:

$$T_o(\hat{\mathbf{n}}) = T(\hat{\mathbf{n}}') = T(\hat{\mathbf{n}} + \alpha) \tag{1.36}$$

$$\alpha = \nabla\phi \tag{1.37}$$

where T_o is the observed lensed temperature, T is the unlensed and ϕ is the CMB lensing potential. The effect is small, so we can work at first order:

$$T_o(\hat{\mathbf{n}}) = T(\hat{\mathbf{n}}) + \sum_i \nabla^i \phi(\hat{\mathbf{n}}) \nabla_i T_o(\hat{\mathbf{n}}) \ . \tag{1.38}$$

The effect of lensing is to correlate the lensed temperature to the gradient of the unlensed temperature. When averaging over realizations of lensing potential and CMB unlensed spectra, the lensing introduces a non-Gaussianity in the CMB that is visible in the connected part of the CMB tri-spectrum. From this feature one can measure the lensing spectrum $C_\ell^{\phi\phi}$ [35]. The Planck measured lensing of the CMB is reported in Fig.1.9.

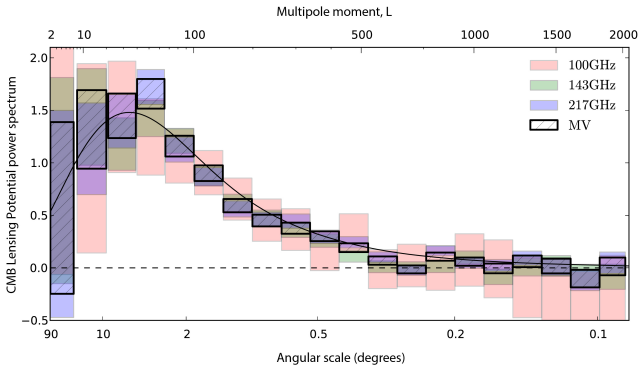

Figure 1.9: The lensing spectrum of the CMB as measured by Planck experiment.

.

Datasets used in this thesis The base dataset of the last years for CMB research was WMAP. This experiment measured at very high precision the first 1200 multipoles of the CMB power spectrum. To include also measurements of the damping tail, other datasets like ACT or SPT measurements could be combined with it. In March 2013 Planck space mission released its first dataset, replacing WMAP as the standard for CMB temperature power spectrum.

- WMAP
  Space mission that observed the sky in 5 bands. I used the 7 years [36] and the 9 years releases [4]. WMAP measured CMB power spectra at high precision in temperature up to $\ell = 1200$, and in polarization (E/B) up to $\ell = 1024$.

- SPT
  Ground based experiment, a 10 mt telescope located at South Pole. Observed sky in 5 frequency bands, obtaining anisotropies measurements up to $\ell < 10000$ [38].

- ACT
  Ground based experiment, a 6 mt telescope located in northern Chile. Observed sky in 3 frequency bands, obtaining anisotropies measurements up to $\ell < 10000$ [37].

- Planck
  Space mission based on 9 channels observations. Planck measured the CMB temperature power spectrum at exquisitely high precision up to multipole $\ell = 2500$. It is used in combination with WMAP polarization spectra, because the Planck polarization measurements are up to come with next release. Beside the TT power spectrum Planck released also the lensing power spectrum, up to $\ell = 2000$.

1.3.3 Clustering measurements

This kind of measurements intends to constraint the clustering power of the LSS. These are considerably young observables, and can be of different type. In our interacting dark energy work we used one type of them: the Red-shift Space Distortions (RSD). Because we are living in an isotropic Universe, if we make a map of the structures of the Universe we should recover angular invariance. This is not the case. Indeed, the peculiar velocities of the objects themselves distort this kind of mapping, because to recreate a 3D map the distance of objects is inferred from the red-shift (remember Hubble law 1.11 and the red-shift-distance relation). Red-shift however does not contain only the Hubble flow contribution, but also the intrinsic velocity of the source.

The idea behind RSD is to use this anisotropy between line-of-sight and perpendicular velocities of objects to determine their motion. This motion is due to the gravitational clustering of matter, so the RSD measurements can give a statistical prediction of the clustering of structures at different epochs. In Fig.1.10 I report an example of this anisotropy between line of sight and perpendicular directions. The clustering power is usually defined with $f\sigma_8$:

$$f\sigma_8 = \frac{\partial \sigma_8}{\partial \ln a}\sigma_8 \tag{1.39}$$

where σ_8 is a quantity that represents the amplitude of the matter power spectrum in terms of density variance inside spheres of 8 Mpc. RSD data,

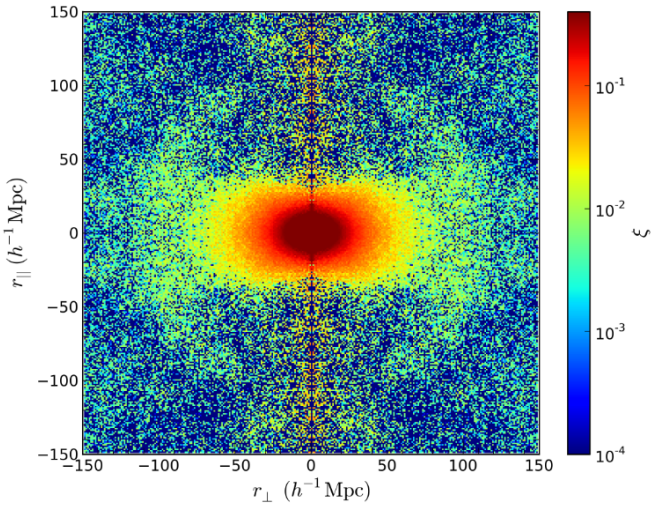

Figure 1.10: This plot shows the typical anisotropy of LSS mapping, represented as a smashing of the two-point correlation function [39]

.

anyway, are usually reduced to this quantity assuming a ΛCDM background evolution. In situations in which the background evolution of the Universe is not ΛCDM is necessary to check the values of other quantities like D_V (1.28) and the Alcock-Paczynski[6] variable F:

$$F = \frac{1+z}{c} D_A(z) H(z) \ . \tag{1.40}$$

The dataset used for my analysis is a compilation of different $f\sigma 8$ measurements as shown in Tab.1.1. The full analysis with the whole set $f\sigma 8 - F - D_V$ was performed using data from Tab.1.2

1.3.4 Hubble parameter measurements

In some analysis I also make use of some Hubble constant H_0 and Hubble parameter $H(z)$ measurements.

The Hubble constant measurement used is the one of [44], obtained using a Hubble space telescope (HST) camera to observe SN and Cepheids[7] and determine distances from which to infer the value of H_0. The Hubble flow

[6]The Alcock-Paczynski effect is a distortion in the LSS mapping due to different background evolutions that lead to different translations of red-shifts in distances.

[7]Cepheids are also standard candles. They are variable stars, and the period of their pulsation is proportional to their absolute magnitude [10].

Survey	z	$f\sigma_8$	ref
6dFGRS	0.067	0.42 ± 0.06	[25]
2dFGRS	0.17	0.51 ± 0.06	[40]
WiggleZ	0.22	0.42 ± 0.07	[41]
SDSS LRG	0.25	0.39 ± 0.05	[39]
SDSS LRG	0.37	0.43 ± 0.04	[39]
WiggleZ	0.41	0.45 ± 0.04	[41]
BOSS CMASS	0.57	0.43 ± 0.03	[42]
WiggleZ	0.60	0.43 ± 0.04	[41]
WiggleZ	0.78	0.38 ± 0.04	[41]
VIPERS	0.80	0.47 ± 0.08	[43]

Table 1.1: RSD measurements used in $f\sigma_8$-only and corresponding references.

Survey	z	$f\sigma_8$	ref
WiggleZ	0.44	0.45 ± 0.04	[28]
BOSS CMASS	0.57	0.43 ± 0.03	[42]
WiggleZ	0.60	0.43 ± 0.04	[28]
WiggleZ	0.73	0.38 ± 0.04	[28]

Table 1.2: RSD measurements used in this analysis and corresponding references.

dataset used, instead, is a compilation of 18 measurements at different red-shifts made by Moresco at al. [45] using the technique of the cosmic clocks. Using the difference in age (spectroscopically determined) Δt of two passive evolving galaxies, formed at the same time but slightly separated in red-shift Δz, it is possible to compute the derivative dz/dt and so the Hubble flow at that epoch [46].

Chapter 2

The dark sector

'...Matter of fact it's all dark.'

Pink Floyd - Eclipse

In this chapter we will review the properties of the various components of the Universe, with a particular focus on the dark sector. As stated before, the behaviour of a species is determined by its EOS 1.13, namely the ratio between its pressure and its density.

Recall of statistical mechanics To understand why each species has its specific EOS we should make some use of statistical mechanics. A particle with a mass m and momentum p has an energy:

$$E = \sqrt{p^2 + m^2} \ .$$

If it is in equilibrium at a temperature T then the following function represents the occupation of the phase space:

$$f(p) = \frac{1}{exp[\frac{E-\mu}{T}] \pm 1} \tag{2.1}$$

that does not depend on the location, given the homogeneity of the Universe. The plus sign is for fermions while the minus applies for bosons. Finally μ is the chemical potential. From here we can compute density and pressure of a species:

$$\rho = g \int \frac{d^3p}{(2\pi\hbar)^3} E(p) f(p) = \frac{g}{2\pi^2} \int_m^\infty dE \frac{(E^2 - m^2)^{\frac{1}{2}}}{exp[\frac{E-\mu}{T}] \pm 1} E^2 \tag{2.2}$$

$$P = g \int \frac{d^3p}{(2\pi\hbar)^3} \frac{pv}{3} f(p) = g \int \frac{d^3p}{(2\pi\hbar)^3} \frac{p^2}{3E} f(p) = \frac{g}{6\pi^2} \int_m^\infty dE \frac{(E^2 - m^2)^{\frac{3}{2}}}{exp[\frac{E-\mu}{T}] \pm 1} \tag{2.3}$$

where g counts the internal degrees of freedom and v is the particles' velocity.

Perturbation equations in synchronous gauge The idea behind everything is that small quantum fluctuations in primordial Universe were inflated to wavelengths beyond the size of horizon during the inflationary era. These fluctuations eventually enters the horizon as time goes by and horizon grows. These anisotropies grew thanks to self gravity, arriving to form the LSS that we see today. However, for what concerns primordial era, their amplitude is small, and one can use perturbation theory to evolve them. A general relativistic treatment is required for perturbations on scale larger than the horizon size. This leads to the choice of a gauge. The two typical gauges used for this calculations are the synchronous and the conformal Newtonian one. The Newtonian gauge evolves scalar perturbations only, and that is the reason why the numerical code generally used for this integration, `camb` [47], works in the synchronous gauge. I will present here the two gauges and the general results for the linear theory of scalar iso-entropic gravitational perturbations in the synchronous gauge. This linear theory is obtained by coupling and linearising the Einstein, Boltzmann and fluid equations for the metric and the density perturbations [48]. Then, in each section, I will report the specific equations for the different components.

Consider a flat background space-time. In synchronous gauge the line perturbed element is:

$$ds^2 = a^2(\tau)[-d\tau^2 + (\delta_{ij} + h_{ij})dx^i dx^j] \tag{2.4}$$

where τ is the conformal time[1] and, by gauge definition, the g_{00} and g_{0i} components of the metric tensor are unperturbed. The perturbation h_{ij} can be decomposed in a trace part $h = h_{ii}$ and a traceless part consisting of three pieces, $h^{\parallel}_{ij}$, $h^{\perp}_{ij}$ and h^{T}_{ij}, the first having a longitudinal and the latter two a transverse divergence. The scalar modes of the perturbations arise from h and $h^{\parallel}_{ij}$, the vector modes from $h^{\perp}_{ij}$ and the tensor modes from h^{T}_{ij}. We will work with scalar perturbations only here. We can express the scalar mode of h_{ij} as the Fourier integral:

$$h_{ij}(\vec{x},\tau) = \int d^3k e^{i\vec{k}\cdot\vec{x}}\Big[\hat{k}_i\hat{k}_j h(\vec{k},\tau) + (\hat{k}_i\hat{k}_j - \frac{1}{3}\delta_{ij})6\eta(\vec{k},\tau)\Big] \tag{2.5}$$

where $\hat{k}$ is the versor of $\vec{k}$, h still represents the trace of h_{ij} and $\eta(\vec{k},\tau)$ is another field.

In conformal gauge, perturbations are represented by two scalar potentials ϕ and ψ, with ϕ being the gravitational potential in the Newtonian limit. The line element reads:

$$ds^2 = a^2(\tau)[-(1+2\phi)d\tau^2 + (1-2\psi)dx^i dx^j] \ . \tag{2.6}$$

[1]Conformal time is related to the proper time as $dx^0 = d\tau = dt/a(\tau)$.

Getting back to the synchronous gauge, the linearised Einstein equation is composed by:

$$k^2\eta - \frac{1}{2}\frac{\dot{a}}{a}\dot{h} = 4\pi G a^2 \delta T^0_0 \tag{2.7}$$

$$k^2\dot{\eta} = 4\pi G a^2(\overline{\rho} + \overline{P})\theta \tag{2.8}$$

$$\ddot{h} + 2\frac{\dot{a}}{a}\dot{h} - 2k^2\eta = -8\pi G a^2 \delta T^i_i \tag{2.9}$$

$$\ddot{h} + 6\ddot{\eta} + 2\frac{\dot{a}}{a}(\dot{h} + 6\dot{\eta}) - 2k^2\eta = -24\pi G a^2(\overline{\rho} + \overline{P})\sigma \tag{2.10}$$

where $(\overline{\rho}+\overline{P})\theta = ik^j\delta T^0_j$ is related to the divergence of the fluid velocity and $(\overline{\rho} + \overline{P})\sigma = -(\hat{k}_i\hat{k}_j - \frac{1}{3}\delta_{ij})(T^i_j - \delta^i_j T^k_k/3)$ is related to its anisotropic stress.

Remembering the form of the energy-momentum tensor in 1.6 we can derive its perturbation to linear order:

$$T^0_0 = -(\overline{\rho} + \delta\rho) \tag{2.11}$$

$$T^0_i = (\overline{\rho} + \overline{P})v_i = -T^i_0 \tag{2.12}$$

$$T^i_j = (\overline{P} + \delta P)\delta^i_j + (T^i_j - \delta^i_j T^k_k/3) \tag{2.13}$$

where $v^i = dx^i/d\tau$ is the velocity of the fluid, that can be treated as a perturbation of the same order as $\delta\rho$, δP and the metric perturbations.

The non-relativistic fluid approximation can be used for CDM and baryons. The conservation of energy-momentum gives:

$$T^{\mu\nu}_{;\mu} = \partial_\mu T_{\mu\nu} + \Gamma^\nu_{\alpha\beta}T^{\alpha\beta} + \Gamma^\alpha_{\alpha\beta}T^{\nu\beta} = 0 \tag{2.14}$$

which in k-space becomes:

$$\dot{\delta} = -(1+w)\Big(\theta + \frac{\dot{h}}{2}\Big) - 3\frac{\dot{a}}{a}\Big(\frac{\delta P}{\delta\rho} - w\Big)\delta \tag{2.15}$$

$$\dot{\theta} = -\frac{\dot{a}}{a}(1-3w)\theta - \frac{\dot{w}}{1+w}\theta + \frac{\delta P/\delta\rho}{1+w}k^2\delta - k^2\sigma \tag{2.16}$$

with $\delta = \delta\rho/\overline{\rho}$. These equations need to be modified if components interact with each other, as for baryons which couple with photons via Thomson scattering.

Radiation components, on the other side, must be described using the full distribution functions in phase-space. The phase-space distribution function gives the number of particles in the phase volume $d^3x d^3P$, where x is the spatial coordinate and P is the conjugate momentum, simply the spatial

part of the four-momentum with lower indices $P_i = mu_i$, with m the mass of the particle:

$$f(x^i, P_j, \tau) d^3x d^3P = dN \ . \tag{2.17}$$

The zero-order distribution function is the Fermi-Dirac or Bose-Einstein 2.1 for fermions and bosons respectively. The energy-momentum tensor then reads:

$$T_{\mu\nu} = \int d^3P (-g)^{-1/2} \frac{P_\mu P_\nu}{P^0} f(x^i, P_j, \tau) \ . \tag{2.18}$$

Now it is useful to express $P_j = aq_j$ and $q_j = qn_j$, and use this new coordinates to write the distribution function as the zero-order one plus a perturbed piece:

$$f(x^i, P_j, \tau) = f_0(q)[1 + \Psi(x^i, q, n_j, \tau)] \tag{2.19}$$

so that, at linear order, one has:

$$T^0_0 = -a^{-4} \int q^2 dq d\Omega \sqrt{q^2 + m^2a^2} f_0(q)(1 + \Psi) \tag{2.20}$$

$$T^0_i = a^{-4} \int q^2 dq d\Omega q n_i f_0(q) \Psi \tag{2.21}$$

$$T^i_j = a^{-4} \int q^2 dq d\Omega \frac{q^2 n_i n_j}{\sqrt{q^2 + m^2a^2}} f_0(q)(1 + \Psi) \tag{2.22}$$

where $d\Omega$ is the solid angle associated with direction n_i and $\sqrt{q^2 + m^2a^2} = \epsilon(q, \tau)$ is the co-moving energy. The phase-space distribution evolves following the Boltzmann equation:

$$\frac{Df}{d\tau} = \frac{\partial f}{\partial \tau} + \frac{dx^i}{d\tau}\frac{\partial f}{\partial x^i} + \frac{dq}{d\tau}\frac{\partial f}{\partial q} + \frac{dn^i}{d\tau}\frac{\partial f}{\partial n^i} = \Big(\frac{\partial f}{\partial \tau}\Big)_C \tag{2.23}$$

where last term is due to collisions. At first order in k-space the Boltzmann equation is:

$$\frac{\partial \Psi}{\partial \tau} + i\frac{q}{\epsilon}(\vec{k} \cdot \hat{n})\Psi + \frac{d \ln f_0}{d \ln q}\Big[\dot{\eta} - \frac{\dot{h} + 6\dot{\eta}}{2}(\hat{k} \cdot \hat{n})^2\Big] = \frac{1}{f_0}\Big(\frac{\partial f}{\partial \tau}\Big)_C \ . \tag{2.24}$$

The following equations will be used to compute the evolution of the perturbations of the dark sector of the Universe in the following sections. We will always consider purely adiabatic initial conditions. For the photons and baryons perturbations refers to Appendix A.

2.1 Dark radiation

Radiation is the Universe's component that dominated the first age of its history. With the term radiation one indicates the relativistic species, like

photons or neutrinos. Recalling 2.2 and 2.3 we can compute the EOS of radiation, knowing that $m \to 0$ and assuming $T \gg \mu$:

$$\rho = \begin{cases} bosons \ \to & \frac{\pi^2}{30} g T^4 \\ fermions \ \to & \frac{7}{8}\frac{\pi^2}{30} g T^4 \end{cases}$$

$$P = \frac{\rho}{3}$$

Obtaining $w_r = 1/3$. Using now the density evolution equation 1.13, we have:

$$\rho \propto a^{-4} \ .$$

When radiation dominates, the scale factor of the Universe grows as (recall 1.14):

$$a \propto t^{\frac{1}{2}} \ .$$

The number of photons is determinable from the CMB, while for neutrinos one can determine it imposing the conservation of entropy at the time at which e^+e^- annihilates ($E \sim 1$Mev) [49]. The total value for radiation today (assuming a standard number of neutrinos) is:

$$\Omega_{r,0} = \frac{\rho_{\gamma,0} + \rho_{\nu,0}}{\rho_{c,0}} = 8.051 \cdot 10^{-5} \ .$$

Neutrinos are a big puzzle in modern cosmology and particle physics, that are working side by side to determine their properties. Light neutrinos (the relativistic ones) come in 3 flavours, following the standard model[2]. These three flavours are associated with electron, muon and tau particle interactions. Neutrinos, however, are only weakly interacting particles, and this is the reason why they are so elusive. They are known to perform *oscillations*, in the sense that they are created from interactions as flavour eigenstates, but these eigenstates do not coincide with their mass eigenstates. While travelling, then, a neutrino changes its flavour accordingly to a determined probability, given by a mixing angle. This theory has been proved indirectly by solar and atmospheric neutrino observations (solar neutrinos are produced in nuclear reactions of our star, while atmospheric neutrinos are produced in nuclear showers due to cosmic rays interacting with atmospheric particles [50]). The two mixing angles measured leave an uncertainty on how these three different masses are sorted with respect to flavours. There are two possibility: a normal hierarchy and an inverse one. Cosmology comes in to play here, because observations are capable of determining the sum of

[2]The value of 3 is indeed confirmed by BBN predictions and by high-energy experiments.

the masses of the neutrinos: this sum can finally determine the right hierarchy [51].

Another big question is whether neutrinos are Dirac or Majorana particles. The first are particles that differ from their antiparticles while the latter are particles that coincide with their antiparticle. The way to prove the Majorana nature of neutrinos should be the observation of the neutrino-less double beta decay, still not observed, given also that its time-scale is huge [52]. If neutrinos were a Majorana particle, moreover, a see-saw mechanism could have created a massive sterile neutrino whose existence is determinable by cosmological observations.

Perturbation theory For massless neutrinos we have $\rho_\nu = 3P_\nu = -T^0_0 = T^i_i$. To reduce the number of variables one usually integrates out the q dependence and expands the angular dependence in a series of Legendre polynomials:

$$F_\nu(\vec{k}, \hat{n}, \tau) = \frac{\int q^2 dq q f_0 \Psi}{\int q^2 dq q f_0} = \sum_{l=0}^{\infty} (-i)^l (2l+1) F_{\nu l}(\vec{k}, \tau) P_l(\hat{k} \cdot \hat{n}) \tag{2.25}$$

where the $F_{\nu l}$ are spherical Bessel functions. Evolving the Boltzmann equation 2.24 in this way and using the results in 2.20 one ends up with the following perturbation equations:

$$\dot{\delta}_\nu = -\frac{4}{3}\theta_\nu - \frac{2}{3}\dot{h} \tag{2.26}$$

$$\dot{\theta}_\nu = k^2\Big(\frac{1}{4}\delta_\nu - \sigma_\nu\Big) \tag{2.27}$$

$$\dot{F}_{\nu 2} = 2\dot{\sigma}_\nu = \frac{8}{15}\theta_\nu - \frac{3}{5}kF_{\nu 3} + \frac{4}{15}\dot{h} + \frac{8}{5}\dot{\eta} \tag{2.28}$$

$$\dot{F}_{\nu l} = \frac{k}{2l+1}\Big[lF_{\nu(l-1)} - (l-1)F_{\nu(l+1)}\Big] \tag{2.29}$$

Last equation must be truncated at some l_{max}.

For massive neutrinos the procedure is to expand directly the perturbation Ψ in Legendre series:

$$\Psi(\vec{k}, \hat{n}, q, \tau) = \sum_{l=0}^{\infty} (-i)^l (2l+1) \Psi_l(\vec{k}, q, \tau) P_l(\hat{k} \cdot \hat{n}) \tag{2.30}$$

and then numerically compute the integrals of Ψ on dq in 2.20 to obtain the density, pressure, velocity and shear perturbations.

2.2 Dark matter

Non-relativist matter is the second component to dominate the Universe evolution, soon after the radiation era. With the term matter density we indicate both baryons and CDM. From the EOS point of view, it holds that $m \gg T$, giving:

$$\rho = gm\left(\frac{mT}{2\pi}\right)^{\frac{3}{2}} exp\left[-\frac{(m-\mu)}{T}\right]$$

$$P = gT\left(\frac{mT}{2\pi}\right)^{\frac{3}{2}} exp\left[-\frac{(m-\mu)}{T}\right] = \frac{T}{m}\rho \sim 0$$

showing that the EOS is $w_m \sim 0$. With this value the evolution of the matter density is:

$$\rho \propto a^{-3}$$

and during its domination the scale factor evolves as (recall 1.14):

$$a \propto t^{\frac{1}{2}} \ .$$

Baryons are the ordinary matter we see and we are made of. However, different estimations of its density, from BBN predictions to observation of Universal LSS, agree on a density parameter value that is much smaller than the one needed for non-relativistic matter to build the Universe we are living in. Indeed while the present matter amount in the Universe accounts for about the 30% of the total density, the baryons alone cannot be more than the 5% of the total. This discrepancy leads to the introduction of non interacting (and so non observable) matter particles in the overall picture. Dark matter is also supported by a number of other observations: rotational velocities of galaxies, hot gas inside big clusters and lensing effects [53, 54]. Properties for dark matter can be different, and it is usual to divide it in 3 classes: cold dark matter (CDM), warm dark matter (WDM) and hot dark matter (HDM). The term cold dark matter indicates particles that became non relativistic when also baryons did. A part of the CDM can be identified with single massive and obscure objects made up of baryons (star remnants and so on, called MACHOS) but this kind of objects cannot account for the whole quantity of dark matter needed and cannot provide important features that CDM does for structure formation and equilibrium. Besides MACHOS other particles are proposed to play the role of dark matter, like axions or other types of weakly interacting massive particles (WIMPs), but until now none of these has been proved to be the right answer. Hot dark matter, like neutrinos, is instead made of particles with a mass much smaller than CDM

and that thus exited the relativistic regime much later. Finally, warm dark matter is an in-between solution, well represented by sterile neutrinos. The reason why the standard model of the Universe is based on CDM must be found in the evolution of perturbations.

Looking at the formed structures of the Universe today, one can determine which have reached dynamical equilibrium (virialized) and which not. The case is that small structures are in equilibrium (galaxies, star clusters and so on) while the big clusters of galaxies are not. This is a consequence of the fact that small structures in the Universe formed first, followed by bigger and bigger ones as the time went by. This kind of hierarchical evolution is possible only if dark matter in the Universe is cold. Baryons, indeed, because of their coupling to the photons due to Thomson scattering, start to gravitationally collapse well after their transition to the non relativistic regime. If the Universe is fulfilled with CDM, that is not coupled with photons, it can start to form structures soon after the non relativistic transition. In this way, when the baryons finally decouple from photons, they just fall into the gravitational wells formed by CDM and give rise to the hierarchical clustering that we see in the sky. Different numerical simulations of the non-linear clustering of structures in presence of CDM, WDM and HDM confirm the need for a cold form of dark matter [55].

CDM has never been detected directly right now, although many experiments on earth and in atmosphere are devoted to this search [56].

Perturbation theory Perturbation equations for dark matter are simple because we can treat it as non-relativistic and collision-less. Moreover CDM can be used to define the synchronous coordinates and so has zero peculiar velocity in this gauge. Setting $\theta = \sigma = 0$ and $w = \dot{w} = 0$ in equations 2.15 one ends up with the sole equation:

$$\dot{\delta}_c = -\frac{1}{2}\dot{h} \tag{2.31}$$

for the density perturbations, that are directly related to the traceless part of the metric perturbations.

2.3 Dark energy

Discovering the nature of dark energy is probably the biggest challenge of modern Cosmology. Today dark energy is the dominant component of the Universe, representing the 70% of the total density, and its properties are

driving the space-time accelerated expansion that we observe [57]. Dark energy must have an EOS $w < -1/3$ in order to the allow for acceleration in the expansion of the Universe. This implies a negative pressure for this component. In the standard model it is identified with a cosmological constant Λ, whose EOS is $w = -1$, keeping its density constant in time. It is intended as the energy generated by vacuum fluctuations, a natural way to infer an energy density that stays constant nevertheless the expansion of the space-time itself. The problem with this model is that the vacuum energy measured today is about 122 orders of magnitude lower than the vacuum energy expected by theoretical calculations. Besides, there is a conceptual issue known as coincidence problem. We happen to live in an epoch in which matter and vacuum densities are of the same order, and this is why we can actually see the accelerated expansion of the Universe. If we lived a little bit earlier or later, we would never have seen the effects that make us call for the presence of dark energy. Given the age of the Universe, the fact that we live in this small window of time in which we can sense the presence of dark energy seems at best a bit suspicious. The cosmological constant model does not involve a physical mechanism that can make sense of this coincidence.

Beside Λ, other models have been developed [58]; some of these identify dark energy with an exotic scalar field slow rolling on its potential (similarly to inflation) [59], while other explain the accelerated expansion of the Universe as the result of a modification of the law of gravity at very high scales [60]. In a particularly known class of these models, modifications arise from a different form of the Einstein-Hilbert action of gravity, that does not depend solely on the scalar curvature R, but also on functions of it (f(R) theories).

In general, whatever is our favoured model to explain dark energy, we can parametrise it as an effective energy density with an effective EOS, time-dependent or not. Recent measurements show that today the value of w must be close to -1, leaving feasible any possible theory that allows for this behaviour.

Perturbation theory In the case of a cosmological constant there are no perturbation equations, because, for construction, a cosmological constant does not evolve in time nor shows anisotropies. When dealing with quintessence model with an EOS $w > -1$ one can simply use equations 2.15 with the correct value of w. However, for phantom models, which EOS is $w < -1$, synchronous gauge introduces coordinates singularities that do not allow the evolution of these models' perturbations. These models must be studied in the Parametrised Post-Friedmann framework (PPF) developed by

Hu [61, 62].

In PPF framework, density and momentum are substituted by a unique dynamical variable:

$$\Gamma = \frac{4\pi G a^2}{k^2}\rho_x(\delta_x + 3u_x/k_H) - \phi$$

and the conservation laws are expressed as two closure relations. The first makes the anisotropic stress vanish for linear field perturbations. The second relates momentum perturbations of dark energy and dark matter and defines a transition scale under which dark energy actually becomes relatively smooth.

2.4 APPENDIX A - Perturbation equations for photons and baryons

For sake of completeness I report here the perturbation equations for photons and baryons. This two species are coupled until recombination. In Thomson scattering the energy of the photon $h\nu$ is much less than the electron rest mass $m_e \sim 0.511$Mev. The classical differential cross section is:

$$\frac{d\sigma}{d\Omega} = 3\sigma_T \frac{1 + cos^2\theta}{16\pi}$$

where θ is the scattering angle and $\sigma_T = 0.6652$ X$10^{-24} cm^2$. The number of free electrons $n_e(z)$ is derived following the re-ionization history.

The evolution of the photon perturbations can be treated as the massless neutrino case, with a major difference: the collisional terms in the Boltzmann equation are now present and they depend on polarization. Photons travelling along $\hat{n}$ are linearly polarised in the plane perpendicular to $\hat{n}$. One has to compute both the sum (intensity) and the difference (Stokes parameter Q) of the phase densities in the two polarization states. The former will be $F_\gamma(\vec{k}, \hat{n}, \tau)$ as for neutrinos, while the latter will be $G_\gamma(\vec{k}, \hat{n}, \tau)$. The linearised collision operators for Thomson scattering are:

$$\Big(\frac{\partial F_\gamma}{\partial \tau}\Big) = a n_e \sigma_T \Big[- F_\gamma + F_{\gamma 0} + 4\hat{n}\cdot\vec{v}_e - \frac{1}{2}(F_{\gamma 2} + G_{\gamma 0} + G_{\gamma 2})P_2 \Big]$$

$$\Big(\frac{\partial G_\gamma}{\partial \tau}\Big) = a n_e \sigma_T \Big[- G_\gamma + \frac{1}{2}(F_{\gamma 2} + G_{\gamma 0} + G_{\gamma 2})(1 - P_2) \Big] .$$

Starting from here one expands the F_γ and G_γ in Legendre series and obtains the perturbation equations:

$$\dot{\delta}_\gamma = -\frac{4}{3}\theta_\gamma - \frac{2}{3}\dot{h}$$

$$\dot{\theta}_\gamma = k^2\Big(\frac{1}{4}\delta_\gamma - \sigma_\gamma\Big) + an_e\sigma_T(\theta_b - \theta_\gamma)$$

$$\dot{F}_{\gamma 2} = 2\dot{\sigma}_\gamma = \frac{8}{15}\theta_\gamma - \frac{3}{5}kF_{\gamma 3} + \frac{4}{15}\dot{h} + \frac{8}{5}\dot{\eta} - \frac{9}{5}an_e\sigma_T\sigma_\gamma + \frac{1}{10}an_e\sigma_T(G_{\gamma 0} + G_{\gamma 2})$$

$$\dot{F}_{\gamma l} = \frac{k}{2l+1}[lF_{\gamma(l-1)} - (l+1)F_{\gamma(l+1)}] - an_e\sigma_T F_{\gamma l},\ l \geq 3$$

$$\dot{G}_{\gamma l} = \frac{k}{2l+1}[lG_{\gamma(l-1)} - (l+1)G_{\gamma(l+1)}] +$$

$$+an_e\sigma_T\Big[-G_{\gamma l} + \frac{1}{2}(F_{\gamma 2} + G_{\gamma 0} + G_{\gamma 2})\Big(\delta_{l0} + \frac{\delta_{l2}}{5}\Big)\Big]$$

For baryons we obtain equations of this kind:

$$\dot{\delta}_b = -\theta_b - \frac{1}{2}\dot{h}$$

$$\dot{\theta}_b = -\frac{\dot{a}}{a}\theta_b + c_s^2k^2\delta_b + \frac{4\overline{\rho}_\gamma}{3\overline{\rho}_b}an_e\sigma_T(\theta_\gamma - \theta_b)\ .$$

The sound speed comes from:

$$c_s^2 = \frac{\dot{P}_b}{\dot{\rho}_b} = \frac{k_BT_b}{\mu}\Big(1 - \frac{1}{3}\frac{d\ln T_b}{d\ln a}\Big)$$

where k_B is the Boltzmann constant, μ is the molecular weight and the temperature of baryons evolves accordingly to:

$$\dot{T}_b = -2\frac{\dot{a}}{a}T_b + \frac{8}{3}\frac{\mu}{m_e}\frac{\overline{\rho}_\gamma}{\overline{\rho}_b}an_e\sigma_T(T_\gamma - T_b)\ .$$

When Thomson drag terms become too large, equations can be simplified using the tight-coupling approximation [48].

Chapter 3

Bayesian analysis

'...Evidence... got a taste of evidence...'

Faith No More - Evidence

The classical *frequentist* definition of probability reads [63]:

> the probability is the number of times an event occurs over the total number of trials, in the limit of an infinite series of equiprobable repetitions.

It is clear that this kind of probability cannot be used in cosmological research, given that we cannot replicate the Universe to obtain a number of trials! Fortunately Bayesian statistics introduces a different concept of probability, namely:

> the probability is a measure of the degree of belief about a proposition.

To deal with these *degrees of belief* one has to refer to the Bayes' theorem, that I will show in next section. Bayesian approach can recover frequentist results on the long run, but can also be applied to situations that have no meaning in frequentist context, like a major part of the cosmological research. Other good points of Bayesian statistics are the natural inclusion of concepts like nuisance parameters, marginalisation and prior knowledge.

3.1 Bayes theorem

We define $p(A|I)$ the probability of the event A to occur, given a relevant information I about it. The *joint probability* of the events A and B is given by:

$$p(A, B|I) = p(A|B, I)p(B|I) \tag{3.1}$$

in practice equal to the probability of A to occur given the occurrence of B, multiplied by the probability of B to occur. We define then the *marginalised probability* of the event B as:

$$p(B|I) = \sum_A p(A, B|I) \tag{3.2}$$

where the sum counts all possible outcomes of A. From this starting point we can state the Bayes' theorem:

$$p(B|A, I) = \frac{p(A|B, I)p(B|I)}{p(A|I)} \ . \tag{3.3}$$

TWe now identify A with the observed data d, and B with the hypothesis to verify H:

$$p(H|d, I) = \frac{p(d|H, I)p(H|I)}{p(d|I)} \ . \tag{3.4}$$

On the left side of 3.4 we see the *posterior probability* of the hypothesis we are studying, given the data we have observed; on the right side we have the *likelihood* to observe those data given the hypothesis $p(d|H, I)$, multiplied by the prior probability of the hypothesis $p(H|I)$ and divided for the *marginal likelihood* or *Bayes evidence*:

$$p(d|I) = \sum_H p(d|H, I)p(H|I) \tag{3.5}$$

where the sum is over all possible hypothesis H. The meaning of this theorem is that when we infer something we include the prior knowledge that we have about it (assumptions) and we determine how likely is to observe the data that we have, given a determinate hypothesis. Even starting from different prior assumptions, when the likelihood is more informative than the prior, we should get to the same result. The key, then, is to have a great number of data points in order to make the likelihood override the prior.

When looking for the value of a parameter θ, in the choice of the prior, usually one looks for *ignorance priors*, that give the same probability to every possible hypothesis. The usual choice is the *flat prior*, that is a constant prior on an interval of parameter values:

$$p(\theta) = \frac{1}{\theta_{max} - \theta_{min}} \ .$$

A flat prior on θ, however, does not translate into a flat prior of a non-linear function of it, $\psi(\theta)$, indeed the two priors are related by:

$$p(\psi) = p(\theta)\frac{d\theta}{d\psi}$$

so that the flat prior on θ can result in a strongly informative prior on ψ. Finally, when dealing with quantities whose scale is not defined, one should use a *Jeffreys' prior*, a prior that is flat in $\ln\theta$.

3.2 Parameter estimation

Bayes' theorem shows its strength when we have to deal with a model M described by several parameters $\vec{\theta}$, whose value we want to infer starting from observed data d. In this vector of parameters we include physically interesting parameters $\vec{\phi}$ and nuisance parameters $\vec{\psi}$ (in cosmology the physically interesting parameters can be the six parameters representing the ΛCDM model, while the uninteresting nuisance parameters can be calibration values of the observations or fitting parameters of foregrounds' contamination). The posterior distribution of the whole set of parameters will be:

$$p(\vec{\theta}|d,M) = \frac{p(d|\vec{\theta},M)p(\vec{\theta}|M)}{p(d|M)} = \mathcal{L}(\vec{\theta})\frac{p(\vec{\theta}|M)}{p(d|M)} \ . \tag{3.6}$$

For parameter inference the normalization $p(d|M)$ is irrelevant, so we can simply ignore it. To obtain the probability distributions of the interesting parameters only, regardless of the nuisance ones, we can marginalise on the latter:

$$p(\vec{\phi}|d,M) = \int \mathcal{L}(\vec{\phi},\vec{\psi})p(\vec{\phi},\vec{\psi}|M)d\psi \ . \tag{3.7}$$

To obtain, now, the mean value of one of the $\vec{\phi}$ parameters or to study degeneracy of two or more of them we can simply marginalise over the others. This whole procedure can be carried out analytically only in few cases; usually the likelihood is computed sampling the parameter space with numerical techniques, like Monte-Carlo Markov Chains (MCMC), as we will see in detail in next section.

3.3 MCMC methods

An MCMC algorithm constructs a sequence of points in parameter space (a *chain*), whose density is proportional to the posterior probability distribution function. In practice a chain is a sequence of random points in parameter space, the probability of which depends only on the probability of the previous, that converges to a stationary state where successive elements of the chains are samples of the target distribution, in our case the posterior distribution $p(\vec{\theta}|d,M)$. Several algorithms can be used to construct these chains;

we will see in detail the classical Metropolis-Hastings algorithm, the one used in the `CosmoMC` code [64] employed in this work, and its modified fast-slow dragging version [65].

Metropolis-Hastings algorithm A chain starts from a point $\vec{\theta}_1$ in the parameter space and moves to another point $\vec{\theta}_2$ with a transition probability $T(\vec{\theta}_1, \vec{\theta}_2)$. This transition probability matrix T is chosen so that the stationary state of the Markov Chain is the probability distribution $p(\vec{\theta}) = p(\vec{\theta}|d, M)$ from which we wish to sample, the posterior. This is done using a *proposal density* $q(\vec{\theta}_i, \vec{\theta}_{i+1})$ to propose a new point $\vec{\theta}_{i+1}$ when in $\vec{\theta}_i$. This new point is accepted with probability:

$$\alpha(\vec{\theta}_i, \vec{\theta}_{i+1}) = min\left\{1, \frac{p(\vec{\theta}_{i+1})q(\vec{\theta}_{i+1}, \vec{\theta}_i)}{p(\vec{\theta}_i)q(\vec{\theta}_i, \vec{\theta}_{i+1})}\right\} \tag{3.8}$$

so that $T(\vec{\theta}_i, \vec{\theta}_{i+1}) = \alpha(\vec{\theta}_i, \vec{\theta}_{i+1})q(\vec{\theta}_i, \vec{\theta}_{i+1})$ and the detailed balance holds[1]:

$$p(\vec{\theta}_{i+1})T(\vec{\theta}_{i+1}, \vec{\theta}_i) = p(\vec{\theta}_i)T(\vec{\theta}_i, \vec{\theta}_{i+1}) \ . \tag{3.9}$$

If the proposal density is symmetrical (when it does not depend on the position, as for cosmological applications) it simply cancels out when the acceptance is computed, meaning that α depends only on the ratio of the posteriors. The choice of the proposal is important for the efficiency of the computation: the best choice is to take a proposal density similar in shape to the posterior, if one has an idea about what the posterior should look like. When we start a chain from a random point, it will take some time for the chain to reach equilibrium and start to sample from the posterior distribution. This time is called *burn in*, and points from this first stage are generally excluded from the analysis. Moreover, the chain is a correlated sample of the posterior distribution, in the sense that near points are correlated. To avoid this, the chains are usually *thinned*, namely, only occasional chain positions are retained, so to give time to the chain to move to an uncorrelated position in the parameter space.

Fast-slow dragging In cosmological application MCMC techniques are usually employed to analyse CMB spectral data. One can indeed calculate the likelihood of the observed C_ℓ with respect to some values of the model parameters by computing theoretical C_ℓ (refer to 1.32) using a Boltzmann

[1]The detailed balance ensures that the probability to move forward in the chain is the same as to move backward. This implies the reversibility of the chain.

code like `camb` and comparing the two. In this case the distinction between fast and slow parameters becomes important. The change of a fast parameter affects the likelihood function only marginally, so that the rescaling of the likelihood function is fast (think of spectral parameters or calibration uncertainties for what concerns the ΛCDM model), while the change of a slow parameter requires the full re-computation of the likelihood function (think to parameters of the model that affects the evolution of perturbations like densities).

Say we want to compute a likelihood $\mathcal{L}(\vec{x}, \vec{y})$ that depends on fast $\vec{y}$ and slow $\vec{x}$ parameters. Ideally one would like to use the Metropolis-Hastings algorithm on $\vec{x}$, using some proposal density $q(\vec{x}_{i+1}, \vec{x}_i)$ and accepting or rejecting the point $\vec{x}_{i+1}$ based on the marginal distribution $p(\vec{x})$. However this distribution is not known in practise. The idea behind the dragging method proposed by [65] is to make changes in $\vec{x}$ in conjunction with changes in $\vec{y}$ obtained by dragging $\vec{y}$ using intermediate fast re-computation of $\mathcal{L}(\vec{x}, \vec{y})$. This works better than just changing $\vec{x}$ while keeping $\vec{y}$ fixed. This latter method indeed works only if the old $\vec{y}$ is suitable for the new $\vec{x}^*$, and this is usually true only for small changes in $\vec{x}$. The new method drags $\vec{y}$ to a new $\vec{y}^*$ that, in the limit of a good transition probability T, should be more suitable for the new $\vec{x}^*$. This allows to make bigger steps in $\vec{x}$ while keeping the acceptance probability high enough.

Convergence diagnostic To understand if the chains have converged to the posterior distributions one has to use diagnostic methods. The one used in this work is the Gelman and Rubin algorithm [66]. This relies on a number of chains greater than one. Say one has m chains of n points. The quantities to compute for each parameter θ are the between-chains variance:

$$B = \frac{n}{m-1} \sum_{j=1}^{m} (\overline{\theta}_j - \overline{\theta})^2 \tag{3.10}$$

and the within-chain variance:

$$W = \frac{1}{m} \sum_{j=1}^{m} \Big[\frac{1}{n-1} \sum_{i=1}^{n} (\theta_{ij} - \overline{\theta}_j)^2 \Big] . \tag{3.11}$$

With these one can compute an overestimation of the marginal posterior variance of θ:

$$Var(\theta) = \frac{n-1}{n} W + \frac{1}{n} B \tag{3.12}$$

and because W is an underestimation of the within-chain variance, the Gelman-Rubin statistics monitors the convergence with the ratio:

$$\sqrt{R} = \sqrt{(\frac{n-1}{n} + \frac{m+1}{mn}\frac{B}{W})\frac{df}{df-2}} \tag{3.13}$$

where *df* are the degrees of freedom of the problem. The chains are considered converged if $R - 1 < 0.02$.

3.4 Model comparison

Bayes theorem can go further the estimation of parameters for a model. It can be used to compare models, and decide which one is more likely. It contains indeed a natural implementation of the *Occam razor*: the simpler, the better. It is clear that adding parameters to a model help to obtain a better fit to the data (think to the order of a polynomial fit). The question, then, is whether the improvement of the fit quality justifies the introduction of the extra parameters. Is the additional complexity needed by the data? To answer this question one must refer to the Bayesian evidence:

$$p(d|M) = \int p(d|\vec{\theta}, M)p(\vec{\theta}|M)d\theta \tag{3.14}$$

that is the average of the likelihood under the prior for a specific model choice. To determine the model's posterior probability we use again Bayes' theorem:

$$p(M|d) = \frac{p(M)p(d|M)}{p(d)} \ . \tag{3.15}$$

The probability of data $p(d)$ is taken equal to unity, so we can simply drop it. The prior on the model $p(M)$ is taken to be $1/N_M$ if one considers N different models. In comparing two models one needs to know the ratio of the posterior probabilities:

$$\frac{p(M_0|d)}{p(M_1|d)} = \frac{p(d|M_0)}{p(d|M_1)}\frac{p(M_0)}{p(M_1)} = B_{01}\frac{p(M_0)}{p(M_1)} \tag{3.16}$$

where B_{01} is known as Bayes factor. A value $B_{01} > 1$ represents an increase of the support in favour of model 0 versus model 1. The Bayes factor is usually interpreted on the basis of the Jeffreys' scale (Tab.3.1).

$\lvert \ln B_{01} \rvert$	strength of evidence
< 1.0	Inconclusive
1.0	Weak evidence
2.5	Moderate evidence
5.0	Strong evidence

Table 3.1: Jeffreys' scale of evidence of model 0 with respect to model 1, based on values of the Bayes factor B_{01}.

Savage-Dikey density ratio Computing the evidence, however, is usually difficult, because an integration over the entire parameter space is needed. Some methods can simplify the task (nested sampling, Laplace approximation) but for our intents we can refer to the Savage-Dickey density ratio (SDDR) [67]. This approximation is to be used with nested model comparison, those cases in which one of the two models to compare is a one-parameter extension of the other, and reduces to the latter for a particular value of the extra parameter. Suppose that we have a model with parameters $\vec{\theta}$ that is our 0 model, and an extension that adds to $\vec{\theta}$ the parameter ψ that is our model 1. Suppose also that the model 0 is recovered if $\psi = 0$. Under the assumption of separable prior spaces:

$$p(\vec{\theta}, \psi | M_1) = p(\psi | M_1) p(\vec{\theta} | M_0)$$

and the Bayes factor reduces to:

$$B_{01} = \left[\frac{p(\psi | d, M_1)}{p(\psi | M_1)} \right]_{\psi=0} . \tag{3.17}$$

In this case to compare two models one has to know the marginal posterior under the more complex model evaluated at the simpler model's parameter value, and the prior density of the more complex model at the same value. For a flat prior on the parameter ψ the latter is simply $p(\psi | M_1)|_{\psi=0} = 1/(\psi_{max} - \psi_{min})$.

Information criteria In more complex cases one can use approximations of the evidence known as information criteria [68]. These criteria comes under the assumption of a near-Gaussian posterior distribution, and so should be used with care.

Akaike Information Criterion (AIC)

This is derived from an approximate minimization of the Kullback–Leibler entropy, which quantifies the deviation between the true data distribution and the model distribution, and reads:

$$AIC = -2\ln\mathcal{L}_{max} + 2k \tag{3.18}$$

where $\mathcal{L}_{max}$ is the maximum likelihood value and k is the number of free parameters in the model. The best model is the one that minimises the AIC.

Bayesian Information Criterion (BIC)

This is an approximation of the Bayes factor itself, valid under the assumption of independent and identically distributed data-points (not the case for CMB) and is written:

$$BIC = -2\ln\mathcal{L}_{max} + k\ln N \tag{3.19}$$

where N is the number of data-points used, and again, the best model is the one that minimises the BIC.

Deviance Information Criterion (DIC)

This is based on the definition of an effective number of parameters p_D, that is the number of parameters actually constrained by data, also known as *Bayesian complexity*. We can compute the complexity as:

$$p_D = -2\ln\overline{\mathcal{L}(\vec{\theta})} + 2\ln\mathcal{L}(\vec{\bar{\theta}}) \tag{3.20}$$

and the DIC:

$$DIC = -2\mathcal{L}(\vec{\bar{\theta}}) + 2p_D = -4\ln\overline{\mathcal{L}(\vec{\theta})} + 2\ln\mathcal{L}(\vec{\bar{\theta}}) \tag{3.21}$$

where the averages are over the posterior distribution. This criterion does not penalise models for the unintended inclusion of unconstrained parameters as AIC and BIC do.

3.5 Decorrelation methods

We end this section with a topic that is not directly related to Bayesian analysis but that regards part of the following analysis. In cosmology we are usually interested in testing time variation of interesting quantities. This can be done slicing the space in red-shift bins, and determining the values of these parameters in each of them. In doing this we must keep in mind

that we work with observables that are integrated along the line of sight, meaning that a photon coming form a particular red-shift bin travelled along other bins to reach us. This translates in an intrinsic correlation between parameter estimates.

To solve this issue a decorrelation technique named Principal Component Analysis (PCA) is often used [69]. The PCA method starts with the set of correlated estimates of the parameter, θ_i (value of the parameter $\theta(z)$ in the i-th red-shift bin), and a correlation matrix between them. From here we can generally move in different directions.

One can use the PCA to restrict a parameter space. Assume that we binned our red-shift range in small slices, in each of which we compute the value of our quantity of interest $\theta(z)$. We end up with n correlated values θ_i. What we want here is to identify few decorrelated parameters that well represent the behaviour of our quantity. In this case the procedure is simple. The first step is to invert the covariance matrix $\mathbf{C}$ (nXn) to obtain the *Fisher information matrix* $\mathbf{F}$. This Fisher matrix has now to be diagonalized:

$$\mathbf{F} = \mathbf{W^T \Lambda W} \tag{3.22}$$

where the transformation matrix $\mathbf{W}$ contains in its rows the eigenvectors, while the eigenvalues are inside the $\mathbf{\Lambda}$ diagonal matrix. Keeping now only the eigenvectors $\mathbf{w}_j(z)$ associated with the few ($m << n$) highest eigenvalues α_j one can reconstruct to great accuracy the behaviour of $\theta(z)$ using just a number m of values. The function $\theta(z)$ will be reconstructed as a linear combination of the eigenvectors multiplied by their eigenvalues as weights:

$$\theta(z) = \sum_j \alpha_j \mathbf{w}_j(z) \ . \tag{3.23}$$

Clearly the bigger m, the more accurate the reconstruction. To understand why this procedure works just notice that, being the $\mathbf{F}$ matrix the inverse of the covariance, highest eigenvalues for $\mathbf{F}$ translates in lower variance. We are in practise keeping those modes that retain the most of the signal and discarding the noisy ones.

One can use PCA also in a 'localised' sense, and that is how I will use it in my work. Assume that we divide our space in few red-shift bins, because what we want is an estimate of the value of our quantity $\theta(z)$ precisely on those slices. As previously stated, the values we can obtain from our analysis will be correlated, with this correlation described by a correlation matrix. To obtain uncorrelated estimates of $\theta(z)$ in our bins we can follow the procedure developed by Huterer and Cooray [70], that diagonalizes the $\mathbf{F}$ matrix in such a way to obtain uncorrelated estimates of the θ_i that are, under certain

assumptions[2], still well localised inside the bins that we constructed. To do this we must diagonalize the **F** matrix with a different transformation matrix **O**:

$$\mathbf{F} = \mathbf{O^T O} \tag{3.24}$$

where in practice $\mathbf{O} = \mathbf{F^{1/2}}$. The rows of this new matrix **O** will be our weight functions. We normalise these rows to unity and combine them with the starting values θ_j to compute uncorrelated estimations ϕ_i of θ_i in this way:

$$\phi_i = \sum_j \mathbf{O}_{ij}\theta_j \ . \tag{3.25}$$

This method will give us a set of parameters ϕ_i that represent uncorrelated estimations of θ_i and that retain their localisation. This is given by the fact that the normalised i-th row of **O**, that acts as weight function for ϕ_i, is principally peaked in the i-th bin (and this clearly holds for a Fisher matrix that is nearly diagonal).

[2]For this procedure to work well, the Fisher matrix must be mostly positive and localised itself (nearly diagonal) [71].

Chapter 4

Neutrinos

...Just let the light touch you
And let the words spill through
And let them pass right through
Bringing out our hope and reason...'

Tool - Reflection

In this chapter I will focus on my research work about neutrino fundamental properties. Following the standard model one expects a number of neutrino equal to three, representing the three flavour eigenstates, characterised by small masses. Cosmology has two major tools to determine the number of the relativistic species beside the photons. The first is the nuclei formation process of the nucleosynthesis, strongly dependent on this value as we will see in next sections, that leads to verifiable predictions on the primordial abundances of light elements (^2H,^3He,^4He,^7Li). The second is the damping tail of the CMB, highly influenced by the presence of relativistic degrees of freedom in the primordial plasma. For what concerns the masses of the neutrinos, cosmology cannot resolve their value singularly, but it can place limits on the total sum of their masses, that acts on the CMB physics and, consequently, on the matter power spectrum of LSS.

To be more precise, the value that ones expects in cosmology for the number of neutrinos is equal to $N_{eff} = 3.046$, where the extra 0.046 comes from the fact that the decoupling of neutrinos from the primordial plasma was not an instantaneous process [72]. I will refer to this value as the standard.

Moreover, the fact that neutrinos act as standard radiation, that is represented by a sound speed and a viscosity parameter both equal to 1/3, is a mere assumption. Cosmology can help also in this case, because the plasma physics of the CMB is clearly affected by the clustering and viscosity properties of neutrinos.

4.1 Species and masses

WMAP satellite has been a milestone for CMB research. Its measurements of the anisotropies in the primordial plasma reached an astonishing precision and allowed the first highly accurate cosmological predictions from the CMB. WMAP was targeted to observe the first 1200 multipoles of the CMB power spectrum, that contain the first three peaks. From these it is possible to derive strong constraints on the relative amount of matter densities (baryons and CDM) and determine the geometry of the Universe, that appears to be flat. No information, however, comes from WMAP for what concerns the physics of the damping tail of the spectrum, the part that is at a major degree affected by neutrino properties.

Things changed with the measurements collected by two ground base experiments: ACT and SPT. Both these two telescopes indeed scrutinized the sky looking for the CMB signal at very small angular scales. At these small scales, however, the CMB signal must be cleaned from a number of foregrounds. Both ACT and SPT likelihoods marginalize over foreground parameters that aim to represent the behaviour of these spurious form of signal.

ACT uses in its likelihood multipoles $500 < \ell < 10000$ for the 148 GHz channel and $1500 < \ell < 10000$ for the 218 GHz. The foreground parameters marginalized over are amplitudes for kinetic and thermal Sunyaev-Zel'dovich effect, a_{kSZ} and a_{tSZ}, the power of clustered and Poisson Cosmic Infrared Background (CIB), a_c and a_p with emissivity β_c, the power of radio sources a_s, the residual Galaxy dust in southern and equatorial survey areas a_{gs} and a_{ge} and finally a correlation coefficient between tSZ and CIB sources ξ.

SPT likelihood is based on its observations in the 150 GHz channel and covers bandpowers $650 < \ell < 3000$. The foregrounds are modelled with four additional parameters: an amplitude for the Poisson CIB sources D^{PS}_{3000}, one for the clustered D^{CL}_{3000}, and finally, for the SZ effect, the total power D^{SZ}_{3000} and a spectral index f^{SZ}_{ℓ}. In Fig.4.1 I report measurements of the CMB power spectrum from WMAP 9 year, ACT and SPT up to $\ell = 3000$. It clearly shows the differences in the measurements obtained by the two high-ℓ experiments. The effect of this discrepancies is particularly visible in the results obtained for 3 cosmological parameters: N_{eff}, the number of relativistic species, $\sum m_\nu$ the sum of the neutrino masses and A_L the amplitude of the lensing effect on the CMB. The number of relativistic species is defined starting from the total radiation density:

$$\rho_{\rm rad} = \left[1 + \frac{7}{8}\left(\frac{4}{11}\right)^{\frac{4}{3}} N_{eff}\right]\rho_\gamma \tag{4.1}$$

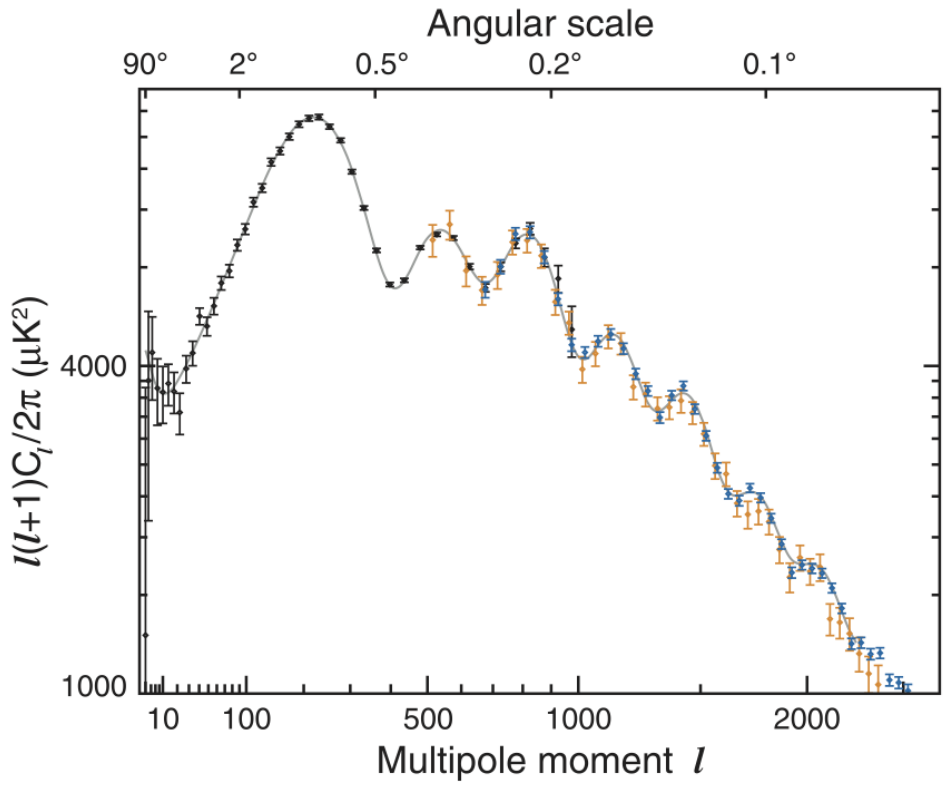

Figure 4.1: CMB power spectrum as measured by WMAP 9 years (black points), ACT (orange points) and SPT (blue points) up to multipole 3000 [4]. The discrepancies between ACT and SPT measurements is clearly visible.
.

where the relation between photons and other relativistic degrees of freedom comes imposing entropy conservation at the time at which the latter decouples. The sum of the masses of the neutrinos, expressed in eV, can be computed starting from the value of their density in this way:

$$\Omega_\nu h^2 = \frac{\sum m_\nu}{93eV} \tag{4.2}$$

Finally, the lensing parameter is defined in [73] in this way:

$$C_\ell^{\phi\phi} \rightarrow A_L C_\ell^{\phi\phi} \tag{4.3}$$

being in practise a rescaling of the lensing power spectrum. The expected value, if the general relativistic treatment of the lensing of the CMB is correct, should be $A_L = 1$. The values the two experiments obtained for these

parameters are reported in the first two columns of Tab.4.1. They refer to results obtained in ΛCDM one-parameter extensions, so varying the standard 6 parameters of the base model plus the single extra parameter under study. Looking at the numerical values, one can say that ACT experiment recovers a standard neutrino number, with a mass value compatible with zero, while the value of the lensing amplitude parameter is extremely higher with respect to the standard expectation of unity. SPT, on the other hand, shows a slightly preference for a higher number of neutrino species, an indication for a non-null value of their sum of masses (the lower limit at 68% c.l. is $\sum m_\nu = 0.41$ [38]) and a lensing amplitude parameter compatible with one within one σ. The inclusion of H_0 and BAO measurements in the likelihood raises the number of neutrino species in both cases, with no particular effect on the lensing amplitude.

Parameters	WMAP7+**ACT**	WMAP7+**SPT**	**Planck**+WP
N_{eff}	2.79 ± 0.56	3.68 ± 0.48	3.51 ± 0.39
$\sum m_\nu$	< 0.70 (95%*c.l.*)	< 1.60 (95%*c.l.*)	< 0.933 (95%*c.l.*)
A_l	1.70 ± 0.38	$0.86^{+0.15}_{-0.13}$	$1.22^{+0.11}_{-0.13}$

Table 4.1: Debated parameters values from ACT and SPT experiments combined with WMAP 7 years low-ℓ data and from Planck temperature measurements combined with WMAP9 polarization data. Confidence limits are at 68% for two-tailed distributions, at 95% for one-tailed distributions. The tension between the different experiments is strong.

One can study the results of this two experiments trying multi-parameter extensions of the ΛCDM base model, combining together these debated parameters, that, given their mutual effects on the damping tail of the CMB, show important degeneracy among each other. I used the MCMC code `CosmoMC` in combination with the Boltzmann code `camb` to solve the perturbation equations for a ΛCDM+N_{eff}+A_L model and study the change in the likelihood function in response to a variation of the parameters. Beside calibration and foreground parameters I let free to vary the following 8 cosmological parameters:

$\Omega_b h^2$ the physical density for baryons, imposing a flat prior on it in the range $[0.005; 0.1]$;

$\Omega_c h^2$ the physical density for CDM, imposing a flat prior on it in the range $[0.001; 0.99]$;

θ the ratio of the sound horizon to the angular diameter distance, a parameter that encodes the H_0 dependence in a faster way for the chains

convergence. I used a flat prior on it $[0.5; 10.0]$;

τ the re-ionization optical depth, defined as:

$$\tau = \int_0^{z_{re}} dz \sigma_T n_e(z) c \frac{dt}{dz}$$

where z_{re} is the re-ionization red-shift, σ_T is the Thomson scattering cross section and $n_e(z)$ is the number of free electrons. I imposed a flat prior on it inside $[0.01; 0.8]$;

n_s the spectral index of the primordial spectrum, with a flat prior on it inside $[0.9; 1.1]$;

$\log(10^{10} A_s)$ the amplitude of the primordial spectrum referred to $k = 0.002$ Mpc $^{-1}$ (WMAP) or $k = 0.05$ Mpc^{-1} (Planck), with a flat prior on it inside $[2.7; 4.0]$;

N_{eff} the number of relativistic species defined in 4.1, imposing a flat prior in the range $[0.047; 10.0]$;

A_L the lensing amplitude parameter introduced in 4.3, with a flat prior inside $[0; 4]$.

The results obtained with this analysis are reported in [74]. I combined ACT and SPT data with WMAP 9 years measurements (in perfect agreement with the WMAP 7 years measurements) and tried to simultaneously vary the number of relativistic species N_{eff} and the lensing amplitude A_L. I add also HST H_0 measurement and BAO data from 6dFGRS, SDSS-DR7, SDSS-Dr9, WiggleZ (refer to Section 1.3.1 for references). Results are reported in Fig.4.2, left panel being the CMB-only case and right panel the CMB+HST+BAO case. The plots show clearly the discrepancy between the two experiments results, discrepancy that is even higher with the inclusion of the low-red-shift data. The inclusion of the HST and BAO measurements increases the tension in that it reduces the confidence limits. I found that for WMAP9+SPT+BAO+HST at 95% $A_L < 1.07$ while for WMAP9+ACT+HST+BAO at 95% $A_L > 1.13$, showing clearly the discrepancies in the results of the two experiments. Numerical values for cosmological parameters are also reported, refer to table Tab.4.2. From here one can see that also values of other parameters are not in agreement, even if at a minor level. As an example I report the degeneracy among $\Omega_b h^2$ and n_s and that among $\Omega_c h^2$ and H_0 in Fig.4.3.

I continued the analysis including the variation of the neutrino masses. I used ACT and SPT in combination with WMAP+BAO+HST and try

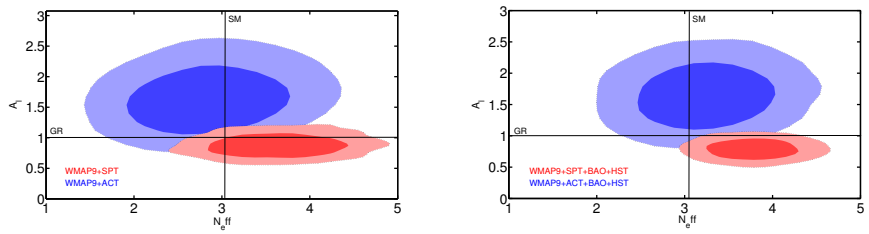

Figure 4.2: The plot reports the 2D contours of the posterior distributions for N_{eff} and A_L (ACT in blue and SPT in red). Left panel shows results for CMB-only analysis while right panel shows results when also H_0 prior from HST and BAO information are added. The two experiments give results that are in tension for both the parameters. The inclusion of low-z data enhances this tension lowering the confidence intervals.

.

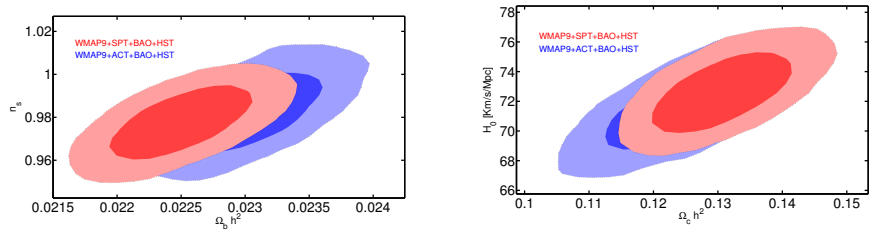

Figure 4.3: The plot reports the 2D contours of the posterior distributions for $\Omega_b h^2$ and n_s (left panel) and for $\Omega_c h^2$ and H_0 (right panel). ACT contours are blue and SPT are red, and refer to results from CMB+HST+BAO analysis. Discrepancies in these parameters values are at a minor level.

.

two different approach: varying only number and masses of the neutrinos, fixing the lensing amplitude to its nominal value of one, or varying the three parameters together. To vary the mass of the neutrinos I added $\sum m_\nu$ (refer to 4.2) to the parameter set, imposing a prior on it in the range $[0.0; 5.0]$. The indication for a non-null sum of the masses from SPT disappears if the lensing amplitude is left free to vary. Fixing A_L to unity indeed drags the sum of the neutrino masses to higher values, to decrease the effect of lensing, that SPT measures smaller than one. This is visible in Fig.4.4, where I report the posterior distributions for the sum of the neutrino masses obtained fixing and varying the lensing amplitude. The simultaneous variation of $\sum m_\nu$ for SPT lift a bit the value of the number of species too. ACT stays in

Parameters	**SPT** +WMAP9	**ACT** +WMAP9	**SPT** +WMAP9+HST+BAO	**ACT** +WMAP9+HST+BAO
$\Omega_b h^2$	0.02264 ± 0.00051	0.02283 ± 0.00052	0.02250 ± 0.00034	0.02301 ± 0.00036
$\Omega_c h^2$	0.1232 ± 0.0080	0.110 ± 0.010	0.1308 ± 0.0067	0.1250 ± 0.0078
$100\,\theta$	1.0415 ± 0.0012	1.0412 ± 0.0025	1.0409 ± 0.0010	1.0388 ± 0.0021
τ	0.088 ± 0.014	0.090 ± 0.014	0.084 ± 0.013	0.087 ± 0.013
n_s	0.982 ± 0.018	0.969 ± 0.019	0.978 ± 0.011	0.983 ± 0.012
$\log(10^{10} A_s)$	3.169 ± 0.048	3.174 ± 0.045	3.198 ± 0.032	3.115 ± 0.034
N_{eff}	3.72 ± 0.46	2.85 ± 0.56	3.78 ± 0.33	3.54 ± 0.41
A_L	0.85 ± 0.13	1.64 ± 0.36	0.79 ± 0.11	1.64 ± 0.32
H_0[km/s/Mpc]	74.6 ± 3.7	69.9 ± 3.7	72.7 ± 1.7	71.7 ± 1.9
Ω_Λ	0.736 ± 0.023	0.728 ± 0.025	0.710 ± 0.010	0.712 ± 0.011
Ω_m	0.264 ± 0.023	0.272 ± 0.025	0.290 ± 0.010	0.288 ± 0.011
Age/Gyr	13.14 ± 0.43	13.90 ± 0.55	13.10 ± 0.27	13.3 ± 0.34

Table 4.2: Cosmological parameters values and 68 % confidence level errors. The SPT and ACT datasets produce different values for some of the parameters, most notably N_{eff} and A_L.

agreement with a standard number of species and with a null mass, but the value of the lensing amplitude in this case is even higher than before, reaching $A_L = 1.78 \pm 0.38$, more than two standard deviations from the standard scenario. Numerical values for this analysis are in Tab.4.3 while Fig.4.5 reports the degeneracy between $\sum m_\nu$ and A_L for both the experiments.

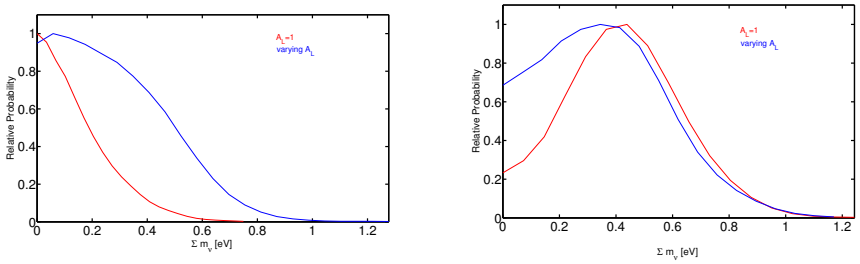

Figure 4.4: Posterior distributions for the sum of the neutrino masses, obtained varying only N_{eff} (red line) and fixing $A_L = 1$ or varying both parameters (blue line). Left panel shows results for WMAP9+ACT+HST+BAO, right panel for WMAP9+SPT+HST+BAO. It is clear how the inclusion of a variable lensing amplitude makes the evidence for a neutrino mass claimed by SPT disappear.

.

After SPT and ACT results, Planck space mission released its first data of the TT power spectrum of the CMB. Planck likelihood is a hybrid likelihood [5] that uses a component separation technique on the 91% of the sky for the multipoles $1 < \ell < 50$ and cross spectra from 100 ($f_{sky} = 58\%$), 143 and 217 GHz ($f_{sky} = 37\%$) for the remaining multipoles up to $\ell = 2500$. In this high-ℓ likelihood several foreground parameters are included and

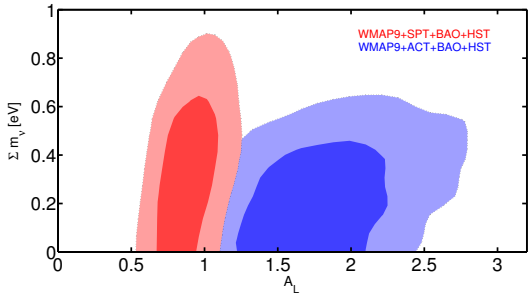

Figure 4.5: This is the plot of the degeneracy among the sum of the neutrino masses and the lensing parameter, for the cases WMAP9+SPT+HST+BAO (red) and WMAP9+ACT+HST+BAO (blue). A higher value of the lensing parameter allows for a higher neutrino mass.

.

Parameters	**SPT** +WMAP9+HST+BAO	**SPT** +WMAP9+HST+BAO	**ACT** +WMAP9+HST+BAO	**ACT** +WMAP9+HST+BAO
$\Omega_b h^2$	0.02279 ± 0.00036	0.02271 ± 0.00039	0.02305 ± 0.00038	0.02317 ± 0.00038
$\Omega_c h^2$	0.1325 ± 0.0074	0.1323 ± 0.0074	0.1224 ± 0.0076	0.1248 ± 0.0077
$100\,\theta$	1.0410 ± 0.0011	1.0410 ± 0.0011	1.0393 ± 0.0021	1.0393 ± 0.0021
τ	0.088 ± 0.013	0.089 ± 0.014	0.094 ± 0.015	0.091 ± 0.014
n_s	0.989 ± 0.012	0.987 ± 0.013	0.985 ± 0.012	0.988 ± 0.013
$\log(10^{10} A_s)$	3.157 ± 0.034	3.168 ± 0.037	3.117 ± 0.038	3.115 ± 0.034
N_{eff}	3.94 ± 0.37	3.92 ± 0.37	3.40 ± 0.39	3.56 ± 0.40
$\sum m_\nu$[eV]	< 0.76 (95% *c.l.*)	< 0.74 (95% *c.l.*)	< 0.41 (95% *c.l.*)	< 0.53 (95% *c.l.*)
A_L	1.00	0.90 ± 0.14	1.00	1.82 ± 0.38
H_0[km/s/Mpc]	72.2 ± 1.9	72.2 ± 1.9	70.5 ± 1.9	71.1 ± 1.8
Ω_Λ	0.702 ± 0.012	0.702 ± 0.012	0.708 ± 0.011	0.707 ± 0.011
Ω_m	0.298 ± 0.012	0.298 ± 0.012	0.292 ± 0.011	0.293 ± 0.011
Age/Gyr	13.12 ± 0.29	13.09 ± 0.31	13.47 ± 0.33	13.36 ± 0.33

Table 4.3: Cosmological parameters values and 68 % confidence level errors for the analysis that consider massive neutrinos.

marginalised over, Tab.4.4 reports all of them.

Instead of showing agreement with one of the two discording experiments, Planck obtains results for these three parameters that are in between the previous, almost for what concerns N_{eff} and A_L. The sum of neutrino masses indicated by Planck is indeed compatible with zero, enforcing our idea that the indication for a non-null mass in SPT comes from fixing the lensing amplitude to a higher value than the measured one. Column three of Tab.4.1 reports the values obtained for the three parameter using Planck TT spectrum data in combination with WMAP 9 years polarization data (WP). From these values we can see how Planck seems to agree with SPT with respect to the number of relativistic species, while being similar to ACT indicating a value for the lensing amplitude higher than one, as one can clearly see from the posteriors of the two extra parameters for the three experiments

A^{PS}_{100}	Poisson point-source power for 100 GHz channel
A^{PS}_{143}	Poisson point-source power for 143 GHz channel
A^{PS}_{217}	Poisson point-source power for 217 GHz channel
$r^{PS}_{143x217}$	Poisson source correlation coefficient for 143 and 217 GHz channel
A^{CIB}_{143}	CIB power for 217 GHz channel
A^{CIB}_{217}	CIB power for 217 GHz channel
$r^{CIB}_{143x217}$	CIB correlation coefficient for 143 and 217 GHz channel
γ^{CIB}	spectral index of the CIB power spectrum
A^{tSZ}	thermal SZ contribution (143 GHz)
A^{kSZ}	kinetic SZ contribution
$\xi^{tSZxCIB}$	correlation coefficient between tSZ and CIB
c_{100}	calibration between 100 and 143 GHz channels power spectra
c_{217}	calibration between 217 and 143 GHz channels power spectra
β^1_1	beam parameter

Table 4.4: Foreground and calibration parameters for Planck high-ℓ likelihood.

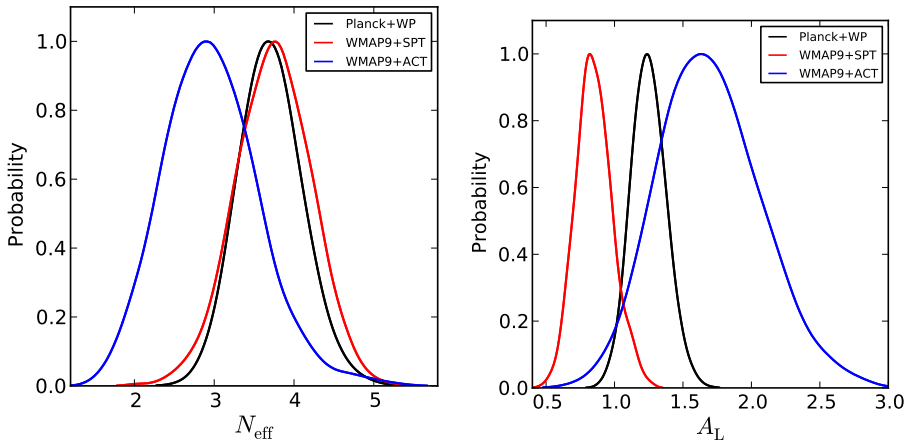

Figure 4.6: Here I present posteriors for N_{eff} and A_L for the three different experiments (ACT in blue, SPT in red and Planck in black) in one-parameter extensions of the ΛCDM analysis. We can see clearly the agreement on the number of relativistic species between Planck and SPT and the in-between value of the lensing amplitude measured by Planck.

.

(SPT+WMAP9, ACT+WMAP9, Planck+WP) reported in Fig.4.6.

I then performed a similar analysis using Planck dataset to constrain parameters for a ΛCDM+N_{eff}+A_L model, as discussed in [75]. A plot of the 2-dimensional posteriors for the different datasets is reported in Fig.4.8 and shows the good agreement with SPT and the strong discrepancy with ACT results in terms of number of relativistic species. That plot comes from CMB data only. Adding HST prior on H_0 confirms the indication for

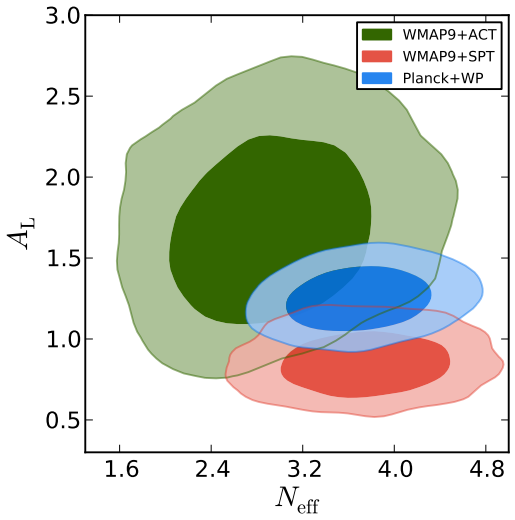

Figure 4.7: This plot shows 2D contours for N_{eff} and A_L for the three different experiments (ACT in green, SPT in red and Planck in blue) in our two-parameter extension of the ΛCDM analysis. The agreement with SPT number of relativistic species is evident.

.

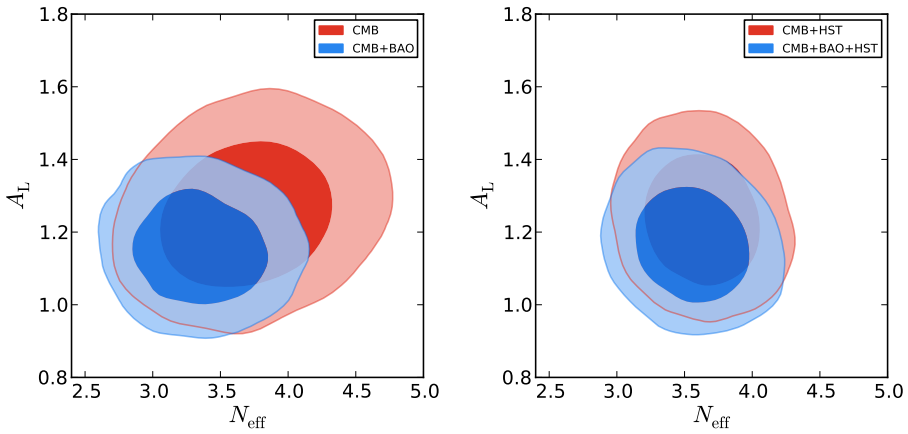

Figure 4.8: Left panel reports the 2D contours in the plane $N_{eff} - A_L$ for Planck+WP alone (red) and for Planck+WP+BAO (blue). On the right we have contours for Planck+WP+HST (red) and for Planck+WP+HST+BAO (blue). BAO inclusion pushes values closer to standard expectations.

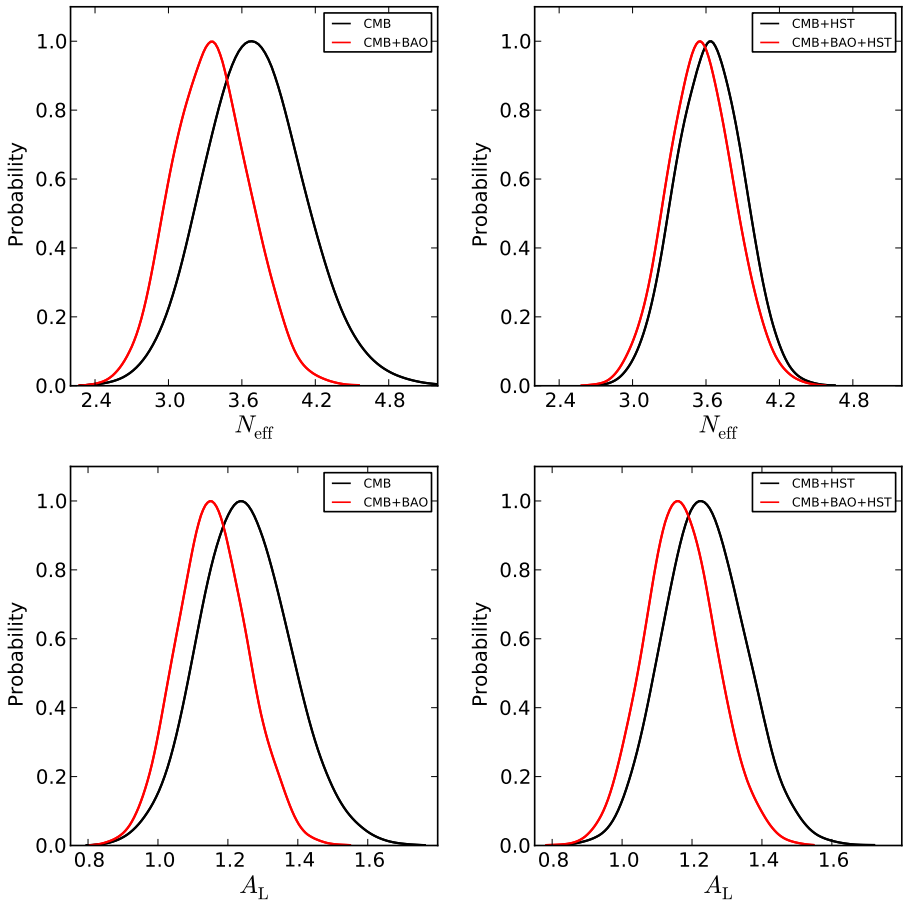

Figure 4.9: Here I present posteriors for N_{eff} (upper row) and A_L (lower row) obtained letting the two parameters vary together. On the left we have results from Planck+WP (black line) and Planck+WP+BAO (red line), on the right results from Planck+WP+HST (black line) and from Planck+WP+HST+BAO (red line). For both the parameters the BAO data indicate a value closer to the standard.

.

a number of relativistic species higher than the standard, while BAO data (only SDSS-DR7, SDSS-DR9 and WiggleZ) push the posterior to lower and standard values (see Fig.4.9). Also for the lensing amplitude parameter the HST prior confirms the higher value, while the BAO information tend to move the posterior to lower values closer to the standard unity. Numerical values are in Tab.4.5.

In general, however, the addition of both BAO and HST measurements to

Parameters	Planck+WP	Planck+WP+HST	Planck+WP+BAO	Planck+WP+BAO+HST
$\Omega_b h^2$	0.02306 ± 0.00051	0.022953 ± 0.00035	0.02246 ± 0.00031	0.02262 ± 0.00028
$\Omega_c h^2$	0.1239 ± 0.0054	0.1234 ± 0.0050	0.1232 ± 0.0053	0.1260 ± 0.0049
$100\,\theta$	1.04124 ± 0.00077	1.04123 ± 0.00077	1.04112 ± 0.00078	1.04085 ± 0.00075
τ	0.095 ± 0.015	0.094 ± 0.014	0.087 ± 0.013	0.089 ± 0.013
n_s	0.996 ± 0.018	0.992 ± 0.011	0.974 ± 0.011	0.9815 ± 0.0088
$\log(10^{10} A_s)$	3.111 ± 0.034	3.108 ± 0.030	3.093 ± 0.030	3.103 ± 0.029
N_{eff}	3.71 ± 0.40	3.63 ± 0.27	3.35 ± 0.31	3.56 ± 0.27
A_L	1.25 ± 0.13	1.24 ± 0.12	1.16 ± 0.10	1.17 ± 0.10
H_0[km/s/Mpc]	74.9 ± 3.7	74.0 ± 2.0	70.4 ± 1.9	71.8 ± 1.6
Ω_Λ	0.736 ± 0.022	0.733 ± 0.014	0.706 ± 0.011	0.7119 ± 0.0094
Ω_m	0.264 ± 0.022	0.267 ± 0.014	0.294 ± 0.011	0.2881 ± 0.0094
Age/Gyr	13.08 ± 0.38	13.15 ± 0.23	13.47 ± 0.28	13.27 ± 0.23

Table 4.5: Constraints at 68 % confidence level on cosmological parameters from the analysis using Planck+WP+HST, Planck+WP+BAO and Planck+WP+BAO+HST.

the Planck dataset hints for a number of relativistic species higher than the expected and for a lensing amplitude also higher. The result on N_{eff} is found also using SPT data, that, on the contrary, indicate a lensing amplitude value lower than the expected. So, while the first result can really be a hint for new physics to take in account, the second seems more to be a systematic effect. Three CMB experiments obtain three different values for the same parameter, none of which is the expected one. Moreover, playing with other CMB damping tail parameters like N_{eff} or $\sum m_\nu$ in anyway a standard value for A_L cannot be properly recovered. Another indication for this strange value of A_L to be caused by a systematic is the fact that the same parameter computed on the tri-spectrum instead of the spectrum results in $A_L^{\phi\phi} = 0.99 \pm 0.05$.

4.2 Clustering parameters

Another way the neutrinos can affect the damping of the CMB acoustic oscillations is via their clustering properties. Is indeed assumed that neutrinos behave like radiation also in clustering, but this is far from being proved. The clustering properties of a fluid are defined with the help of two parameters: the rest-frame sound speed c^2_{eff} and the viscosity parameter c^2_{vis}. The former represents the ratio among pressure and density perturbations of the fluid, while the latter is given by its anisotropic stress. Both these quantities should be equal to 1/3 to reproduce clustering properties typical of a radiation fluid.

To study these features we can describe neutrinos as *generalised dark matter*, as proposed by Hu in [76]. This leads to a change in the neutrino

perturbation equations of 2.26, that in this case read [77]:

$$\dot{\delta}_\nu = \frac{\dot{a}}{a}\left(1-3c_{\rm eff}^2\right)\left(\delta_\nu + 3\frac{\dot{a}}{a}\frac{q_\nu}{k}\right) - k\left(q_\nu + \frac{2}{3k}\dot{h}\right) \tag{4.4}$$

$$\dot{q}_\nu = k\, c_{\rm eff}^2\left(\delta_\nu + 3\frac{\dot{a}}{a}\frac{q_\nu}{k}\right) - \frac{\dot{a}}{a}q_\nu - \frac{2}{3}k\pi_\nu \tag{4.5}$$

$$\dot{\pi}_\nu = 3\, c_{\rm vis}^2\left(\frac{2}{5}q_\nu + \frac{8}{15}\sigma\right) - \frac{3}{5}kF_{\nu,3} \tag{4.6}$$

$$\frac{2l+1}{k}\dot{F}_{\nu,l} - lF_{\nu,l-1} = -\left(l+1\right)F_{\nu,l+1}\ \ l \geq 3\ . \tag{4.7}$$

The effective sound speed enters the equations of density and momentum perturbations, while the viscosity parameter acts on the anisotropic stress.

To perform this analysis I modified `camb` to include the new parameters, on which I imposed a flat prior inside the range $[0;1]$. Differently from the analysis of the previous section, the $\sum m_\nu$ is kept fixed to 0.06 rather than to zero. I used as datasets Planck+WP alone, Planck+WP+BAO+HST and Planck+WP+lensing. The BAO data-points included in this analysis are those from 6dFGRS, SDSS-DR7 and SDSS-DR9. Results are published in [78] and reported in first column of Tab.4.6 for Planck+WP, first column of 4.7 for Planck+WP+BAO+HST and in first column of Tab.4.8 for Planck+WP+lensing. In general we see a trend for $c_{\rm eff}^2$ (0.304 ± 0.013 in the Planck+WP case) to be a bit lower than the expectation, and for $c_{\rm vis}^2$ to be higher (0.60 ± 0.18 in the Planck+WP case). In between two standard deviations, however, the standard values are recovered. The inclusion of low-z measurements or of Planck lensing likelihood drags the values closer to standard assumptions.

Parameters	$+c_{\rm vis}^2 + c_{\rm eff}^2$	$+c_{\rm eff}^2 + A_L$	$+c_{\rm vis}^2 + A_L$	$+c_{\rm eff}^2 + c_{\rm vis}^2 + A_L$
$\Omega_b h^2$	0.02118 ± 0.047	0.02219 ± 0.045	0.02236 ± 0.053	0.02162 ± 0.095
$\Omega_c h^2$	0.1157 ± 0.0038	0.1177 ± 0.0032	0.1170 ± 0.0034	0.1159 ± 0.0036
$100\,\theta$	1.0412 ± 0.0014	1.0428 ± 0.0012	1.0421 ± 0.0019	1.0420 ± 0.0020
$\log(10^{10}A_s)$	3.173 ± 0.052	3.086 ± 0.028	3.08 ± 0.05	3.141 ± 0.078
τ	0.089 ± 0.013	0.088 ± 0.013	0.087 ± 0.013	0.089 ± 0.014
n_s	0.998 ± 0.018	0.9732 ± 0.0099	0.970 ± 0.014	0.989 ± 0.023
A_L	1	1.16 ± 0.13	1.20 ± 0.12	1.08 ± 0.18
$c_{\rm vis}^2$	0.60 ± 0.18	0.33	0.35 ± 0.12	0.51 ± 0.22
$c_{\rm eff}^2$	0.304 ± 0.013	0.321 ± 0.014	0.33	0.311 ± 0.019
H_0[km/s/Mpc]	68.0 ± 1.3	68.7 ± 1.5	68.9 ± 1.5	68.6 ± 1.7

Table 4.6: Results for different combinations of extra parameters for Planck+WP dataset at 68% c.l..

I decided to add as free parameter also the lensing amplitude A_L and try different combinations of extra parameters, in order to determine whether the degeneracy among these three can some way correct the huge value of

Parameters	$+c^2_{\rm vis}+c^2_{\rm eff}$	$+c^2_{\rm eff}+A_L$	$+c^2_{\rm vis}+A_L$	$+c^2_{\rm eff}+c^2_{\rm vis}+A_L$
$\Omega_b h^2$	0.02142 ± 0.048	0.02228 ± 0.037	0.02258 ± 0.043	0.02209 ± 0.091
$\Omega_c h^2$	0.1160 ± 0.0025	0.1171 ± 0.0018	0.1173 ± 0.0023	0.1167 ± 0.0024
$100\,\theta$	1.0417 ± 0.0016	1.0427 ± 0.0011	1.0429 ± 0.0018	1.0426 ± 0.0018
$\log(10^{10} A_s)$	3.158 ± 0.050	3.084 ± 0.028	3.065 ± 0.043	3.104 ± 0.075
τ	0.091 ± 0.013	0.088 ± 0.013	0.087 ± 0.013	0.088 ± 0.013
n_s	0.993 ± 0.016	0.9737 ± 0.0080	0.967 ± 0.012	0.978 ± 0.023
A_L	1	1.18 ± 0.12	1.23 ± 0.11	1.15 ± 0.17
$c^2_{\rm vis}$	0.53 ± 0.16	0.33	0.302 ± 0.097	0.40 ± 0.19
$c^2_{\rm eff}$	0.306 ± 0.013	0.322 ± 0.013	0.33	0.319 ± 0.019
H_0[km/s/Mpc]	68.29 ± 0.74	68.93 ± 0.80	69.16 ± 0.87	68.88 ± 0.99

Table 4.7: Results for different combinations of extra parameters for Planck+WP+BAO+HST dataset at 68% c.l..

Parameters	$+c^2_{\rm vis}+c^2_{\rm eff}$	$+c^2_{\rm eff}+A_L$	$+c^2_{\rm vis}+A_L$	$+c^2_{\rm eff}+c^2_{\rm vis}+A_L$
$\Omega_b h^2$	2.155 ± 0.049	2.214 ± 0.038	2.217 ± 0.046	2.166 ± 0.063
$\Omega_c h^2$	0.1151 ± 0.0034	0.1171 ± 0.0030	0.1159 ± 0.0034	0.1151 ± 0.0037
$100\,\theta$	1.0414 ± 0.0015	1.0426 ± 0.0012	1.0415 ± 0.0018	1.0415 ± 0.0017
$\log(10^{10} A_s)$	3.146 ± 0.054	3.084 ± 0.027	3.094 ± 0.051	3.137 ± 0.064
τ	0.090 ± 0.013	0.088 ± 0.013	0.088 ± 0.013	0.088 ± 0.013
n_S	0.990 ± 0.019	0.9726 ± 0.0098	0.974 ± 0.015	0.989 ± 0.021
A_L	1	1.042 ± 0.072	1.057 ± 0.070	1.025 ± 0.076
$c^2_{\rm vis}$	0.52 ± 0.18	0.33	0.39 ± 0.14	0.50 ± 0.19
$c^2_{\rm eff}$	0.312 ± 0.013	0.322 ± 0.012	0.33	0.314 ± 0.015
H_0[km/s/Mpc]	68.5 ± 1.1	68.8 ± 1.4	68.9 ± 1.4	68.8 ± 1.5

Table 4.8: Results for different combinations of extra parameters for Planck+WP+lensing dataset at 68% c.l..

the lensing amplitude obtained in the ΛCDM scenario by Planck. Plots 4.10, 4.11 and 4.12 report the parameter posteriors in the various cases (different combinations of parameters and datasets).

For what concerns the sound speed it is worth to notice that the simultaneous variation of the lensing parameter pushes the results towards the standard value. Datasets combinations give very similar results, the inclusion of lensing enlarges the posterior enhancing the agreement with the standard value 1/3. The viscosity parameter seems to be higher than 1/3, but again, including the lensing amplitude as a free parameter can reconcile its value with the expectations. Planck lensing dataset in this case slightly tighten the posterior and drag it closer to the standard. A unitary value for A_L, instead, can be recovered only when both the clustering parameters for neutrinos are free to vary, or including the lensing information. Summarising, the simultaneous variation of the three parameters can recover standard results for all, even including only CMB spectrum information, giving $c^2_{\rm eff} = 0.319 \pm 0.019$, $c^2_{\rm vis} = 0.51 \pm 0.22$ and $A_L = 1.08 \pm 0.18$. The inclusion of the lensing likelihood maintains this agreement while tightening the constraints, giving $c^2_{\rm eff} = 0.0.314 \pm 0.015$, $c^2_{\rm vis} = 0.50 \pm 0.19$ and

$A_L = 1.025 \pm 0.076$.

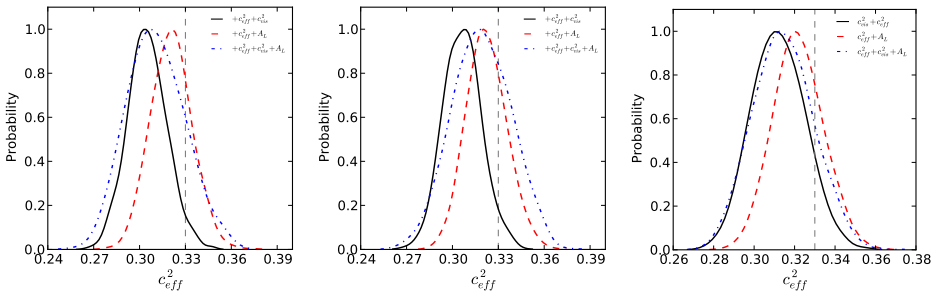

Figure 4.10: Here I present posteriors for $c^2_{\rm eff}$ in the analysis of Planck+WP (left), Planck+WP+BAO+HST (center) and Planck+WP+lensing (right). In each plot different lines refer to different parameters combinations. For each dataset choice varying the $c^2_{\rm eff}$ and A_L together recovers agreement with standard expectations. The variation of the three parameters all together enlarges the posteriors obtaining the same result.

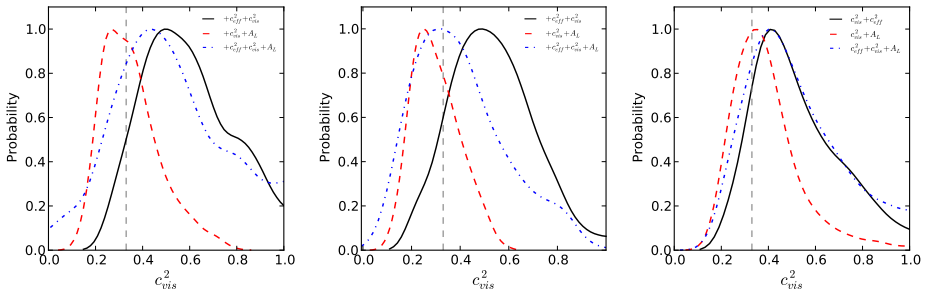

Figure 4.11: Here I present posteriors for $c^2_{\rm vis}$ in the analysis of Planck+WP (left), Planck+WP+BAO+HST (center) and Planck+WP+lensing (right). In each plot different lines refer to different parameters combinations. The simultaneous variation of the parameters gives results closer to the standard.

It is worth noticing how the clustering parameters act also on the spectral parameters, given the strong degeneracy among them. This correlation is reported in Fig.4.13 for the sound speed and in Fig.4.14 for the viscosity parameter. The former shows a negative degeneracy with the inflationary parameters, while the latter presents a positive correlation. The degeneracy of the sound speed is partially removed if the lensing amplitude parameter is let free to vary. Finally, correlations between A_L and the clustering parameters are shown in Fig.4.15.

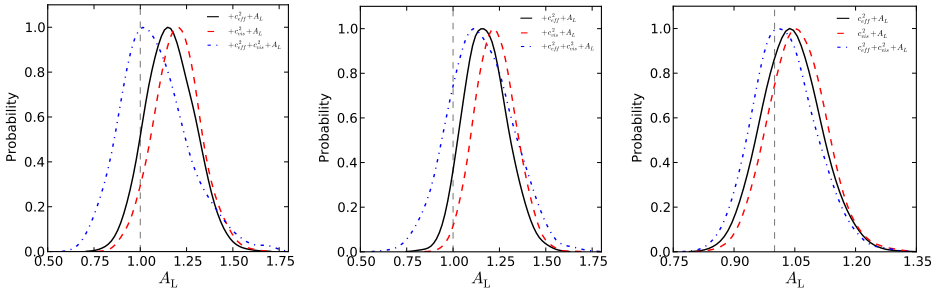

Figure 4.12: Here I present posteriors for A_L in the analysis of Planck+WP (left), Planck+WP+BAO+HST (center) and Planck+WP+lensing (right). In each plot different lines refer to different parameters combinations. A unitary value for A_L is recovered when all the three parameters are let free to vary.

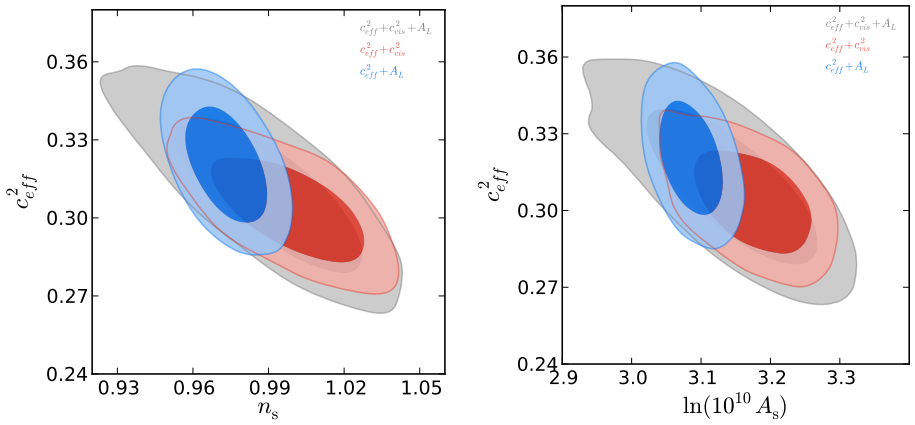

Figure 4.13: 2D contours for $c^2_{\rm eff}$ and the spectral parameters n_s (left) and A_s (right) in the Planck+WP case. Grey contours are for the simultaneous variation of all parameters, red for the variation of the clustering parameters only, and blue for the variation of $c^2_{\rm eff}$ and A_L. The anti-correlation of the sound speed with the inflationary parameters is partially removed when the lensing amplitude is allowed to vary.

4.3 Nucleosynthesis

To conclude this chapter I report the interesting correlation of neutrino properties with primordial abundances I worked on recently. The results of this analysis have been submitted to *Physical Review D*. The Big Bang Nucle-

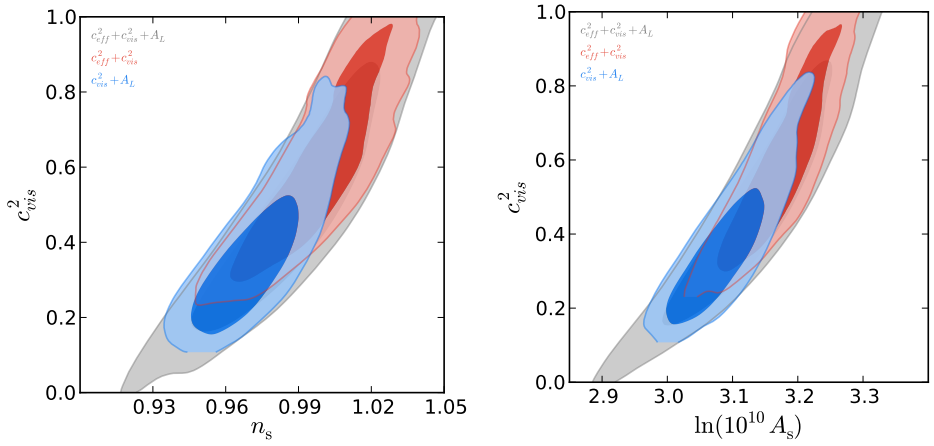

Figure 4.14: 2D contours for $c^2_{\rm vis}$ and the spectral parameters n_s (left) and A_s (right) in the Planck+WP case. Grey contours are for the simultaneous variation of all parameters, red for the variation of the clustering parameters only, and blue for the variation of $c^2_{\rm vis}$ and A_L. The correlation between viscosity and inflationary parameters is evident.

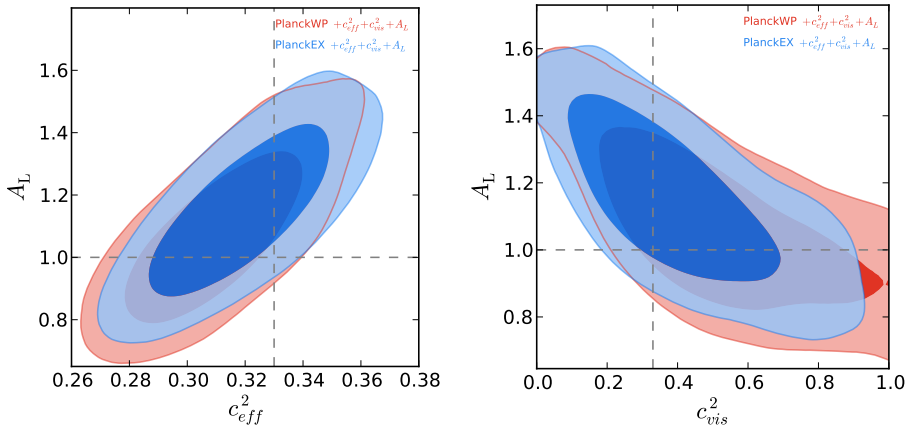

Figure 4.15: 2D contours for the lensing and the clustering parameters ($c^2_{\rm eff}$ on the left and $c^2_{\rm vis}$ on the right) in the case when all the three are free to vary. Different colors refer to different datasets, namely, grey for Planck+WP, red for Planck+BAO+HST and blue for Planck+lensing. The correlations of the clustering parameters with the lensing amplitude are opposite.

osynthesis (BBN) is the standard scenario of the formation of the light nu-

clei in the Big Bang scenario. The abundances of the light elements depend strongly on two factors: the baryon to photon ratio $\eta = n_b/n_\gamma \sim 10^{-9}$ and the number of relativistic species [79]. The baryon to photon ratio is fundamental for the following reasons. When the Universal temperature dropped below the binding energy E_b of light nuclei, in theory an abundance of this element should start to form. In practise, because of the very low baryon to photon ratio, encounters between baryons that creates nuclei are much less probable than encounters between baryons and photons from the high-energy tail of the spectrum (with $h\nu > E_b$) that disrupt them, and this makes the temperature T_a, at which nuclei start actually to form, lower than the binding energy by a factor $\eta^{(A-1)}$, where A is the atomic number of the species. The cosmological parameter Ω_b then is fundamental to determine precisely at which temperature the nucleosynthesis starts.

The number of neutrinos enters the calculation in that while neutrinos are coupled with the primordial plasma, they interact with e^+e^- pairs maintaining an equilibrium among the number of neutrons and protons given by their mass difference $X_n/X_p = exp(-\Delta m/T)$. When the temperature goes below $T_d \sim 1$ MeV ($\sim m_e$), however, there is no more enough energy to recreate e^+e^- pairs, and the neutron to proton ratio, starting from the last value $X_n/X_p(T_d)$ at equilibrium, begins to drop because of the neutron decay. The time spent between T_d and T_a is determinant for the number of neutrons available to form nuclei, and is directly linked to the ^4He abundance. The assumption of the BBN is indeed that all the neutrons end up in ^4He nuclei, and this ^4He formation leads to the depletion of other lighter elements like ^2H and ^3He. The heavier element to form in the nucleosynthesis process is the ^7Li, in extremely small amounts.

CMB observations, measuring the number of neutrinos and the baryon abundance, can tell us about primordial abundances of light nuclei. These quantities, however, can also be directly observed in areas of the sky particularly free from stellar formation and evolution. Stellar processes alter the element abundances with their nuclear reactions. In particular, ^2H is never produced in stellar reactions, but only consumed, and in this way ^2H observations can help to pose a lower limit on the baryon density. These observations are made on neutral Hydrogen clouds invested by the light emitted from far QSO (Lyman-α forests).

A numerical code `PArthENoPE` [80] is available to compute BBN results starting from parameters as Ω_b, N_{eff} and the neutron mean lifetime. I used it to derive fitting formulas to compute ^4He abundance, usually expressed as $Y_p = {}^4He/H$, and ^2H abundance $D = {}^2H/H$, and add these two parameters as derived ones to the chains obtained with the Planck+WP dataset. This analysis aimed to compare Planck predictions for ^2H with the value mea-

sured by Pettini and Cooke [81]. They analysed the light from a metal poor damped Lyman alpha system (DLA), namely the QSO SDSS J1419+0892, obtaining a highly accurate estimate of $D = 0.2535 \pm 0.0050 \cdot 10^{-4}$, that translates in a baryon density of $\Omega_b h^2 = 0.0223 \pm 0.0009$ for a standard number of neutrinos. The value for the baryonic abundance measured by Planck is $\Omega_b h^2 = 0.02205 \pm 0.00028$. There is a tension between these two measurements at a level of 1-2 standard deviations.

In this analysis I derived values for the D parameter in different extensions of the ΛCDM model and compute the deviance from the Pettini and Cooke measurement as shown in Tab.4.9. The different models allow for: a non standard lensing amplitude A_L, iso-curvature perturbations α_1, non standard mass or number of neutrinos $\sum m_\nu$ and N_{eff}, tilt of the spectral index n_r, spatial curvature Ω_k, non standard EOS for dark energy w, non-null tensor to scalar ratio of the perturbations r and combinations of them. We could drop the following conclusions for the one-parameter extensions:

- in models where w, r, n_r, α_1 are free to vary there is no variation (or at least a very small variation) in values of Deuterium with respect to the standard model. We can infer that there is no correlation between these parameters and the abundances of light nuclei;
- in models with A_L, Ω_k as free parameters we saw a strong variation with respect to the standard model and I obtained values of Deuterium in good agreement, even within $1\,\sigma$, with the value of Pettini and Cooke;
- in the two models in which $\sum m_\nu$ and N_{eff} are free to vary the new Deuterium distributions are even farther from the one obtained by Pettini and Cooke with respect to the standard model.

I then retained those combinations for which the two values were more in agreement and used the importance sampling technique to weight the chains imposing a Gaussian prior on D based on the Pettini and Cooke value. In this way are including this data-point in the analysis. The numerical results are reported from Tab.4.10 to Tab.4.14.

When Pettini and Cooke prior is added to the extensions considered we have several shifts in the extra parameters: A_L and Ω_k tend to stay away from the standard value, see Fig.4.16. When in combination with $\sum m_\nu$, A_L again shows the same behaviour, as shown in Fig.4.17. Finally, for what concerns the inflationary parameters n_r and r, the former remains close to its standard value, while the latter shows a non-null value, as reported in Fig.4.18. When these parameters are combined also with curvature Ω_k, the agreement with Pettini and Cooke result is perfect, due to an enhanced curvature balanced by a higher tensor to scalar ratio, see Fig.4.19.

Model	$\Omega_b h^2$	$(D/H)\cdot 10^{-5}$	$\frac{\Delta}{\sigma_{CMB}}\cdot 10^{-2}$
ΛCDM	0.02207 ± 0.00027	2.661 ± 0.055	2.3
$+A_L$	0.02244 ± 0.00036	2.585 ± 0.067	0.75
$+\alpha_1$	0.02216 ± 0.00029	2.638 ± 0.057	1.8
$+\sum m_\nu$	0.02190 ± 0.00032	2.692 ± 0.065	2.4
$+N_{eff}$	0.02238 ± 0.00041	2.753 ± 0.094	2.3
$+n_r$	0.02218 ± 0.00029	2.636 ± 0.057	1.8
$+\Omega_k$	0.02231 ± 0.00030	2.611 ± 0.059	1.3
$+w$	0.02206 ± 0.00028	2.658 ± 0.055	2.2
$+r$	$0.02207^{+0.00028}_{-0.00027}$	2.656 ± 0.055	2.2
$+\sum m_\nu$, A_L	0.02228 ± 0.00038	2.617 ± 0.074	1.1
$+\sum m_\nu$, Ω_k	0.02211 ± 0.00035	2.650 ± 0.068	1.7
$+\sum m_\nu$, N_{eff}	0.02220 ± 0.00045	2.763 ± 0.092	2.5
$+n_r$, r	0.02232 ± 0.00032	2.611 ± 0.061	1.3
$+n_r$, r, Ω_k	0.02276 ± 0.00044	2.528 ± 0.079	0.089

Table 4.9: Values of $\Omega_b h^2$ and ^2H abundance for the ΛCDM model and for all the extensions considered. In the last column is reported the squared difference with the Pettini and Cooke value divided by the uncertainty on the CMB estimation.

Parameters	PLANCK+WP	PLANCK+WP+D
A_L	$1.22^{+0.12}_{-0.12}$	1.25 ± 0.11
$\Omega_b h^2$	$(0.2244 \pm 0.0036)\cdot 10^{-1}$	$(0.2262 \pm 0,0022)\cdot 10^{-1}$
$\Omega_c h^2$	0.1168 ± 0.0030	0.1158 ± 0.0025
n_s	0.9689 ± 0.0084	0.9718 ± 0.0070
$100\,\theta$	1.04181 ± 0.00068	1.04201 ± 0.00061
τ	$0.867^{+0.058}_{-0.062}\cdot 10^{-1}$	$0.877^{+0.056}_{-0.063}\cdot 10^{-1}$
$\log(10^{10}A_s)$	3.077 ± 0.025	3.077 ± 0.025

Table 4.10: Parameters mean values and 68% c.l. for the case ΛCDM+A_L. Left column shows results of the CMB-only analysis, while in the right panel are reported the values obtained after imposing the D prior.

Parameters	PLANCK+WP	PLANCK+WP+D
Ω_k	$-0.37^{+0.23}_{-0.22}\cdot 10^{-1}$	$-0.44 \pm 0.23\cdot 10^{-1}$
$\Omega_b h^2$	$(0.2231 \pm 0.0031)\cdot 10^{-1}$	$0.2254^{+0.0020}_{-0.0021}\cdot 10^{-1}$
$\Omega_c h^2$	$0.1183^{+0.0027}_{-0.0029}$	0.1171 ± 0.0024
n_s	$0.9646^{+0.0075}_{-0.0074}$	$0.9680^{+0.0066}_{-0.0067}$
$100\,\theta$	$1.04159^{+0.00065}_{-0.00064}$	1.0418 ± 0.0060
τ	$0.869^{+0.058}_{-0.064}\cdot 10^{-1}$	$0.892^{+0.059}_{-0.064}\cdot 10^{-1}$
$\log(10^{10}A_s)$	3.081 ± 0.025	3.083 ± 0.025

Table 4.11: Parameters mean values and 68% c.l. for the case ΛCDM+Ω_k. Left column shows results of the CMB-only analysis, while in the right panel are reported the values obtained after imposing the D prior.

Parameters	PLANCK+WP	PLANCK+WP+D
$\sum m_\nu$[eV]	< 0.71	< 0.56
A_L	1.30 ± 0.13	1.34 ± 0.13
$\Omega_b h^2$	$(0.2228 \pm 0.0038) \cdot 10^{-1}$	$(0.2257 \pm 0.0022) \cdot 10^{-1}$
$\Omega_c h^2$	$0.1177^{+0.0030}_{-0.0031}$	$0.1160^{+0.0025}_{-0.0024}$
n_s	0.9644 ± 0.0095	$0.9699^{+0.0073}_{-0.0074}$
$100\,\theta$	$1.04144^{+0.00072}_{-0.00071}$	1.04178 ± 0.00062
τ	$0.865^{+0.058}_{-0.065} \cdot 10^{-1}$	$0.881^{+0.059}_{-0.066} \cdot 10^{-1}$
$\log(10^{10} A_s)$	3.077 ± 0.025	3.077 ± 0.026

Table 4.12: Parameters mean values and 68% c.l. for the case ΛCDM+$\sum m_\nu$+A_L. Left column shows results of the CMB-only analysis, while in the right panel are reported the values obtained after imposing the D prior.

Parameters	PLANCK+WP	PLANCK+WP+D
n_r	$(-0.21 \pm 0.11) \cdot 10^{-1}$	$(-0.24 \pm 0.11) \cdot 10^{-1}$
r	< 0.126	< 0.150
$\Omega_b h^2$	$(0.2232 \pm 0.0032) \cdot 10^{-1}$	$(0.2255 \pm 0.0021) \cdot 10^{-1}$
$\Omega_c h^2$	0.1198 ± 0.0028	$0.1188^{+0.0025}_{-0.0024}$
n_s	0.9583 ± 0.0080	0.9610 ± 0.0075
$100\,\theta$	$1.04140^{+0.00062}_{-0.00063}$	1.04161 ± 0.00058
τ	$0.1002^{+0.0066}_{-0.0080}$	$0.1050^{+0.0066}_{-0.0078}$
$\log(10^{10} A_s)$	3.115 ± 0.031	3.123 ± 0.031

Table 4.13: Parameters mean values and 68% c.l. for the case ΛCDM+n_r+r. Left column shows results of the CMB-only analysis, while in the right panel are reported the values obtained after imposing the D prior.

Parameters	PLANCK+WP	PLANCK+WP+D
n_r	$(-0.22 \pm 0.13) \cdot 10^{-1}$	$(-0.213 \pm 0.12) \cdot 10^{-1}$
r	< 0.253	< 0.234
Ω_k	$-0.57^{+0.34}_{-0.33} \cdot 10^{-1}$	$(-0.52 \pm 0.29) \cdot 10^{-1}$
$\Omega_b h^2$	$(0.2276 \pm 0.0044) \cdot 10^{-1}$	$0.2272^{+0.0023}_{-0.0024} \cdot 10^{-1}$
$\Omega_c h^2$	0.1164 ± 0.0034	0.1166 ± 0.0027
n_s	0.970 ± 0.010	$0.9687^{+0.0085}_{-0.0083}$
$100\,\theta$	$1.04196^{+0.00072}_{-0.00073}$	1.04191 ± 0.00062
τ	$0.950^{+0.066}_{-0.074} \cdot 10^{-1}$	$0.949^{+0.064}_{-0.071} \cdot 10^{-1}$
$\log(10^{10} A_s)$	3.097 ± -0.030	3.098 ± 0.030

Table 4.14: Parameters mean values and 68% c.l. for the case ΛCDM+n_r+r+Ω_k. Left column shows results of the CMB-only analysis, while in the right panel are reported the values obtained after imposing the D prior.

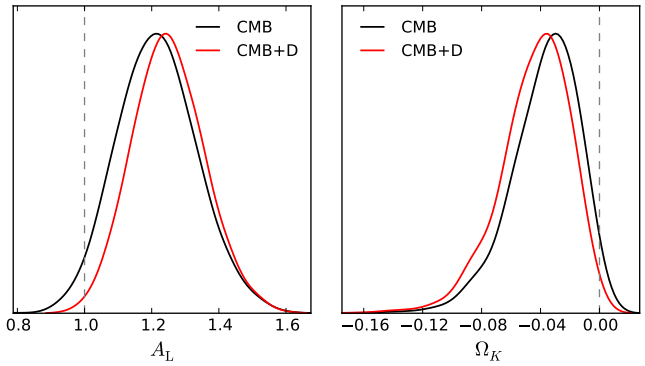

Figure 4.16: I report here the posteriors for ΛCDM+A_L (left) and ΛCDM+Ω_k (right) where the black line refers to the CMB-only case, while the red to the case with the add of the D prior. In both cases including the Deuterium prior pushes the results a little farther from the standard expectations.

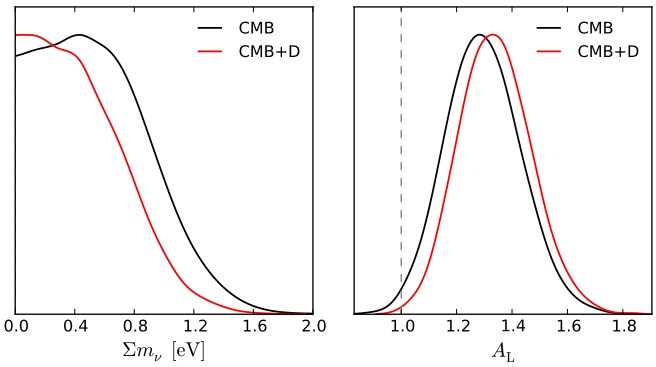

Figure 4.17: I report here the posteriors for ΛCDM+$\sum m_\nu$+A_L, where the black lines refer to the CMB-only case, while the red to the case with the D prior. With the inclusion of the Deuterium prior the sum of the masses of neutrinos is more consistent with zero while the lensing amplitude shows an even higher value.

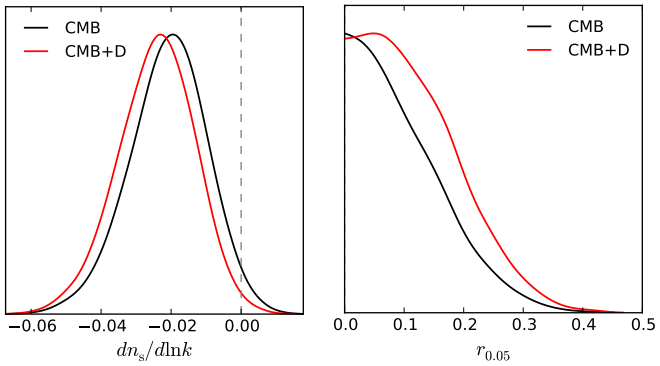

Figure 4.18: I report here the posteriors for ΛCDM+n_r+r, where the black lines refer to the CMB-only case, while the red to the case with the D prior. The inflationary parameters are slightly effected by the inclusion of the Deuterium prior, moving toward non-standard values.

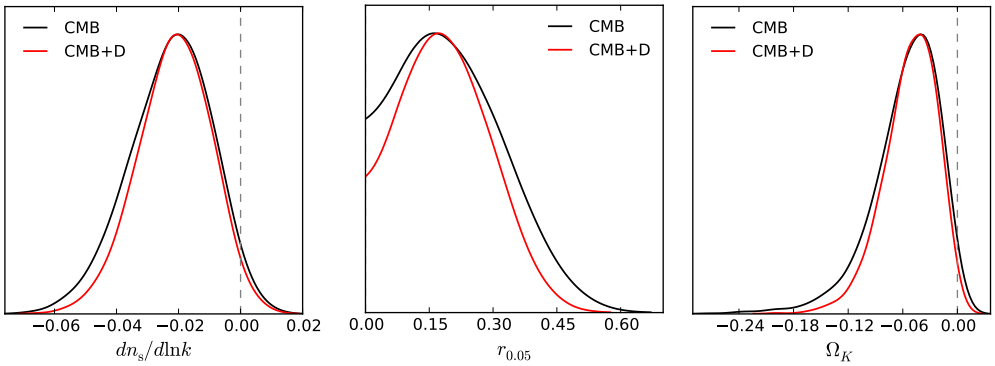

Figure 4.19: I report here the posteriors for ΛCDM+n_r+r+Ω_k, where the black lines refer to the CMB-only case, while the red to the case with the D prior. Adding D has a small effect on these posteriors, given the fact that this combination recovers well the Pettini and Cooke D value using only CMB data.

My reference papers

10.1103/PhysRevD.88.023501 E. Di Valentino, S. Galli, M. Lattanzi, A. Melchiorri, P. Natoli, L. Pagano and N. Said, "*Tickling the CMB damping tail: scrutinizing the tension between the ACT and SPT experiments*", Phys. Rev. D **88**, 023501 (2013) arXiv:1301.7343 [astro-ph.CO]].

10.1103/PhysRevD.88.023513 N. Said, E. Di Valentino and M. Gerbino, "*Planck constraints on the effective neutrino number and the CMB power spectrum lensing amplitude*", Phys. Rev. D **88**, 023513 (2013) [arXiv:1304.6217 [astro-ph.CO]].

10.1103/PhysRevD.88.063538 M. Gerbino, E. Di Valentino and N. Said, "*Neutrino Anisotropies after Planck*", Phys. Rev. D **88**, 063538 (2013) [arXiv:1304.7400 [astro-ph.CO]].

Waiting for publication in Physiscal Review D L. Salvati, N. Said, A. Melchiorri
'*Is PLANCK consistent with primordial Deuterium measurements?*'

Chapter 5

Dark energy

'...I thought maybe
I thought this would go away
But it continues
The only constant
Every day
Stronger...'

Nine Inch Nails - Demon Seed

In this chapter I will discuss my work on dark energy evolution. If the dark energy is a cosmological constant, indeed, the value of its EOS should be always equal to -1. A strong way, then, to determine the viability of a cosmological constant solution is to study the time evolution of this EOS, looking for possible deviations from the actual value $w \sim -1$. Each other theory developed to explain the accelerated expansion of the Universe (scalar field theories and modified gravity scenarios) can indeed be represented by an effective energy density that evolves in time following an effective EOS [82]. The only requisite for this EOS is to be $< -1/3$, in order to allow for an acceleration of the space-time expansion (refer to 1.8).

5.1 Time evolution

In general dark energy is expressed by an energy density ρ_x and its EOS w_x, and its evolution can be studied using perturbation equations 2.15. As we yet mentioned, this approach is valid only in the limit $w_x > -1$, because for values of the EOS equal or below -1 (phantom models) the synchronous gauge presents coordinate divergences due to infinite sound speed. In this case one must follow the approach of Hu and work in the PPF framework, in which density and momentum are treated as a unique perturbed variable,

whose sound speed is finite and well-behaved. In order to use this framework to evolve the perturbations I modified `camb` and `CosmoMC`. I sampled on the baryon and cold dark matter densities Ω_b and Ω_c, the Hubble constant H_0, the re-ionization optical depth τ, the scalar spectral index n_s, and the overall normalization of the spectrum A_s.

Instead of the single value w_x for the dark energy EOS, I introduced 6 parameters $w_i(z)\,(i = 1, 2, ..6)$, each representing the value of w_x in a particular red-shift bin $z_i \in [0.0, 0.25, 0.50, 0.85, 1.25, 2.0]$ equally spaced in $\ln(a)$. Including more than six bins does not significantly improve the constraints. The $\ln(a)$ spacing makes possible to have a statistical significant number of low-red-shift observables in each bin. In order to have $w_x(z)$ as a smooth and continuous function, I interpolated between these values with a hyperbolic tangent function defined as:

$$\begin{cases} w_x(z) = w_i & z = z_i \\ w_x(z) = w_i + \delta_w + \delta_w \tanh(\frac{\delta_z - z}{s}) & z \in [z_i, z_{i+1}] \\ w_x(z) = -1 & z \geq z_6 \end{cases}$$

where A_i is an amplitude factor, δ_z is the half value of $(z_{i+1} - z_i)$, δ_w is the half value of $(w_{i+1} - w_i)$ and s is a smoothing parameter. The position of the bins was chosen in order to be sensitive to the presence of SN and BAO, that can constrain effectively the value of $w_x(z)$, rather than the CMB, that can give only very wide constraints on it (the only part of the CMB spectrum that is highly sensitive to the presence of dark energy is the low-ℓ part, affected by the ISW effect, that however is strongly limited in accuracy, due to cosmic variance 1.33). The datasets I used in this work are reported below.

I used the CMB observations coming from WMAP 7 years. As non-CMB data, for the SN I separately used the Union1 compilation, Union2 and SNLS. I considered then different datasets for BAO combined in the following way:

- run1
  SDSS-dr7 at z=0.20, 0.35 in form of $d_s(z)$, WiggleZ at z=0.44, 0.60, 0.73 in form of $A_s(z)$;

- run2
  6dFGRS at z=0.1, WiggleZ at z=0.44, 0.60, 0.73 all in form $d_s(z)$;

- run3
  WiggleZ at z=0.44, 0.60, 0.73 all in form $d_s(z)$;

- run4
  6dFGRS at z=0.1, SDSS-dr7 at z=0.20, 0.35, WiggleZ at z=0.44, 0.60, 0.73 all in form $d_s(z)$.

I chose a preferred combination of BAO and SN and I added the measurements for H_0 from the Hubble Space Telescope and the $H(z)$ dataset from Moresco et al..

As noticed in last section of Chapter 3, the estimations that we can determine for the $w_i(z)$ will be correlated. I used the PCA procedure of Serra and Cooray introduced in Section 3.5 to decorrelate them. In other words I used `CosmoMC` with the $w_i(z)$ to obtain their mean values and covariance matrix. After that, using PCA, I derived $q_i(z)$, the decorrelated values, and then run again the statistics to evaluate their marginalized values and errors. In left panel of Fig.5.1 I show typical weights to obtain $\mathbf{q}$ from a linear combination of $\mathbf{w}$ while in right panel I show the likelihoods of the six principal components q_i for a typical run. It can be noticed how, as expected, the lower red-shift components are better constrained than the higher red-shift ones.

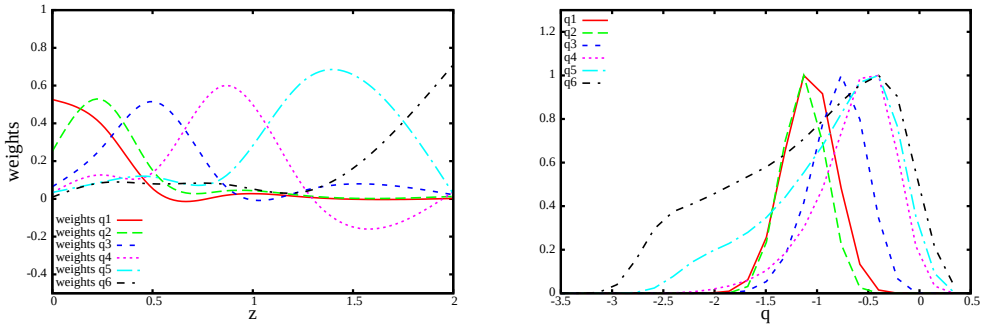

Figure 5.1: On the left typical weights used to obtain the principal components $q_i(z)$ starting from the values of the $w_i(z)$. The weights plotted are those obtained by PCA decorrelation for run2 of Tab.5.3. Notice the localisation of these weight functions. On the right typical likelihoods for the principal components $q_i(z)$. Clearly the low-red-shift ones are much better constrained than the high-red-shift ones.

The results obtained by combining CMB+SN are reported in Tab.5.1 and in left panel of Fig.5.2. There is a general agreement with a cosmological constant, for all the $q_i(z)$ and all the datasets. However, if we look at the value of q_3, around $z \sim 0.5$, the SNLS survey results appears closer to the ΛCDM behaviour than the Union1 and Union2 ones that indeed show slightly larger values of q_3. The constraints on H_0 (refer to Tab.5.1), then, are slightly different from dataset to dataset: the SNLS survey indicates larger values,

Parameters	**WMAP7** +Union1	**WMAP7** +Union2	**WMAP7** +SNLS
$\Omega_b h^2$	0.0222 ± 0.0011	0.0222 ± 0.0011	0.0222 ± 0.0011
$\Omega_c h^2$	0.113 ± 0.011	0.113 ± 0.011	0.113 ± 0.010
H_0[km/s/Mpc]	68.2 ± 6.1	70.4 ± 6.1	72.6 ± 7.0
n_s	0.963 ± 0.028	0.963 ± 0.026	0.962 ± 0.027
$\log(10^{10} A_s)$	3.209 ± 0.091	3.212 ± 0.085	3.213 ± 0.084
$q_6(z = 2.00)$	> -3.0	$-1.6^{+1.4}_{-1.2}$	-1.5 ± 1.3
$q_5(z = 1.25)$	$-1.3^{+1.1}_{-1.2}$	-1.3 ± 1.0	$-1.4^{+1.0}_{-1.1}$
$q_4(z = 0.85)$	$-0.92^{+0.58}_{-0.97}$	$-1.11^{+0.57}_{-0.71}$	$-1.31^{+0.80}_{-0.87}$
$q_3(z = 0.50)$	$-0.84^{+0.30}_{-0.38}$	$-0.89^{+0.31}_{-0.34}$	$-1.06^{+0.31}_{-0.37}$
$q_2(z = 0.25)$	$-1.02^{+0.22}_{-0.23}$	$-1.08^{+0.16}_{-0.19}$	$-1.02^{+0.14}_{-0.15}$
$q_1(z = 0.00)$	$-0.93^{+0.39}_{-0.38}$	$-1.02^{+0.29}_{-0.28}$	-1.03 ± 0.21
θ	1.0380 ± 0.0054	1.0380 ± 0.0052	1.0382 ± 0.0052
Ω_Λ	0.708 ± 0.061	0.725 ± 0.059	0.742 ± 0.057
Ω_m	0.292 ± 0.061	0.275 ± 0.059	0.258 ± 0.057
Age/Gyr	13.84 ± 0.32	13.79 ± 0.31	13.72 ± 0.32
χ^2	7776.58	7999.48	7586.84

Table 5.1: Constraints at 95% confidence level for a WMAP 7 years analysis considering different SN datasets. The SNLS survey provides constraints that are more consistent with the ΛCDM case.

with $H_0 \sim 72.5$ km/s/Mpc, while the Union2 and Union1 catalogues prefer smaller values with $H_0 \sim 70.4$ km/s/Mpc and $H_0 \sim 68.2$ km/s/Mpc respectively. All these values of H_0 are however in mutual agreement in between two standard deviations.

When combining on the contrary CMB+BAO datasets the evidence goes towards $q_i > -1$, even remaining in agreement with the cosmological constant scenario. Particular attention must be paid to the H_0 values. These indeed are in the range $58 - 64$ km/s/Mpc, in strong tension with the HST result of $H_0 = 73.8 \pm 2.4$ km/s/Mpc. All the results for this case are reported in Tab.5.2 and represented in right panel of Fig.5.2.

I then added together info from SNLS (the dataset that appears to lower the error bars at low red-shift and to give less scattered results) for SN and the different BAO combinations examined to choose a preferred dataset to which add further measurements. Results are shown in left panel of Fig.5.3. In this case we found a slight indication for $w < -1$ around the second bin q_2 at $z \sim 0.25$. This deviation was already noticed in [83]. The values of q_3 at $z \sim 0.50$ are on the contrary larger than -1 at about one standard deviation. The agreement with a cosmological constant is worse with respect to the WMAP+SNLS case. It seems as the BAO data are hiking up the value of the q_i everywhere but in the second bin, where the weight of the SN

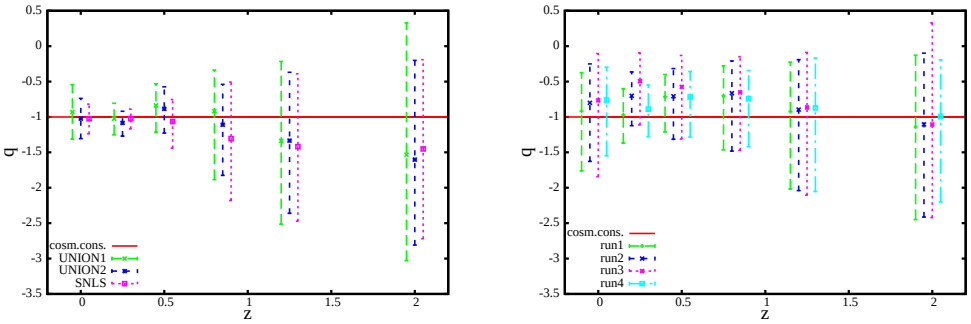

Figure 5.2: On the left are reported constraints at 95% c.l. on $q_i(z)$ from WMAP 7 years data combined with different SN catalogues: Union1, Union2 and SNLS. As we can see all the datasets provide constraints on $q_i(z)$ that are consistent with the predictions of a cosmological constant in between two standard deviations. On the right are plotted the constraints on the dark energy EOS from a combined analysis with different BAO datasets as described in the text. There is a broad agreement with a cosmological constant for all the datasets and none of them reduces significantly the error bars with respect to the others.

is much higher and dominates the results. Looking at numerical results in Tab.5.3 one can see that adding BAO data lowers significantly the preferred value for the Hubble constant with respect to the WMAP+SNLS case, as expected from the results of the WMAP+BAO analysis.

I chose as default combination the CMB+SNLS+BAO-run2, given its tight constraints and less scattered results with respect to the other datasets combinations. To this combination I added singularly and together the HST prior on H_0 (even if in strong tension with BAO predictions) and the $H(z)$ dataset of Moresco et al.. Both the HST prior and the $H(z)$ dataset render the value of q_3 more compatible with predictions of a cosmological constant ($w = -1$). In general, with the exception of the value of q_2 at $z \sim 0.25$, that prefers $w < -1$, there is a general agreement with a cosmological constant. $q_i(z)$ results are showed in right panel of Fig.5.3, while the numerical mean values for the cosmological parameters are reported in Tab.5.4.

These results can be used to make a qualitative comparison with some models of dark energy. I chose to make this comparison with some modified gravity proposed models. As final dataset I used the WMAP+SNLS+BAO+ $H(z)$, not including HST prior because of its strong tension with BAO predictions.

Parameters	**WMAP7** BAO-run1	**WMAP7** BAO-run2	**WMAP7** BAO-run3	**WMAP7** BAO-run4
$\Omega_b h^2$	0.0221 ± 0.0011	0.0222 ± 0.0012	0.0223 ± 0.0012	0.0221 ± 0.0012
$\Omega_c h^2$	0.118 ± 0.011	0.115 ± 0.012	0.115 ± 0.012	0.116 ± 0.012
H_0[km/s/Mpc]	63.7 ± 6.9	60.4 ± 6.4	57.95 ± 8.3	61.9 ± 5.7
n_s	0.959 ± 0.029	0.963 ± 0.030	0.965 ± 0.030	0.961 ± 0.031
$\log(10^{10} A_s)$	3.238 ± 0.099	3.212 ± 0.093	3.23 ± 0.10	3.22 ± 0.10
$q_6(z = 2.00)$	$-1.1^{+1.0}_{-1.3}$	$-1.1^{+1.0}_{-1.3}$	> -2.4	$-0.99^{+0.80}_{-1.21}$
$q_5(z = 1.25)$	$-0.92^{+0.70}_{-1.10}$	$-0.90^{+0.71}_{-1.14}$	$-0.9^{+1.0}_{-1.2}$	$-0.87^{+0.71}_{-1.18}$
$q_4(z = 0.85)$	$-0.70^{+0.43}_{-0.76}$	$-0.66^{+0.46}_{-0.82}$	$-0.65^{+0.50}_{-0.82}$	$-0.74^{+0.40}_{-0.68}$
$q_3(z = 0.50)$	$-0.72^{+0.32}_{-0.50}$	$-0.71^{+0.39}_{-0.61}$	$-0.57^{+0.44}_{-0.64}$	$-0.72^{+0.36}_{-0.57}$
$q_2(z = 0.25)$	$-0.97^{+0.37}_{-0.40}$	$-0.70^{+0.34}_{-0.42}$	$-0.50^{+0.40}_{-0.62}$	$-0.89^{+0.34}_{-0.39}$
$q_1(z = 0.00)$	$-0.92^{+0.54}_{-0.85}$	$-0.80^{+0.55}_{-0.83}$	$-0.77^{+0.66}_{-1.08}$	$-0.76^{+0.46}_{-0.79}$
$100\,\theta$	1.0375 ± 0.0054	1.0377 ± 0.0055	1.0380 ± 0.0055	1.0373 ± 0.0056
Ω_Λ	0.652 ± 0.072	0.587 ± 0.075	0.67 ± 0.11	0.639 ± 0.060
$\Omega_{\rm m}$	0.348 ± 0.072	0.380 ± 0.075	0.41 ± 0.11	0.361 ± 0.060
Age/Gyr	14.03 ± 0.29	14.04 ± 0.30	14.07 ± 0.30	14.05 ± 0.33
χ^2	7476.05	7474.62	7473.73	7478.43

Table 5.2: Constraints at 95% confidence level for a WMAP 7 years analysis considering different combinations of BAO datasets (see text). BAO data clearly prefer a lower Hubble constant around $H_0 \sim 61$ km/s/Mpc.

Parameters	**WMAP7+SNLS** BAO-run1	**WMAP7+SNLS** BAO-run2	**WMAP7+SNLS** BAO-run3	**WMAP7+SNLS** BAO-run4
$\Omega_b h^2$	0.0220 ± 0.0011	0.0221 ± 0.0011	0.0221 ± 0.0011	0.0222 ± 0.0012
$\Omega_c h^2$	0.119 ± 0.012	0.118 ± 0.011	0.117 ± 0.012	0.117 ± 0.012
H_0[km/s/Mpc]	64.3 ± 3.5	64.6 ± 3.8	64.4 ± 4.2	63.6 ± 3.0
n_s	0.957 ± 0.029	0.959 ± 0.030	0.960 ± 0.029	0.962 ± 0.031
$\log(10^{10} A_s)$	3.245 ± 0.098	3.236 ± 0.093	3.229 ± 0.095	3.22 ± 0.10
$q_6(z = 2.00)$	> -2.7	$-1.1^{+1.0}_{-1.5}$	$-0.97^{+0.92}_{-1.43}$	$-0.79^{+0.71}_{-1.22}$
$q_5(z = 1.25)$	$-0.75^{+0.69}_{-1.45}$	$-0.71^{+0.60}_{-1.23}$	$-0.67^{+0.65}_{-1.28}$	$-0.59^{+0.47}_{-0.92}$
$q_4(z = 0.85)$	$-0.52^{+0.40}_{-0.71}$	$-0.56^{+0.37}_{-0.72}$	$-0.47^{+0.34}_{-0.62}$	$-0.45^{+0.31}_{-0.51}$
$q_3(z = 0.50)$	$-0.84^{+0.28}_{-0.41}$	$-0.82^{+0.27}_{-0.45}$	$-0.85^{+0.28}_{-0.40}$	$-0.73^{+0.26}_{-0.37}$
$q_2(z = 0.25)$	$-1.21^{+0.18}_{-0.19}$	$-1.14^{+0.18}_{-0.19}$	$-1.14^{+0.18}_{-0.19}$	$-1.17^{+0.18}_{-0.20}$
$q_1(z = 0.00)$	$-1.06^{+0.27}_{-0.30}$	$-1.11^{+0.27}_{-0.31}$	$-1.08^{-0.25}_{+0.29}$	$-1.06^{+0.27}_{-0.32}$
$100\,\theta$	1.0370 ± 0.0052	1.0372 ± 0.0054	1.0373 ± 0.0054	1.0374 ± 0.0055
Ω_Λ	0.659 ± 0.035	0.657 ± 0.042	0.665 ± 0.048	0.656 ± 0.035
$\Omega_{\rm m}$	0.341 ± 0.035	0.343 ± 0.042	0.335 ± 0.048	0.344 ± 0.035
Age/Gyr	14.1 ± 0.28	14.10 ± 0.28	14.08 ± 0.30	14.11 ± 0.28
χ^2	7595.08	7594.50	7593.98	7597.02

Table 5.3: Constraints at 95% confidence level for a WMAP+SNLS analysis considering different combinations of BAO datasets (see text). I can see the hint for a lower value of $q_i < -1$ in the red-shift bin around $z = 0.25$, where SN has the most of their high precision measurements, while there is a preference for $w > -1$ in higher red-shift bins where BAO dominate.

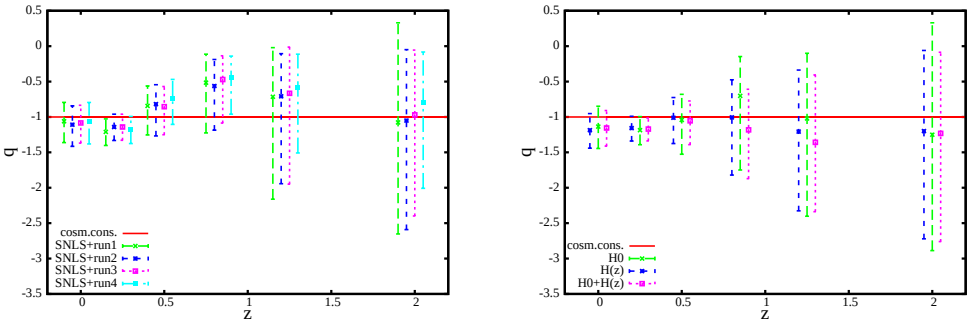

Figure 5.3: On the left: constraints on the dark energy EOS from a combined analysis of the WMAP+SNLS dataset with different BAO datasets as described in the text. There is general agreement with a cosmological constant, however values at red-shift $z \sim 0.25$ are in better agreement with $w < -1$ while values at $z \sim 0.5$ prefer a $w > -1$. On the right: constraints on the dark energy EOS from a combined analysis of the WMAP+SNLS+BAO-run2 dataset with the HST prior on the Hubble constant and the determination of $H(z)$ in Moresco et al.. There is an improved agreement with a cosmological constant with respect to the WMAP+SNLS+BAO case for q_3 at $z \sim 0.50$.

In Fig.5.4 I show how the results on q_i are in tension with the typical $w(z)$ behaviour of models such as the Hu-Sawicki $f(R)$ model (HS) [84], the covariant Galileon model [85] and two different tracking models [86, 87]. For both tracking and HS models this is given by the fact that all of these predict $w(z) > -1$ at low red-shifts that clearly disagrees with the hint for a lower value than -1 as found in this analysis. The covariant galileon model instead does give $w < -1$, however it is in tension with values in the higher red-shift bins.
It is important to stress that this kind of models do not affect only the background expansion of the Universe, but they also produce effects on structure growth and therefore on CMB, and this leads to degrade constraints on q_i, in particular at high red-shifts where the LSS clustering is important [88]. The error bars obtained with this analysis can be considered appropriate for quantitative comparison with models that change the Universal evolution only at a background level, through the different $w(z)$ function.

Parameters	**WMAP7+SNLS+BAO** +HST	**WMAP7+SNLS+BAO** +H(z)	**WMAP7+SNLS+BAO** +H(z)+HST
$\Omega_b h^2$	0.0222 ± 0.0011	0.0219 ± 0.0011	0.0221 ± 0.0011
$\Omega_c h^2$	0.121 ± 0.012	0.1248 ± 0.0096	0.1250 ± 0.0093
H_0[km/s/Mpc]	67.2 ± 3.4	66.4 ± 3.0	68.1 ± 2.7
n_s	0.959 ± 0.029	0.950 ± 0.027	0.953 ± 0.026
$\log(10^{10} A_s)$	3.248 ± 0.097	3.284 ± 0.081	3.277 ± 0.077
$q_6(z = 2.00)$	> -2.9	$-1.2^{+1.1}_{-1.5}$	$-1.2^{+1.1}_{-1.5}$
$q_5(z = 1.25)$	$-1.02^{+0.92}_{-1.38}$	$-1.21^{+0.87}_{-1.12}$	$-1.36^{+0.95}_{-0.98}$
$q_4(z = 0.85)$	$-0.70^{+0.56}_{-1.05}$	$-1.01^{+0.53}_{-0.82}$	$-1.18^{+0.57}_{-0.69}$
$q_3(z = 0.50)$	$-1.04^{+0.36}_{-0.48}$	$-1.01^{+0.29}_{-0.36}$	$-1.05^{+0.28}_{-0.34}$
$q_2(z = 0.25)$	$-1.19^{+0.19}_{-0.21}$	$-1.16^{+0.17}_{-0.18}$	-1.18 ± 0.17
$q_1(z = 0.00)$	$-1.14^{+0.29}_{-0.31}$	$-1.12^{+0.23}_{-0.25}$	$-1.16^{+0.25}_{-0.26}$
$100\,\theta$	1.0380 ± 0.0052	1.0368 ± 0.0054	1.0376 ± 0.0052
Ω_Λ	0.683 ± 0.036	0.667 ± 0.037	0.682 ± 0.033
Ω_m	0.317 ± 0.036	0.333 ± 0.037	0.318 ± 0.033
Age/Gyr	13.92 ± 0.24	13.96 ± 0.24	13.86 ± 0.22
χ^2	7608.70	7611.00	7619.64

Table 5.4: Constraints at 95% confidence level for a WMAP+SNLS+BAO-run2 analysis considering the HST prior on the Hubble constant and the determination of $H(z)$ from Moresco et al..

5.2 CMB shift parameters

Following [89] one can derive from CMB data simple distance indicators, that can be used to add CMB constraints to the low-z distance measurements. In this way results on $w(z)$ can be used in a safe way to constrain the parameters of the different modified gravity models, in that the perturbation evolution remains out of the analysis. An optimal set of distance measurements, known as *shift parameters*, are R and ℓ_a, that combined with $\Omega_b h^2$ and n_s can furnish this alternative way to include CMB information in the analysis. These shift parameters are defined as follows:

$$R = \frac{\sqrt{\Omega_m H_0^2} d_d}{c} \tag{5.1}$$

$$\ell_a = \frac{\pi d_d}{r_s} \tag{5.2}$$

where d_d is the co-moving distance to the decoupling surface and r_s is the co-moving sound horizon at decoupling epoch. Using Planck release I computed these values for a combination of Planck+WP and the Planck lensing likelihood obtaining the values reported in Tab.5.5 for the set R,ℓ_a, $\Omega_b h^2$ and n_s.

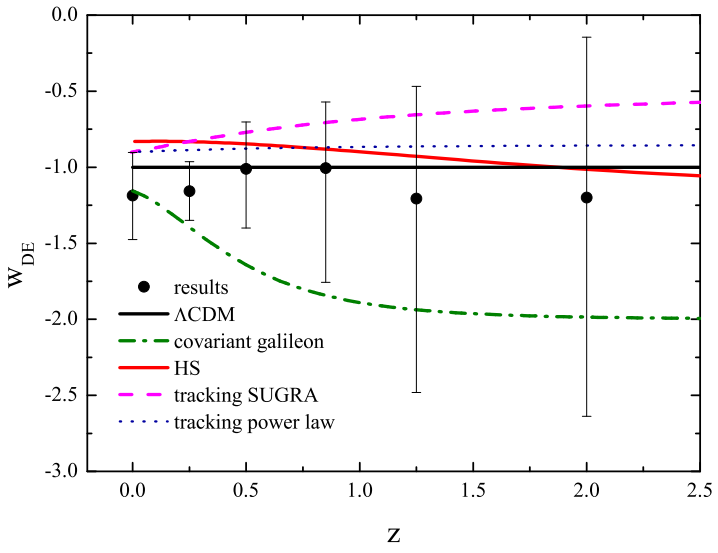

Figure 5.4: Comparison of the constraints on the dark energy EOS derived from a WMAP+SNLS+BAO+$H(z)$ dataset with several dark energy models as covariant Galileon, Hu-Sawicki, tracking SUGRA and tracking power-law. Most of these models are in tension with the data mostly because of the low red-shift values of q_1 and q_2 that point to a cosmological constant or to $w(z \sim 0.25) < -1$. The tracking power law model reproduces the low red-shift behaviour but is in disagreement with the constraints at higher red-shifts.

With these values one can make a full analysis including CMB, SN, BAO and $H(z)$ measurements to derive estimations for the uncorrelated values $q(z)$ that do not include perturbation information and so can be easily used to be compared with different dark energy models predictions. The MCMC sampled on 10 parameters: the 6 values w_i, $\Omega_b h^2$, $\Omega_c h^2$, H_0 and n_s. Beside Planck+WP+lensing I added as SN the Union2.1 compilation, and BAO data-points the ones from 6dFGRS, SDSS-DR7, SDSS-DR9 and WiggleZ. As usual $H(z)$ measurements are from HST for $z = 0$ and Moresco et al. for $z \neq 0$. Results are shown in Fig.5.5 and reported in Tab.5.6.

From the results shown we can see that with Planck CMB spectrum and lensing information and the new SN compilation Union2.1 the constraints on $w(z)$ are broadly consistent with a ΛCDM model, nevertheless at small red-shift, in particular at $z = 0.25$ there is still a hint for a smaller value than $w =$

Parameters	Planck+WP+lensing
$\Omega_b h^2$	0.02228 ± 0.00021
R	1.7407 ± 0.0047
ℓ_a	301.57 ± 0.15
n_s	0.9662 ± 0.0042

Table 5.5: Constraints at 68 % confidence level for a Planck+WP+lensing analysis to compute shift parameters R and ℓ_a for the CMB.

Parameters	**Planck+WP+lensing** +SN	**Planck+WP+lensing** +SN+BAO	**Planck+WP+lensing** +SN+BAO+H
$\Omega_b h^2$	0.02226 ± 0.00059	0.02221 ± 0.00057	0.02209 ± 0.00058
$\Omega_c h^2$	0.1188 ± 0.0055	0.1196 ± 0.0053	0.1216 ± 0.0053
H_0	69.6 ± 5.9	67.4 ± 3.5	68.8 ± 2.7
n_s	0.966 ± 0.015	0.964 ± 0.014	0.960 ± 0.015
$q_6(z = 2.00)$	$-1.5^{+1.9}_{-1.4}$	$-1.07^{+0.75}_{-1.00}$	$-1.10^{+0.84}_{-1.20}$
$q_5(z = 1.25)$	-1.4 ± 1.2	$-0.89^{+0.47}_{-0.70}$	$-1.21^{+0.64}_{-0.72}$
$q_4(z = 0.85)$	$-1.23^{+0.67}_{-0.70}$	$-0.80^{+0.29}_{-0.41}$	$-0.99^{+0.36}_{-0.48}$
$q_3(z = 0.50)$	$-0.93^{+0.29}_{-0.34}$	-0.98 ± 0.24	-1.02 ± 0.22
$q_2(z = 0.25)$	-1.04 ± 0.17	-1.06441 ± 0.17	$-1.11^{+0.13}_{-0.14}$
$q_1(z = 0.00)$	-0.98 ± 0.28	$-1.01^{+0.30}_{-0.29}$	$-1.08^{+0.21}_{-0.22}$
$100\,\theta$	1.0417 ± 0.0012	1.0416 ± 0.0012	1.0414 ± 0.0012
Ω_Λ	0.707 ± 0.054	0.687 ± 0.032	0.696 ± 0.025
Ω_m	0.293 ± 0.054	0.313 ± 0.032	0.304 ± 0.025
Age/Gyr	13.68 ± 0.25	13.81 ± 0.11	13.767 ± 0.096

Table 5.6: Table shows results from this CMB shift parameters analysis, in combination with SN, SN+BAO, and SN+BAO+H. Confidence intervals are at 95 %.

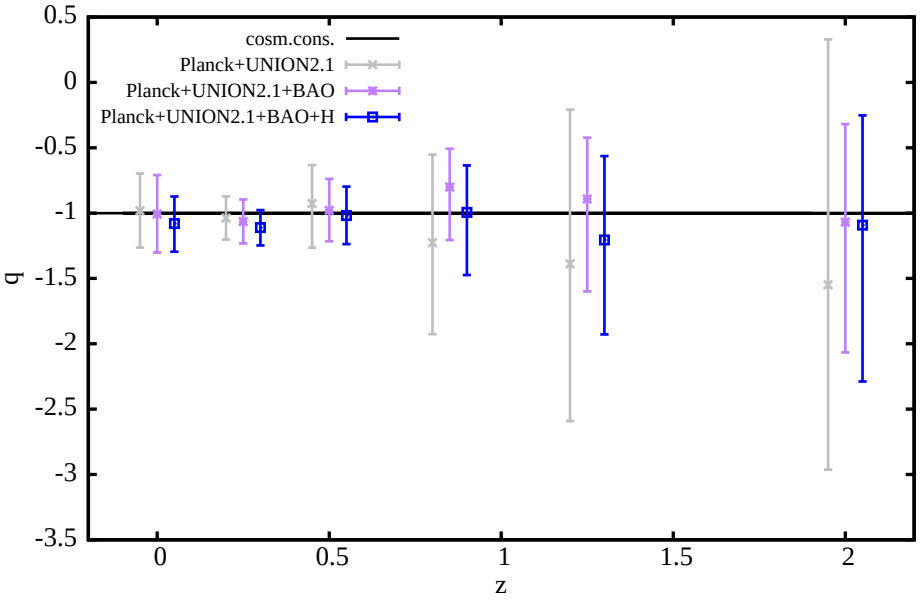

Figure 5.5: Results for the uncorrelated parameter $q_i(z)$ in this CMB shift parameters analysis. These limits can be safely used to constrain parameter space of different dark energy and modified gravity models, in that they do not include any perturbation evolution information.

-1. These constraints should be included in a future work about effective field theory parametrisation of different dark energy models, as explained in [90].

My reference papers

10.1103/PhysRevD.88.043515 N. Said, C. Baccigalupi, M. Martinelli, A. Melchiorri and A. Silvestri, "*New Constraints On The Dark Energy Equation of State*", Phys. Rev. D **88**, 043515 (2013) [arXiv:1303.4353 [astro-ph.CO]].

Submitted and waiting for publication N. Said - '*Dark energy equation of state: a PCA approach*' - Proceedings of the Enrico Fermi School, Varenna.

Chapter 6

Interacting dark sector

'There's a gap in between
There's a gap where we meet
Where I end and you begin...'

Radiohead - Where I End And You Begin

This last chapter is devoted to my research work about interacting dark sector scenarios, which aim to describe the present Universe accelerated expansion as the result of interactions within dark matter and dark energy. This solution can give observable features quite identical to the one deriving from a ΛCDM framework. This is a good point in that it can well reproduce the Universe we live in, but at some level it can result not discernible from ΛCDM. Some classes of these models are however viable for verification, because of the production of observable features in CMB and matter spectra.

6.1 Unified models and interacting vacuum

Unified dark matter (UDM) models identify dark matter and dark energy as a unique fluid with a particular EOS that can represent both the behaviours, the gravitational attraction of matter and the repulsive effect of dark energy. These models do not answer the coincidence problem, but in some way they make it weaker from a theoretical point of view. In general they predict a non-negligible Jeans length scale that produces huge effects on small structures and ISW. This makes them compatible with observations only for values of their parameters that do not allow the distinction with a ΛCDM model. A small value for the Jeans length can be however recovered in the limit of a fast transition between an Einstein - De sitter CDM-like epoch and a ΛCDM-like one [91]. Starting from the metric perturbation in conformal gauge, as

in equation 2.6, one can define the plane wave perturbation:

$$u = \frac{2\phi}{\sqrt{\rho + p}} \tag{6.1}$$

with ϕ the gravitational potential and ρ and p density and pressure of the fluid, respectively. For the evolution of this perturbation u one obtains the second order differential equation [92]:

$$u^{''} + k^2 c_s^2 u - \frac{\Theta^{''}}{\Theta} = 0 \tag{6.2}$$

where derivatives are with respect to conformal time, c_s^2 is the fluid effective sound speed and Θ is defined as:

$$\Theta = \sqrt{\frac{\rho}{3(\rho + p)}}(1 + z) \, . \tag{6.3}$$

For an adiabatic fluid one has $c_s^2 = p'/\rho'$. From here one can define the squared Jeans wave number as:

$$k_J^2 = \left| \frac{1}{c_s^2 \Theta} \frac{d^2\Theta}{d\Theta^2} \right| . \tag{6.4}$$

In practise all viable UDM models must satisfy $k_J^2 \gg k^2$, where k is any scale of cosmological interest. The full expression for k_J^2 is the following:

$$k_J^2 = \frac{3}{2}\rho a^2 \frac{(1+w)}{c_s^2} \left| \frac{1}{2}(c_s^2 - w) - \rho \frac{dc_s^2}{d\rho} + \frac{3(c_s^2 - w)^2 - 2(c_s^2 - w)}{6(1+w) + \frac{1}{3}} \right| \tag{6.5}$$

showing that one can obtain large k_J^2 in two limits: when $c_s^2 \to 0$ and when c_s^2 changes rapidly.

These UDM models are mappable into interacting vacuum (IV) models [93]. Starting from matter and vacuum energy-momentum tensors:

$$T_\nu^\mu = P g_\nu^\mu + (\rho + P) u^\mu u_\nu \tag{6.6}$$

$$\check{T}_\nu^\mu = -V g_\nu^\mu \tag{6.7}$$

where hatted quantities refer to vacuum, one can see that the vacuum four-velocity is undefined, because $\check{\rho} = -\check{P} = V$. In presence of interactions between the two components, the conservation of energy and momentum is given by:

$$\nabla_\mu T_\nu^\mu = -Q_\nu \tag{6.8}$$

$$\nabla_\mu \check{T}_\nu^\mu = -\nabla_\nu V = Q_\nu. \tag{6.9}$$

$$\tag{6.10}$$

A general parametrisation for the interaction Q can be the one of [94]. If one identifies the matter component as CDM, then $\rho = \rho_c$ and $P = 0$, and it follows that, at a background level:

$$\dot{\rho_c} + 3H\rho_c = -Q \tag{6.11}$$

$$\dot{V} = Q \ , \tag{6.12}$$

where the interaction is given by:

$$Q \propto H[q_0 + q_c\rho_c + q_V V] \tag{6.13}$$

where q_0, q_c, q_V are dimensionless constant parameters. Solving the continuity equations 6.11 and 6.12 one obtains the background evolution.

6.1.1 Linear Perturbation Theory

Considering as line element the one of a flat FLRW metric:

$$ds^2 = a^2\{-(1+2\phi)d\tau^2 - 2B_i dx^i d\tau + [\ (1-2\psi)\delta_{ij} + 2E_{ij}]\, dx^i dx^j\} \tag{6.14}$$

the four-velocity of the matter reads:

$$u^\mu = [1-\phi, a^{-1}\partial^i v] \quad u_\mu = [-1-\phi, \partial_i\theta] \tag{6.15}$$

where $\partial^i v = a(\partial x^i/\partial t)$ and $\theta = a(v+B)$. One can now define $Q_\mu = Qu_\mu + f_\mu$ with $f_\mu u^\mu = 0$ so to rewrite the conservation equations for the fluids as:

$$\dot{\delta\rho_c} + 3H\delta\rho_c - 3\rho_c\dot{\psi} + \rho_c\frac{\nabla^2}{a^2}(\theta + a^2\dot{E} - aB) = \delta Q + Q\phi \tag{6.16}$$

$$\dot{\delta V} = -\delta Q - Q\phi \tag{6.17}$$

and

$$\rho_c\dot{\theta} - 3c_s^2 H\rho_c\theta + \rho_c\phi = f - c_s^2 Q\theta \tag{6.18}$$

$$-\delta V = -f - Q\theta \ . \tag{6.19}$$

One can eliminate Q and f from previous equations, ending up with one conservation equation for the total energy and one for the total momentum. Assuming a geodesic flow, $Q_\mu = Qu_\mu$:

$$\dot{\delta\rho_c} + 3H\delta\rho_c - 3\rho_c\dot{\psi} + \rho_c\frac{\nabla^2}{a^2}(\theta + a^2\dot{E} - aB) = \dot{\delta V} \tag{6.20}$$

$$\dot{\theta} + \phi = 0 \ . \tag{6.21}$$

The co-moving synchronous gauge is the most natural choice since there is only one four-velocity (the matter one) defined in this scenario, and in this case $\phi = 0$ and $\theta = 0$. This leads to standard perturbation equations for the CDM component (refer to 2.31) and no perturbations for the vacuum (valid only in this particular gauge choice). The change in the evolution of the anisotropies, then, comes solely from the change in the background evolution.

6.1.2 Mapping of UDM in IV

As an example here I map a particular UDM model into an interacting vacuum one, in order to obtain a model with an identical background evolution, but different perturbation equations and in particular a null value of the sound speed at every time. In this way one can avoid instabilities in the clustering of the matter that eventually lead to strong features in the matter power spectrum. I start with a functional form for the total density, as defined in [92]:

$$\rho = \rho_t\Big(\frac{a_t}{a}\Big)^3 + \rho_\Lambda\left[1 - \Big(\frac{a_t}{a}\Big)^3\right]A(a_t - a) \tag{6.22}$$

where ρ_t is the value of the total energy density at the transition, ρ_Λ is the asymptotic value of the density (when $\rho_c \to 0$) and $A(a_t - a)$ is the function representing the transition, namely

$$A(a_t - a) = \frac{1}{2} + \frac{1}{\pi}\arctan[\beta(a_t - a)] \tag{6.23}$$

with a_t the scale factor at the transition time and β a steepness parameter.

The first step is to determine which part of this total energy acts as an interacting vacuum, and which other evolves as a cold dark matter component. In order to make this identification I use the two Friedmann equations 1.7 and 1.8 and the continuity equation for the total density 1.9. By deriving equation 6.22 with respect to the cosmic time, one obtains:

$$\dot{\rho} = -3H\rho - 3H\rho_\Lambda A - \rho_\Lambda\dot{A}\Big[1 - (a_t/a)^3\Big] \tag{6.24}$$

and comparing to 1.9 one can state:

$$P = -\rho_\Lambda A - \frac{\rho_\Lambda\dot{A}\Big[1 - (a_t/a)^3\Big]}{3H}\ . \tag{6.25}$$

Because what I want is an interaction between two fluids that behave as cold dark matter and vacuum, I will impose that:

$$\rho = \rho_c + V \qquad P = P_v = -V \tag{6.26}$$

$$\dot{\rho_c} + 3H\rho_c = Q_c \qquad \dot{V} = Qv \tag{6.27}$$

where, in order to respect the conservation of the momentum we must have $Q_c = -Q_V$. Identifying P as $-V$ one can determine also ρ_c:

$$V = \rho_\Lambda A + \frac{\rho_\Lambda \dot{A}\Big[1 - (a_t/a)^3\Big]}{3H} \tag{6.28}$$

$$\rho_c = (\rho_t - \rho_\Lambda A)\Big(\frac{a_t}{a}\Big)^3 - \frac{\rho_\Lambda \dot{A}\Big[1 - (a_t/a)^3\Big]}{3H} \tag{6.29}$$

Deriving now this two equations with respect to cosmic time one ends up with the form of the interaction:

$$\dot{V} = \rho_\Lambda \dot{A} + B = Q_V \tag{6.30}$$

$$\dot{\rho_c} = -3H\rho_c - \rho_\Lambda \dot{A} - B = -3H\rho_c + Q_c \tag{6.31}$$

where the term B is:

$$B = \rho_\Lambda \dot{A}[1 - (a_t/a)^3] + \frac{\rho_\Lambda \ddot{A}[1 - (a_t/a)^3]}{3H} - \frac{\rho_\Lambda \dot{A}\dot{H}[1 - (a_t/a)^3]}{3H^2} \tag{6.32}$$

so that the interaction is simply:

$$Q_V = -Q_c = \rho_\Lambda \dot{A}[2 - (a_t/a)^3] + \frac{\rho_\Lambda \ddot{A}[1 - (a_t/a)^3]}{3H} - \frac{\rho_\Lambda \dot{A}\dot{H}[1 - (a_t/a)^3]}{3H^2} \tag{6.33}$$

I determine now an equivalent form of the interaction, in particular expressing the derivatives of the transition function A in terms of typical variables. This is straightforward for the first and the third term of the total interaction Q_V. Indeed, noting that:

$$\rho_\Lambda \dot{A}\Big[1 - (a_t/a)^3\Big] = 3H(V - \rho_\Lambda A) \tag{6.34}$$

it follows:

$$Q_V = 3H(V - \rho_\Lambda A)\left(\frac{2 - (a_t/a)^3}{1 - (a_t/a)^3}\right) + \frac{\rho_\Lambda \ddot{A}[1 - (a_t/a)^3]}{3H} - \frac{\dot{H}}{H}(V - \rho_\Lambda A) \tag{6.35}$$

The second term can be rewritten as:

$$\frac{\rho_\Lambda \ddot{A}[1 - (a_t/a)^3]}{3H} = \frac{\ddot{A}}{\dot{A}}(V - \rho_\Lambda A) \tag{6.36}$$

so that computing the derivatives of A leads to:

$$\frac{\ddot{A}}{\dot{A}}(V-\rho_\Lambda A)=\left[\frac{\dot{H}}{H}+H\left(1-\frac{2\beta^2 a(a_t-a)}{1+\beta^2(a-a_t)^2}\right)\right](V-\rho_\Lambda A) \tag{6.37}$$

obtaining for the interaction, finally:

$$Q_V=H(V-\rho_\Lambda A)\left(\frac{6-3(a_t/a)^3}{1-(a_t/a)^3}-\frac{1+\beta^2(a_t^2-a^2)}{1+\beta^2(a-a_t)^2}\right) \tag{6.38}$$

6.2 Late time interaction

Now that I defined the framework I can introduce my work on interacting vacuum that led to the determination of a best fit model that can assure agreement between low and high red-shift measurements: the late time interaction. The initial point of this work was to study the evolution with the red-shift of a possible interaction between vacuum and matter. In [94] authors performed a background analysis with SN data, showing that a model with $q_0 = 0$ and $q_c = 0$ is preferred. Following their work I chose an interaction of the form:

$$Q=-q_V HV \tag{6.39}$$

where q_V is a time-varying quantity $q_V \equiv q_V(z)$. Integrating the continuity equations 6.11 and 6.12 one obtains for the background evolution (see [95]):

$$V=V_0 a^{-q_V} \tag{6.40}$$

$$\rho_c=\rho_{c,0}a^{-3}+V_0\frac{q_V}{-3+q_V}(a^{-3}-a^{-q_V}) \tag{6.41}$$

and for the sum of the coupled fluid densities:

$$\rho_c+V=\left[\rho_{c,0}-V_0\frac{q_V}{3-q_V}\right]a^{-3}+\frac{3}{3-q_V}V_0 a^{-q_V}\ . \tag{6.42}$$

I considered $q_V < 0$ so that both the energy densities in (6.40) and (6.41) are always positive defined. If $q_V = 0$ the (6.42) reduces properly to the standard ΛCDM case.

I used the following combination of cosmological probes: CMB data from Planck+WP, SN from the compilation Union2.1 and RSD measurements reported in Section 1.3.3. The tension in the σ_8 determination between CMB and RSD data that arises in a ΛCDM scenario is solved in this interacting model, named iVCDM, making possible to combine the two datasets. I tested that the inclusion of BAO data and other standard candles measurements

reaching higher red-shifts (Radio Galaxies calibrated with SN, see [96]) do not alter the constraints of SN alone.

To study the temporal evolution of $q_V(z)$ I subdivided the red-shift range from last scattering until today in four bins as reported in Fig. 6.1 and illustrated below:

- bin 1 from $z = 2.5$ to z_{CMB}, to account for CMB data;
- bin 2 from $z = 0.9$ until $z = 2.5$, that includes the farther SN measurements;
- bin 3 from $z = 0.3$ to $z = 0.9$, mostly sensitive to RSD data;
- bin 4 from $z = 0$ to $z = 0.3$, mostly sensitive to SN measurements.

I assumed a constant q_V inside each bin and I used a *tanh* function to interpolate between different bins, to ensure continuity. I assumed a negative

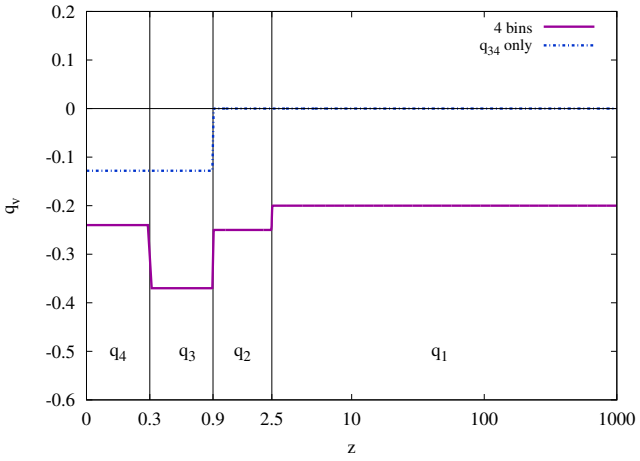

Figure 6.1: Sketch of the interaction strength $q_V(z)$ subdivided in red-shift bins in iVCDM model. In the i-th bin the interaction parameter $q_V(z)$ takes the constant value q_i.

q_V everywhere, to ensure that the matter density remains non-negative in the past, adopting a linear prior on the interaction parameters $q_i = [-10, 0]$. I have verified that the magnitude of q_V is of order one and that the same results are obtained when considering a wider logarithmic prior, see Fig.6.11. Beside the four values of q_i I sampled over the standard 6 cosmological parameters: $\Omega_b h^2$, $\Omega_c h^2$, θ, τ, n_s and A_s with usual priors on them.

The interest in exploring a *time-varying* strength of the interaction comes because a $q_V = const$ along the full evolution of the Universe is not preferred by data, as shown in Fig.6.2. There is no evidence of interaction; moreover the strong tension between the CMB and the RSD estimate of σ_8 implies that the strong limits given by the combination of these two datasets are not reliable. A constant interaction in the dark sector is statistically highly disfavoured compared to a simple ΛCDM model, as demonstrated by the fact that the best fit χ^2 value for the interacting model is higher than the value for ΛCDM despite the interacting model has one more parameter.

In the 4-bin analysis the situation changes, as shown in Fig.6.3 and Fig.6.4. There is a preference for a non-zero value of q_i in the high red-shift bins that is clearly driven by the full degeneracy between the strength of the interaction and $\Omega_c h^2$. In the fourth bin, indeed, where the degeneracy is weaker, a null value is preferred. Combining CMB and RSD measurements together imposes a lower limit on the amount of cold dark matter, excluding the zero value for $\Omega_c h^2$. This fact implies a reduction of the degeneracy between $\Omega_c h^2$ and the interaction parameters, as clearly shown in Fig.6.4, and a shift in the posterior distributions. Numerical results are reported in Tab.6.1. This leads to exclude at 99% c.l a zero interaction in the third bin and at 95% c.l a zero interaction in the fourth bin, suggesting that a late-time interaction, at $z < 1$, is in very good agreement with measurements, see also Tab.6.2. It should be noticed that the tension in the σ_8 value as measured from CMB and from RSD is solved in this case, making reliable the combination of this two datasets.

I performed a PCA as previously made for a time-varying dark energy EOS $w(z)$. However a PCA approach, both with the Serra and Cooray method and the standard one, is not helping in this case, as we can clearly see in Fig.6.5. Applying the Serra and Cooray method to this case one obtains very large weights, meaning that the assumption of the mild correlation is false and the use of this method does not maintain the red-shift localization.

On the other side, following the standard approach one can only notice that a mode where the interaction is favoured exists, however its red-shift behaviour is unknown.

Since a late time interaction is preferred from data and the issues with PCA are mainly due to the large and very poorly constrained 1st bin [71] next step was considering a late time interaction in the bin 2, 3 and 4. The interaction value in the first bin has been fixed to zero, in practice allowing an interaction only at red-shifts lower than 2.5. The assumption of no interaction at early time breaks the degeneracy between $\Omega_c h^2$ and the late-time interaction parameters (see Fig.6.7) and this pushes the probability distributions of the interaction parameters towards null values when considering

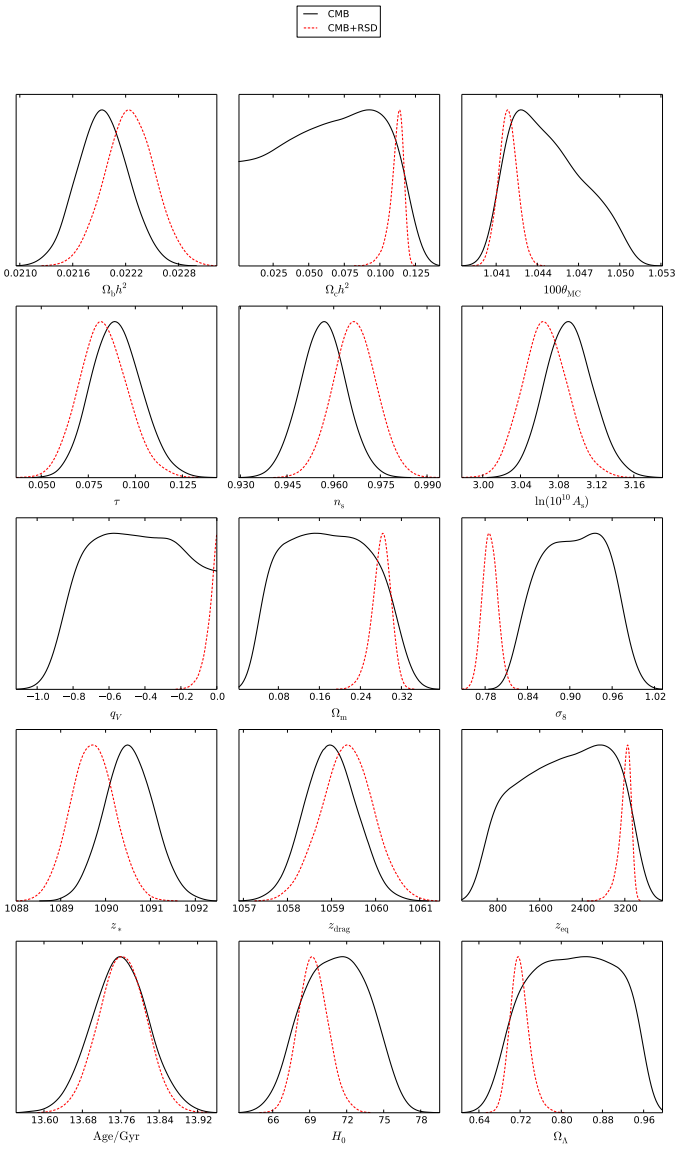

Figure 6.2: Posterior distributions of cosmological parameters when considering an interacting vacuum model with interaction $Q = q_V HV$ with q_V constant in time. In black line the results from CMB, in red line the results from the combination CMB+RSD. The tension in σ_8 estimation with or without RSD measurements inclusion is evident.

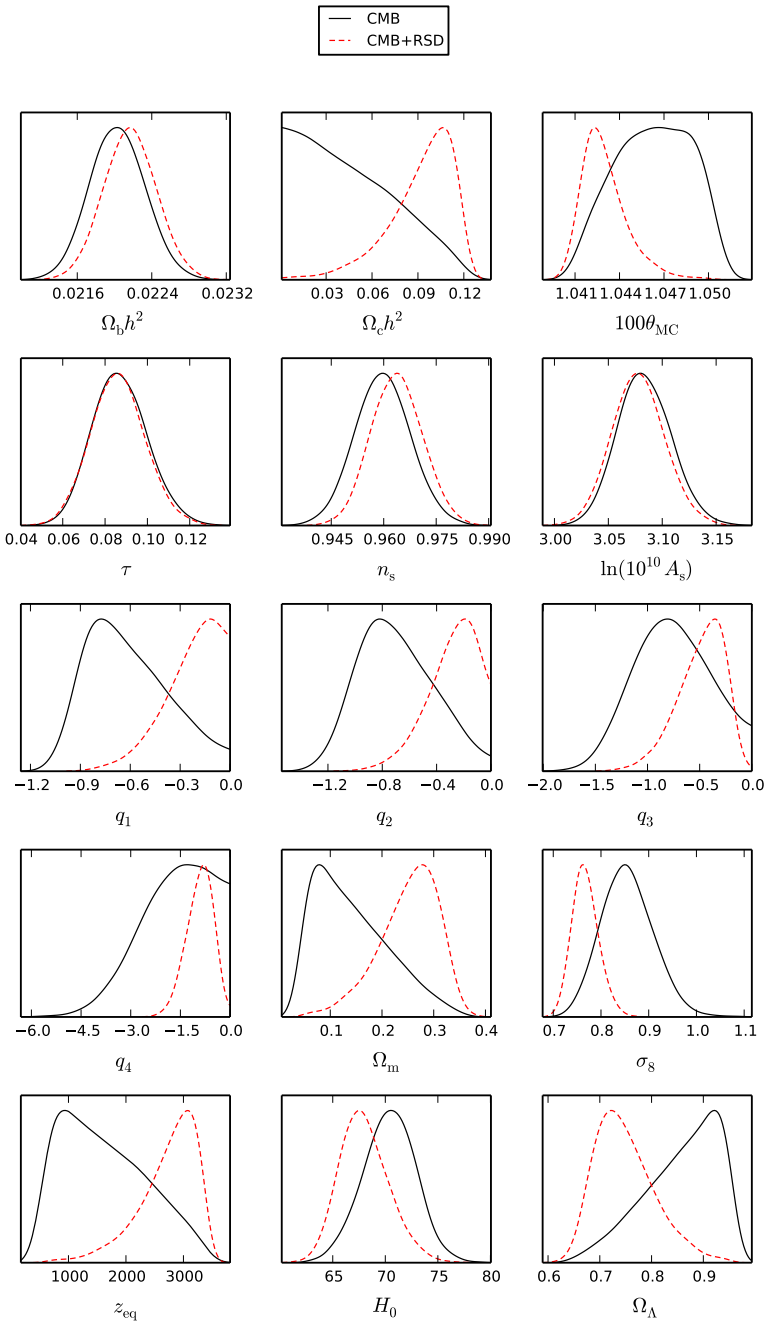

Figure 6.3: Posterior distributions of cosmological parameters when considering an interacting vacuum model with interaction $Q = q_V HV$ where q_V is a binned function of the red-shift. Black line shows results from CMB, red line results from the combination CMB+RSD. The introduction of RSD measurements fixes a minimal amount of CDM, posing constraints on coupling parameters that favours a low red-shift interaction.

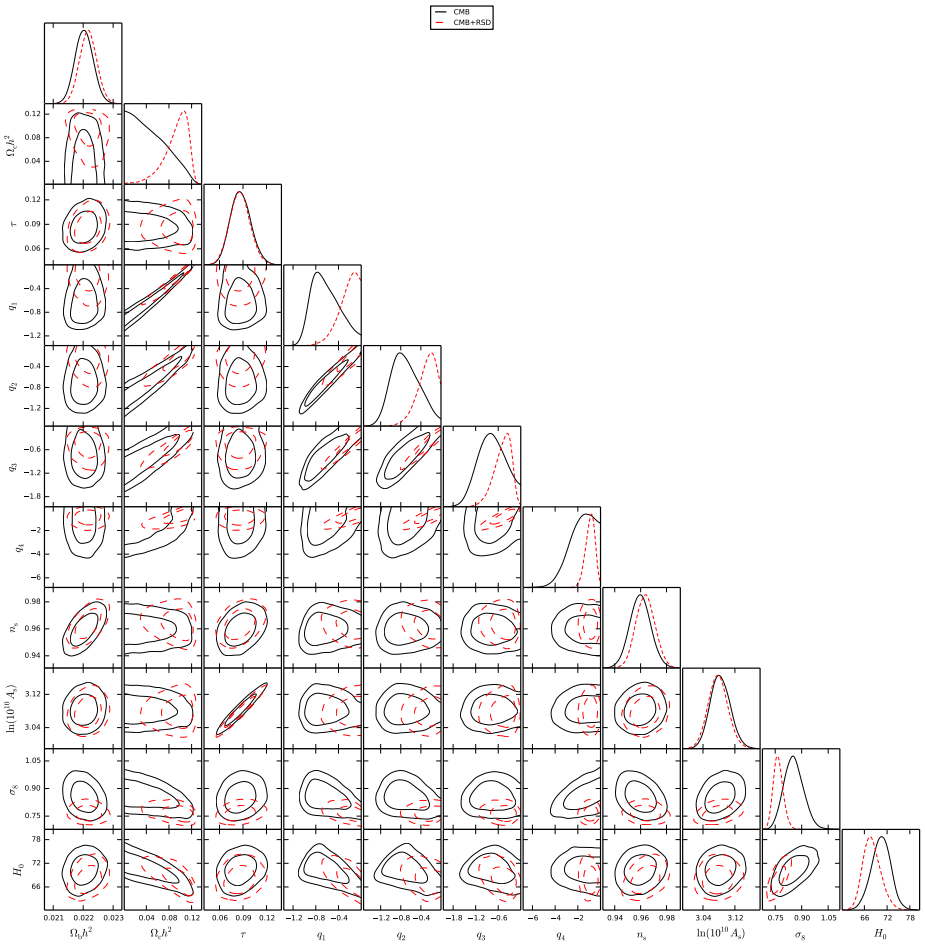

Figure 6.4: Degeneracies between cosmological parameters when considering an interacting vacuum model with interaction $Q = q_V HV$ where q_V is a binned function of red-shift. In black solid line the results from CMB, in red dashed line the results from the combination CMB+RSD.

Parameters	Planck	Planck+SN	Planck+RSD
$\Omega_b h^2$	0.02203 ± 0.00029	0.02203 ± 0.00029	0.02217 ± 0.00028
$\Omega_c h^2$	< 0.060	$0.049^{+0.018}_{-0.044}$	$0.0918^{+0.026}_{-0.010}$
$100\,\theta$	$1.0463^{+0.0032}_{-0.0024}$	$1.0460^{+0.0023}_{-0.0028}$	$1.04302^{+0.00095}_{-0.00183}$
τ	$0.087^{+0.012}_{-0.014}$	$0.086^{+0.012}_{-0.014}$	$0.086^{+0.012}_{-0.013}$
n_s	0.9597 ± 0.0078	0.9599 ± 0.0078	$0.9638^{+0.0071}_{-0.0078}$
$\log(10^{10} A_s)$	$3.084^{+0.024}_{-0.026}$	$3.082^{+0.024}_{-0.027}$	3.078 ± 0.024
q_1	$-0.62^{+0.18}_{-0.31}$	$-0.61^{+0.21}_{-0.29}$	> -0.29
q_2	$-0.70^{+0.24}_{-0.33}$	$-0.69^{+0.26}_{-0.31}$	$-0.291^{+0.255}_{-0.098}$
q_3	$-0.76^{+0.37}_{-0.40}$	$-0.80^{+0.36}_{-0.42}$	$-0.49^{+0.28}_{-0.16}$
q_4	> -2.12	$-1.58^{+1.51}_{-0.506}$	$-0.92^{+0.48}_{-0.34}$

Table 6.1: Constraints at 68% c.l. on cosmological parameters in the iVCDM model when q_V is allowed to vary in four red-shift bins. Results are from CMB only, CMB+SN and CMB+RSD. The impact of RSD measurements on this analysis is evident.

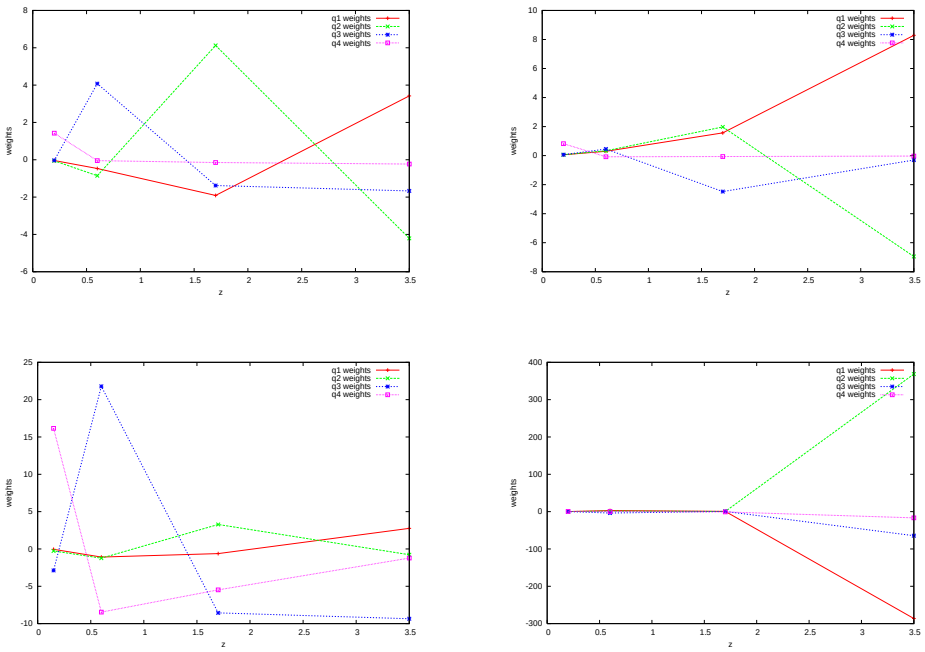

Figure 6.5: Decorrelation weights from PCA. The top row reports results from CMB, the bottom row results from CMB+RSD. On the left the results from Serra and Cooray PCA method, on the right results from the standard PCA decomposition.

CMB and CMB+SN as shown in Fig.6.6. On the contrary, when CMB is combined with RSD data, an evidence for an interaction arises at 99% c.l. in the third bin and at 68% c.l. in the fourth bin (see Tab.6.2).

Applying the decorrelation method of Serra and Coray to this case one obtains good results (see Fig.6.8), and the evidence of interaction in bin 3 is maintained at 95% c.l., as shown in Tab.6.3 and Fig.6.9)

	4bin CMB+RSD		**3bin CMB+RSD**	
Parameters	Best fit	95% limit	Best fit	95% limit
q_1	-0.24	> -0.56	0	[0,0]
q_2	-0.29	> -0.64	-0.081	> -0.18
q_3	-0.49	[-0.96,-0.09]	-0.211	[-0.370,-0.061]
q_4	-0.91	[-1.7, -0.15]	-0.53	> -1.02
$\chi^2_{\rm min}/2$	4905.765		4905.221	

Table 6.2: Interaction parameters for the combination CMB+RSD when considering an interaction along all the cosmic evolution ($q_1 \neq 0$, first column) and when considering instead a late-time interaction ($q_1 = 0$, second column). The latter case is slightly statistically favoured, having one parameter less.

$\widetilde{q}_2$		$\widetilde{q}_3$		$\widetilde{q}_4$	
Best fit	95% limit	Best fit	95% limit	Best fit	95% limit
-0.0349	> -0.156	-0.219	[-0.410,-0.026]	-0.84	> -1.68

Table 6.3: Decorrelated interaction parameters for the combination CMB+RSD when considering a late time interaction. Note that the $\widetilde{q}_i$ parameters are linear combination of the q_i parameters.

The whole previous analysis shows that a model with a "delta-like" interaction in recent epochs, in particular in the red-shift range of the third bin, is the one that better represents the data. It is important at this point to quantify how much this model is preferred compared to other kinds of interacting-models and one-parameter extensions of the ΛCDM scenario.

From Tab.6.4 one sees that a model with an interaction limited to the third bin is favoured compared to models with delta-interactions at different times. The best model, however, is the one that considers a constant interaction in the third and fourth bin (i.e. $q_1 = q_2 = 0$ and $q_3 = q_4 \neq 0$), labelled q_{34}. I compared this results also with a ΛCDM+$\sum m_\nu$ model, another

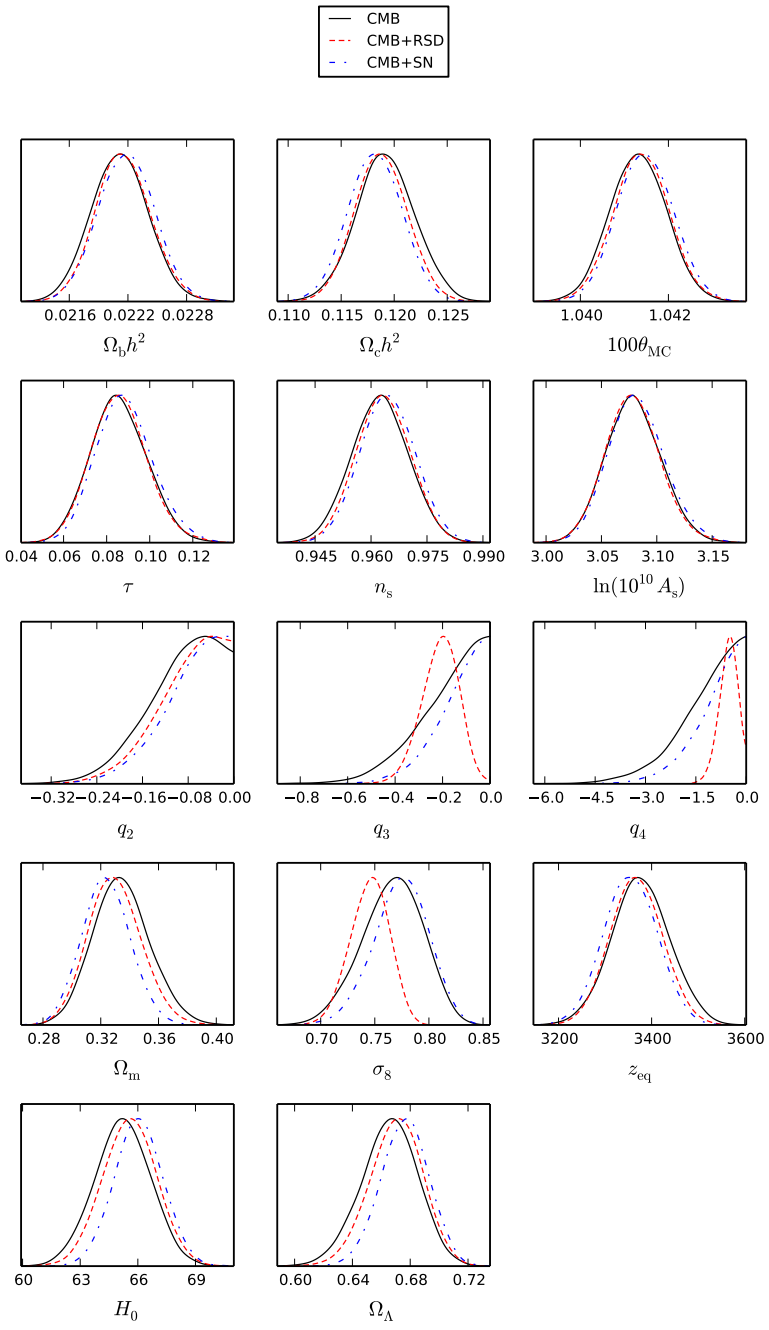

Figure 6.6: Probability distributions of cosmological parameters when assuming a late-time interaction (at $z < 2.5$). In black the results from CMB, in red those from CMB+RSD and in blue those from CMB+SN.

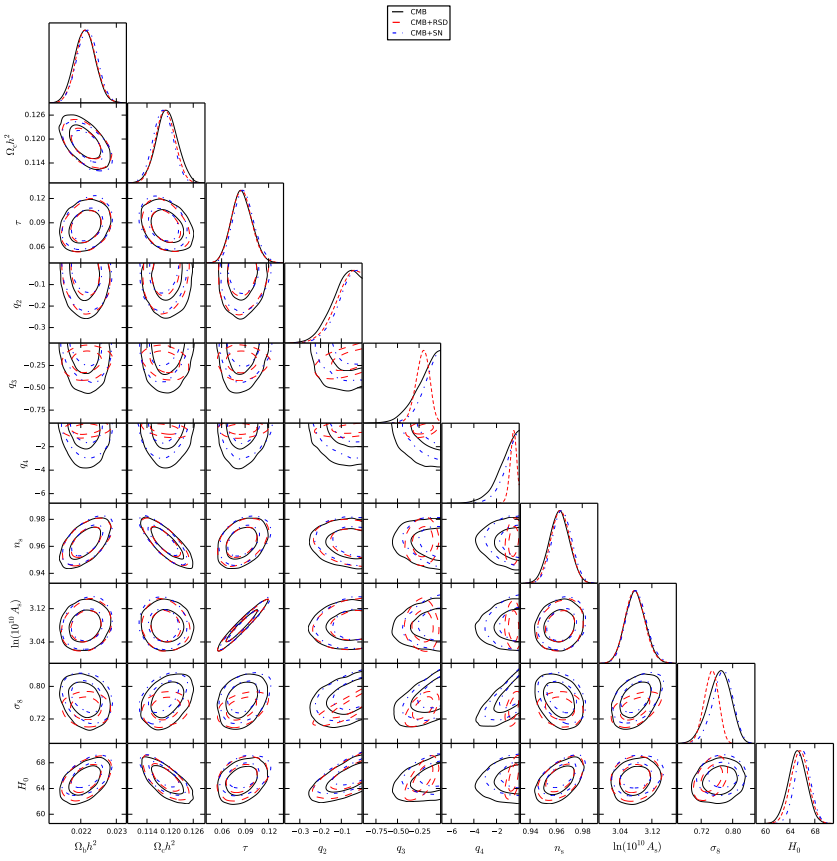

Figure 6.7: Degeneracies between cosmological parameters for a late-time interaction (for $z < 2.5$). In black the results from CMB, in red those from CMB+RSD, and in blue those from CMB+SN. In this case there is a weak degeneracy between $\Omega_c h^2$ and the q parameters. Notice that the degeneracies of σ_8 and H_0 with q_2 and q_3 have changed shape compared to the general case.

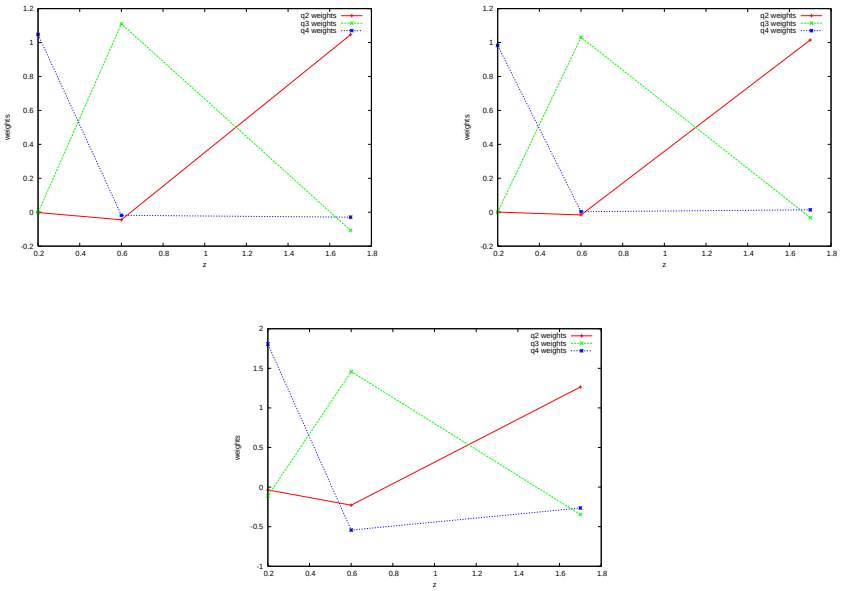

Figure 6.8: Decorrelation weights from PCA with the Serra and Cooray method when assuming a late-time interaction. From top left to bottom: CMB, CMB+SN, CMB+RSD. We can observe that in this case the localisation is well retained since weight factors are small and each bin weakly depends on others. When considering CMB and CMB+SN there is basically no correlation between bins but they are also the less interesting cases, since there is no evidence of interaction anywhere.

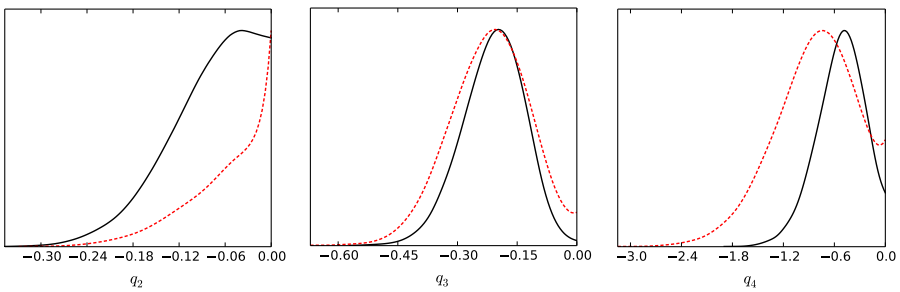

Figure 6.9: Probability distributions for the interaction parameters before (black) and after (red) the PCA decorrelation when a late time interaction is assumed (q_1 is fixed to zero).

one-parameter extension that seems to solve the tension between low and high red-shift measurements [8]. Also in this case indeed the σ_8 the tension between CMB and RSD is alleviated (see Fig.6.10). The interacting model with a late-time interaction starting at $z = 0.9$, however, results preferred also compared to the ΛCDM+$\sum m_\nu$ extension.

To coherently compare the models together, keeping in account the different number of parameters used, I performed some tests using the information criteria introduced in Section 3.4, namely the AIC and the DIC tests. Results are shown in Tab.6.5 and again point toward a strong preference for the q_{34} model.

	$q_2$only	$q_3$only	$q_4$only	q_{34}only	ΛCDM	ΛCDM+$\sum m_\nu$
$\chi^2_{\rm min}$	9818.74	9813.016	9817.252	9810.7	9818.12	9813.014

Table 6.4: In the first 4 columns are reported the best-fit χ^2 values when the vacuum interaction is allowed in one bin at a time. In the fifth column is shown the best-fit χ^2 value when bin 3 and 4 are merged together and a constant $q_3 = q_4$, dubbed q_{34}, is considered as the free extra parameter. For comparison in the sixth and seventh columns I have reported the best fit χ^2 values for ΛCDM and ΛCDM+$\sum m_\nu$. The comparison with ΛCDM must take in account that the standard model has one parameter less than the others reported in the table. Results are all from CMB+RSD.

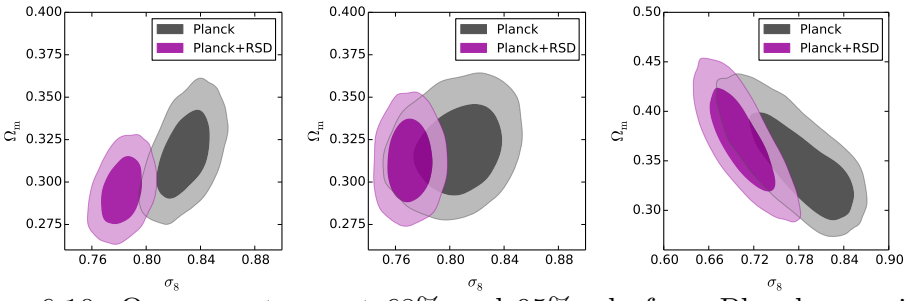

Figure 6.10: Ω_m-σ_8 contours at 68% and 95% c.l. from Planck experiment (black) and Planck+RSD (purple) for three theoretical models. The tension between the Planck and RSD datasets that arises in the ΛCDM model (left) is resolved in the q_{34} interacting vacuum model (middle). Also in the ΛCDM model with massive neutrinos (right) this tension with RSD is alleviated.

model	ΔAIC	ΔDIC
ΛCDM	0	0
q_2 only	2.62	2.40
q_3 only	−3.10	−4.40
q_4 only	1.13	0.34
q_{34}	−5.42	−5.78
$\sum m_\nu$	−3.11	−4.56

Table 6.5: The table shows results from AIC and DIC tests for the different one-parameter extensions of the ΛCDM analysed. They refer to results of CMB+RSD analysis. The preference for the q_{34} model is evident.

6.2.1 Analysis on the late-time interaction q_{34}

Results for the best-fit model q_{34} are reported in Fig.6.11 and in Tab.6.6.

Parameters	Best-fit	Mean
$\Omega_b h^2$	0.02225	0.02216 ± 0.00027
$\Omega_c h^2$	0.1170	0.1183 ± 0.0023
$100\,\theta_{\rm MC}$	1.04150	1.04142 ± 0.00061
τ	0.094	$0.087^{+0.012}_{-0.014}$
n_s	0.9702	$0.9633^{+0.0068}_{-0.0067}$
$\log(10^{10} A_s)$	3.094	3.080 ± 0.024
q_{34}	−0.128	$-0.156^{+0.068}_{-0.056}$

Table 6.6: Constraints at 68% c.l. on fundamental cosmological parameters for the iVCDM model with $q_V = q_{34}$.

To test the strength of these results one can quantify easily the evidence of this late-interaction model with respect to the ΛCDM using the Savage-Dickey density ratio formula 3.17. However the Bayes evidence is highly dependent on the prior choice (see 3.16), and given the fact that in this case no theoretical reasoning can help to determine a supported prior, this comparison is not straightforward. However I computed the evidence for different ranges of the prior, measured in σ from the mean value and used this approach also on the other preferred model just shown, the ΛCDM+$\sum m_\nu$. The conclusion is that a late time interaction is always preferred compared to a model with massive neutrinos, showing that an interaction mechanism can solve low and high red-shift measurements discrepancies better than massive neutrinos, see Fig.6.12.

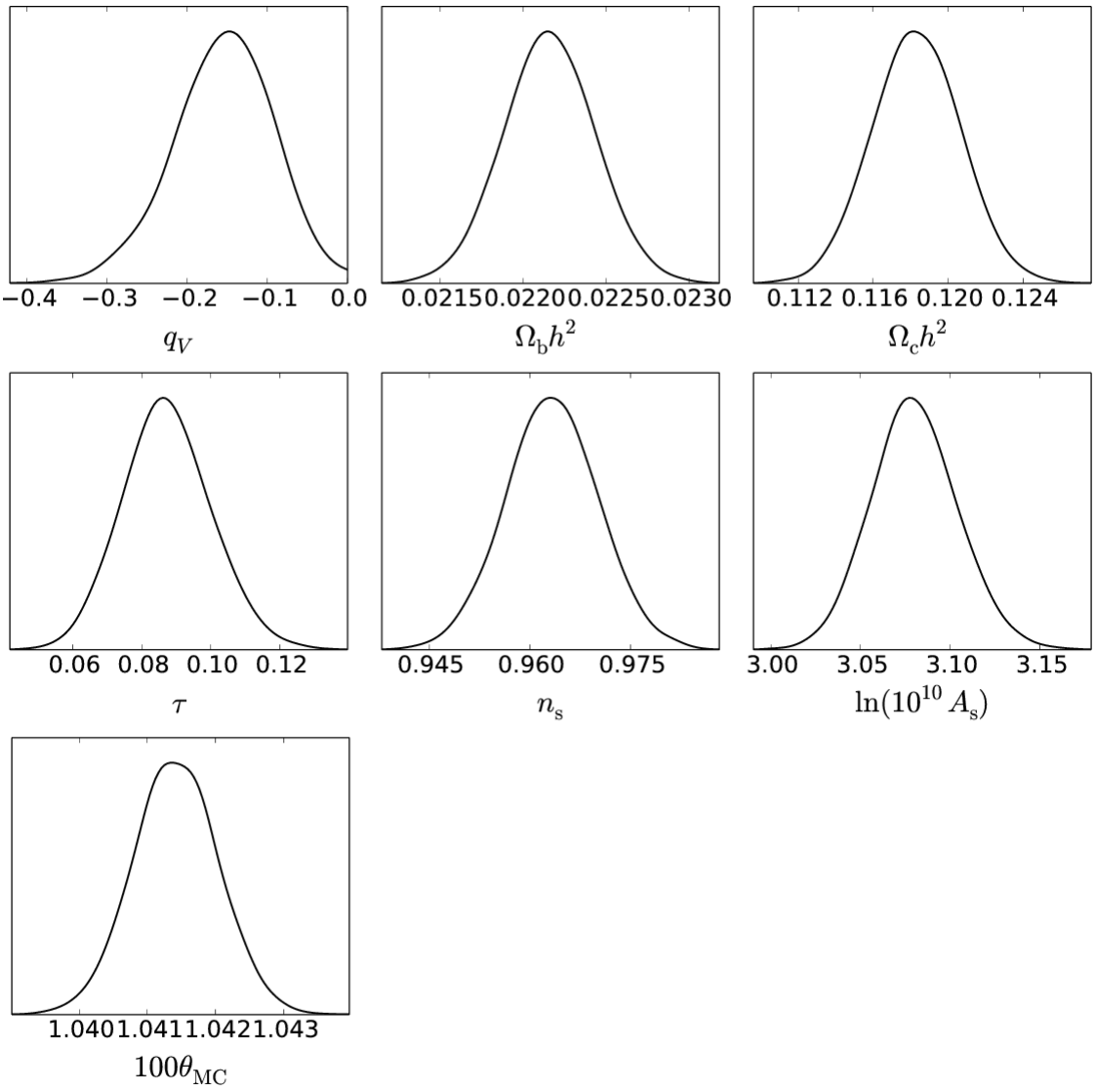

Figure 6.11: Posterior distributions for the q_{34} model for the cosmological parameters of interest. The confidence on an interaction reaches the 99% level.

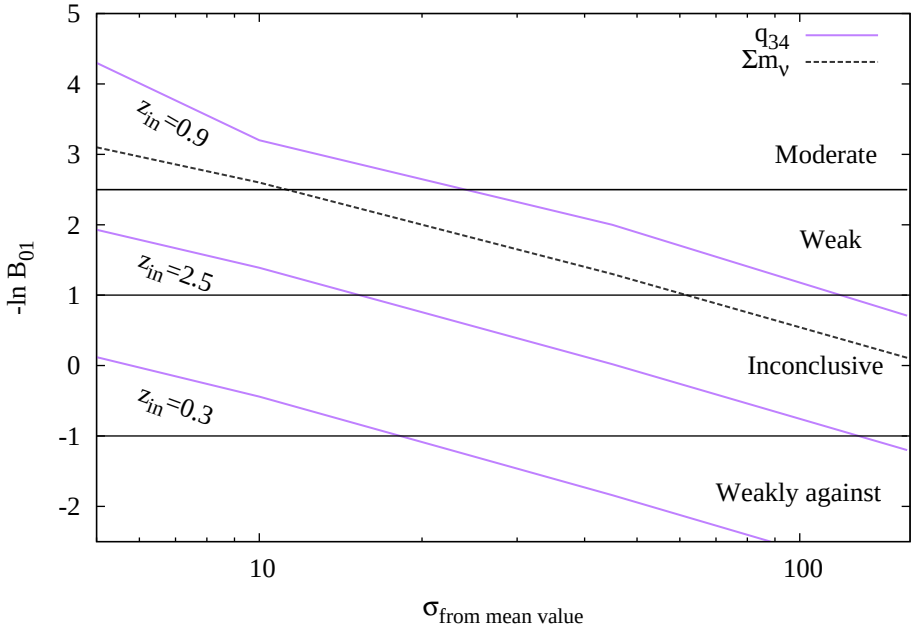

Figure 6.12: Bayesian evidence with respect to a ΛCDM model as a function of the prior width, expressed in terms of standard deviations from the mean value of the nested parameter. In purple (solid line) the q_{34} model (z_{in}=0.9) and same model with different choices of z_{in}. In grey (dashed line) the ΛCDM+$\sum m_\nu$ model. On the right we report the empirical Jeffreys' scale.

To determine the favoured red-shifts for the interaction to start and terminate, a further analysis was performed, adding two more parameters to the MCMC chains: z_q^{in} and z_q^{fin}, namely the starting and ending points of an interaction of strength q_V. This analysis showed that an ending point for the interaction is not detectable from present observations, meaning either that we have not enough sensibility, or that the interaction is not ended yet. Discarding for this reason z_q^{fin} from the parameter set the result for the starting point is $z_q^{in} = 1.1 \pm 0.7$, with a best-fit value of $z_q^{in} \sim 0.9$, perfectly matching the one chosen arbitrarily in the previous analysis. Beside this lucky guess, however, the analysis shows a very large upper limit for z_q^{in} ($z_q^{in} < 2.5$ at 95% c.l.). The two-dimensional plot for the posteriors of q_V and z_q^{in} is shown in left panel of Fig.6.13.

The posterior of q_V for this case is reported in right panel of Fig.6.13, beside the posterior obtained in the q_{34} case (in which $z_q^{in} = 0.9$) and the one

obtained using a logarithmic prior, inside $[-10^3; -10^{-3}]$ on the interaction strength, in order to test if the assumption of the range $[-10; 0]$ was leaving something important out of the analysis. The agreement between the results with logarithmic and flat priors shows that this was not the case.

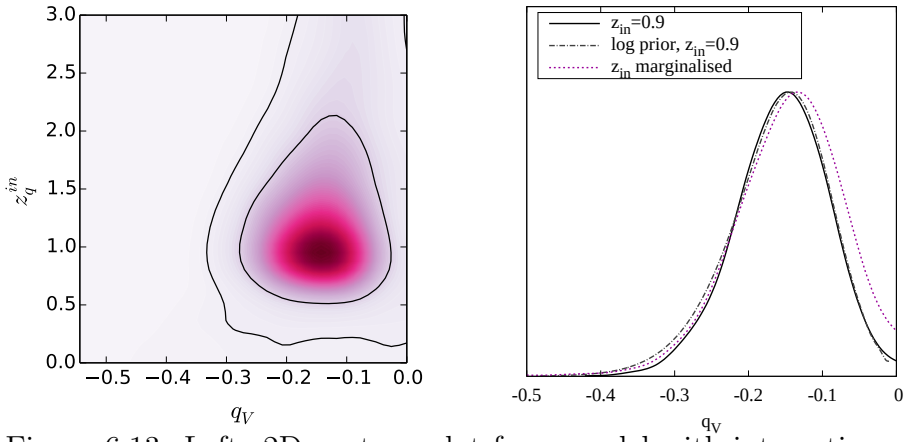

Figure 6.13: Left: 2D contour plot for a model with interaction q_V starting at z_q^{in}. The contours correspond to 68% and 95% c.l. As we can expect there is a large degeneracy between parameters, however the interaction is mostly favoured when z_q^{in} is around 0.9. Right: posterior distribution for q_V in a model with $z_q^{in} = 0.9$ with flat (black line) and logarithmic prior (grey line), and in the model with z_q^{in} allowed to vary with flat prior on q_V (purple line). All models agree; the one with the extra parameter z_q^{in} results clearly in a wider posterior for q_V.

As previously stated in Section 1.3.3, to use RSD data with models that assume a non-ΛCDM background evolution, is necessary to take in account the distortions due to the Alcock-Pacinsky effect. The angular corrections are taken in account with the quantity $D_V(z)$ (1.28), while the line-of-sight corrections depend on the offset of H_0, computed using the AP parameter $F(z)$ (1.40).

A complete analysis, thus, must implement a comprehensive likelihood of these three quantities. The full set of three measurements and their covariance matrices, however, are available only for the few red-shifts of Tab.1.2. I performed an analysis including only these red-shifts and another combining them with the other $f\sigma_8$-only measurements of Tab.1.1. The results are shown in Fig.6.14 and Fig.6.15 for both the 4-bin and the q_{34} cases. Clearly the addiction of D_V and F data that are in perfect agreement with ΛCDM lowers the evidence of an interaction. However if one plots directly the AP observable F the deviations from the ΛCDM behaviour are negligible, as

shown in Fig.6.16, justifying the absence of geometrical corrections in the overall analysis.

Correlations with other parameters In the overall analysis of the interacting scenario the lensing amplitude parameter A_L is held fixed to the standard value 1. Given its strange value measured by Planck, and given the strong relation among lensing and LSS clustering I studied whether the previous result may be affected by the lensing amplitude marginalization. I added thus as free parameter also A_L in the 3-bin model. Fig.6.17 shows that there is a degeneracy between the A_L parameter and the strength of the interaction in the bins where we get an evidence for the latter.

Moreover, to balance the higher value of A_L, the q_3 and q_4 posteriors are shifted a little towards zero, making the exclusion of a null interaction weaker but still largely favoured.

Finally, since both the vacuum interaction and the massive neutrinos shift the growth rate in the same direction, a degeneracy between those two parameters is expected. Considering a q_{34} model with massive neutrinos we obtain a clear degeneracy between them, as shown in Fig.6.18.

In summary, this interacting model is capable of solving the tension between high and low red-shift measurements introducing an extra parameter that encodes the strength of this coupling between dark energy and dark matter. The strong evidence for this model comes out when combining CMB and RSD measurements, combination made possible thanks to the better agreement among CMB and RSD σ_8 predictions in this interacting scenario. The best-fit model is the one that allows for an interaction in the dark sector starting around $z = 0.9$; its preference with respect to the standard ΛCDM model and its favoured extension ΛCDM+$\sum m_\nu$ is evident. As expected the interaction parameters are degenerate with the lensing amplitude A_L and $\sum m_\nu$. The matching of this best-fit model with the low-red-shift observation is well depicted in Fig.6.19.

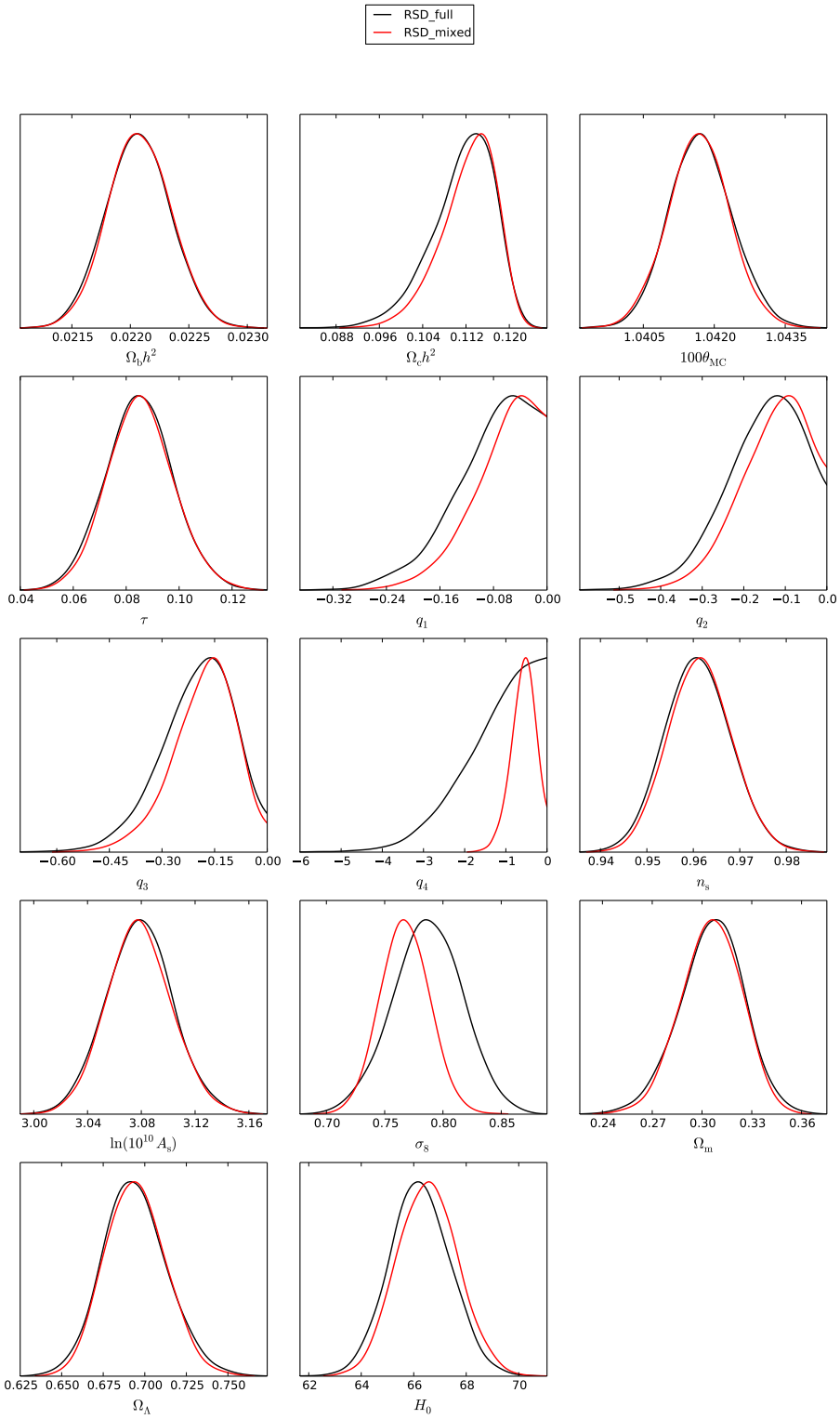

Figure 6.14: Posterior distributions for the 4-bin case obtained when using complete $f\sigma_8$+F+D_V data only (RSD full, black line) and these same data combined with $f\sigma_8$-only measurements (RSD mixed, red line). As clearly shown, the evidence for an interaction is weaker, given the strong agreement of the ΛCDM model with the geometric data included.

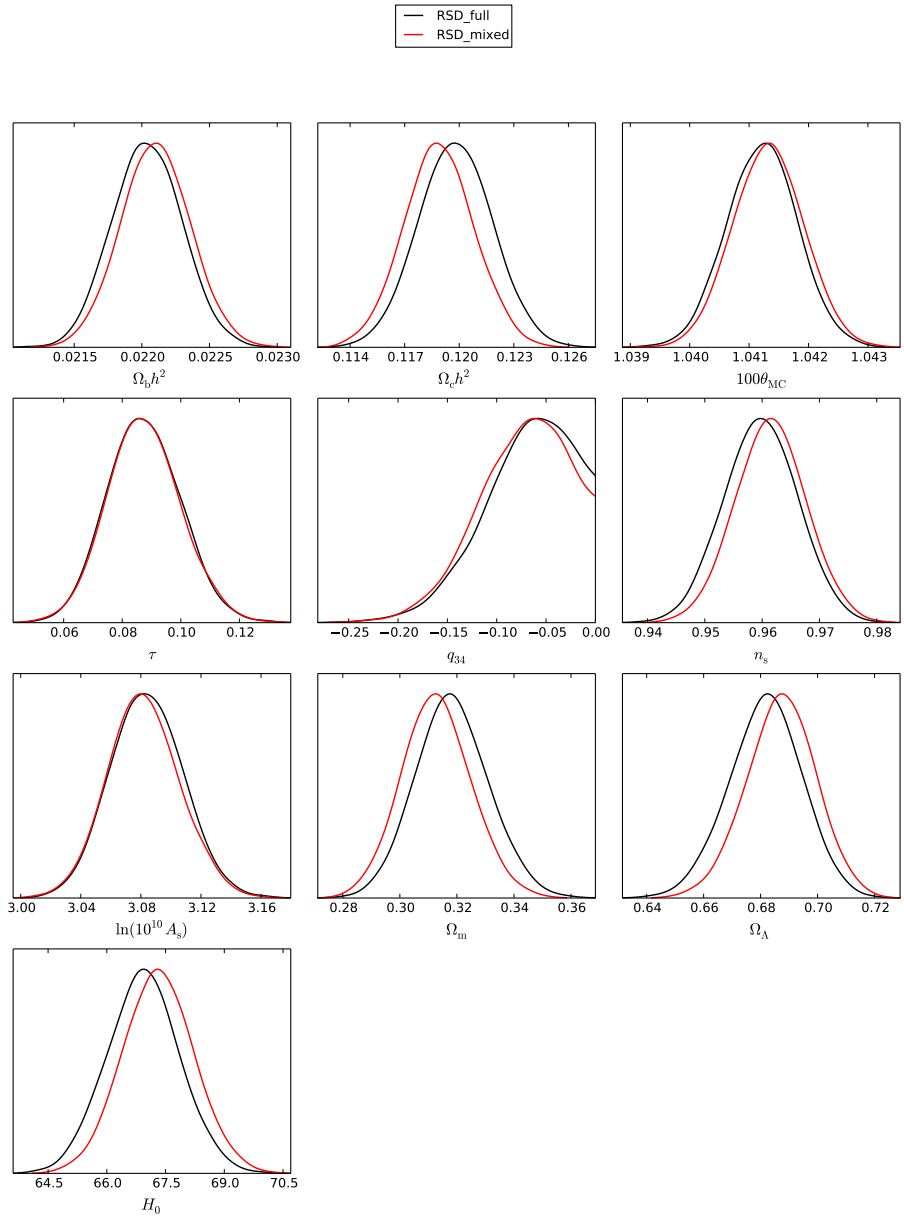

Figure 6.15: Posterior distributions for the late interaction case obtained when using complete $f\sigma_8$+F+D_V data only (RSD full, black line) and these same data combined with $f\sigma_8$-only measurements (RSD mixed, red line). Also in this case the evidence for an interaction is lowered.

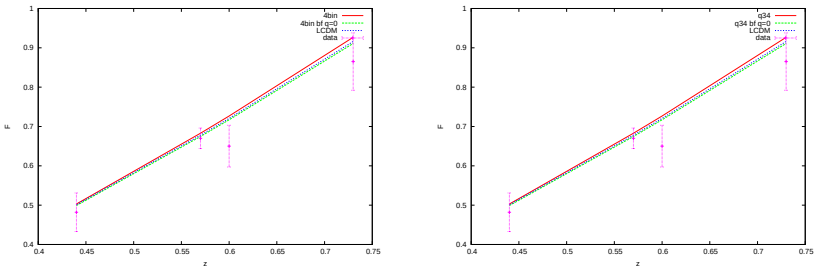

Figure 6.16: red-shift dependence of the AP parameter F for the 4-bin case (left) and the q_{34} case (right). In each plot I report the results for the q_{34} best fit model (red line), for the same model with the interaction set to zero (blue line) and for the ΛCDM Planck best fit (green line). In pink are also shown the data-points of Tab.1.2. Deviations from a ΛCDM scenario are not significant.

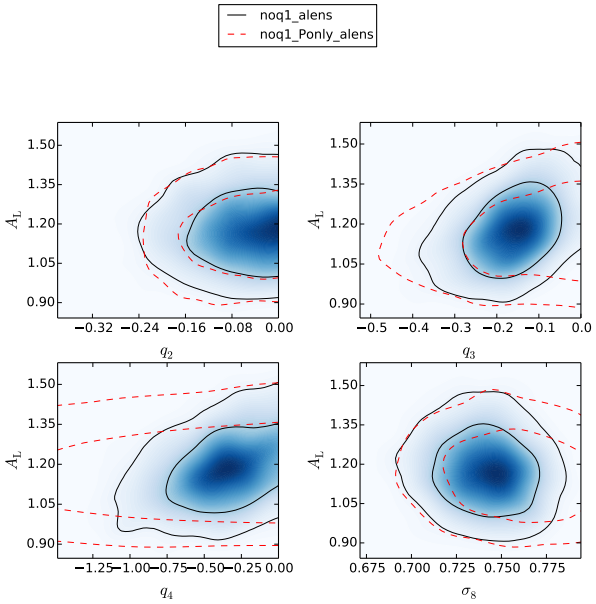

Figure 6.17: 2D contour plot for a model where I consider a late-time interaction with q_V varying in 3 bins and a varying lensing amplitude A_L. In red lines the results from Planck only, in black lines the results from Planck+RSD. We can observe the degeneracy among A_L and q_3 and q_4 when considering Planck+RSD combination.

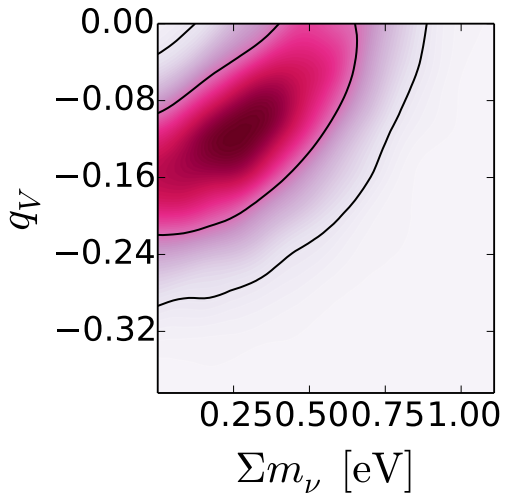

Figure 6.18: Degeneracy between the strength of the vacuum interaction and the mass of neutrinos in the iVCDM+$\sum m_\nu$ model.

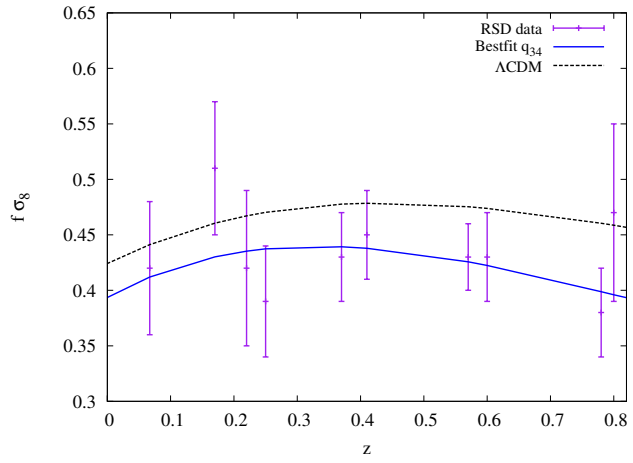

Figure 6.19: RSD measurements plotted against the theoretical predictions from the best-fit iVCDM model with $q_{34} = -0.128$ (blue) and a ΛCDM model ($q_{34} = 0$) with the same values of cosmological parameters (black).

My reference papers

10.1103/PhysRevLett.113.181301 V. Salvatelli, N. Said, M. Bruni, A. Melchiorri, D. Wands
"*Hints for a late interaction in the Dark Sector*" Phys. Rev. Lett. **113**, 181301 (2014) [arXiv:1406.7297v2 [astro-ph.CO]].

In preparation N. Said, V. Salvatelli, M. Bruni, A. Melchiorri, D. Wands
'*A complete analysis on interacting dark sector*'

Conclusions

To summarize, my Ph.D. work have been devoted to the study of the dark sector of the Universe, following the hints coming from the recently released measurements of different observables. Fundamental components of the Universe are in practise unknown, and it is in their properties that one has to look for answers to the discrepancies of the ΛCDM model predictions and the actual observations.

ΛCDM model has been indeed a satisfactory answer until we reached the present levels of accuracy. At this point the standard model seems no more capable of giving an overall agreement. Systematic effects in measurements and data analysis can indeed be responsible for these discrepancies, but the correctness of the a priori assumptions made on the dark components of the Universe must be doubted and demonstrated. The nature of these properties can be studied only in an indirect way, and thanks to the recent developments of Astrophysical observations we can rely now on different and powerful methods.

Bayesian statistics has been proved to be a great tool for Cosmological research, allowing robust parameter estimation of a selected model and the selection itself among different models. Monte-Carlo Markov Chains methods can implement the Bayesian analysis in a fast and reliable way, making possible to test the ΛCDM assumptions using several datasets combination.

My research faced the discrepancies in recent measurements, asking whether and which deviations from the standard model could resolve the tensions.

In Chapter 4 I reported all my research on neutrino properties, triggered by the inconsistencies in the CMB damping tail measurements of three different experiments (ACT, SPT and Planck). I have shown how the claim of SPT for a neutrino sum of the masses different from zero was most likely due to a wrong value of the lensing amplitude parameter, and how this parameter affects also the determination of the number of neutrino species in all the three experiments. I studied the clustering properties of the dark radiation, in terms of sound speed and viscosity, showing that non standard values are preferred if the lensing amplitude parameter is kept fixed to the

expected value of one. All of this seems to suggest that systematic effects are responsible for the disagreement among different experiments predictions of this amplitude, and that solving this issues can recover a good agreement between the standard model and the small scales measurements of the CMB. However, neutrino non standard properties can also cure the discrepancy between Deuterium abundance measurements from Astrophysical observations and the CMB predictions, as also non standard inflationary scenarios do.

In Chapter 5 I focus on my research on the temporal evolution of the dark energy EOS, that would be the best way to test the correctness of the cosmological constant solution. Using different probes that indicates different behaviours (BAO, SN, Hubble flow) I determined the values of this EOS in different red-shift bins, I applied the decorrelation method of the PCA and found a hint for a value lower than the standard at low red-shifts, where the precision of the measurements is higher. These results can be used to compare the actual value of the EOS with the one predicted from different dark energy and modified gravity models, in order to rule out classes of models or determine viable parameter ranges.

Finally, in Chapter 6 I exposed my conclusions about coupled dark sector scenarios, to solve the disagreement between CMB-predicted growth of structures and the actual value measured observing the clustering of the LSS. Following the results of a red-shift bin analysis, I determined a best-fit model characterised by an interaction among dark energy and dark matter starting below $z = 1$. I verified the robustness of this result in several ways and quantified the preference of this model over the ΛCDM and its massive neutrino extension (that also solves the tension between CMB and RSD data) using the Bayesian evidence.

At the end of it all the dark sector remains dark, but hopefully the final Planck release of CMB measurements and the forthcoming LSS observations will shed light on this shadowed part of our Universe.

Acknowledgments

I would like to thank all the people that, in minor or major ways, contributed to this achievement.

The first mention goes to my family, that with care and patience always supported me, in every way, in every challenge I took.

Thank you mum, for being always there and for reminding me my strength, thank you dad, for taking such good care of me and for reminding me what really matters in life, thank you Amira, for being such a perfect sister and drying away my tears, and thanks to all my beloved puppies, Luigi, Uma and Cinzia, for reminding me every day how beautiful the world is.

Beside family there are friends, that never left me alone, even in my worst periods, never forgot me, notwithstanding distances, and helped me in taking my decisions.

So thank you Silvia, Mari, Cecia and Lord, for being such good Friends and for always giving me a reason to be happy, that is your presence in my life.

Thank you Marco, for being always beside me, you know how important you are to me.

Thank you Chiara, Marghe and Stefano, for making my life so beautiful and easy with you nearby, you are the best atmates ever, but first of all you are best friends.

Thank you Sari and Dani, for giving me your time and smiles, I will never forget the way you took care of me when I mostly needed it.

Thank you Nicco, Bob and Seb, for making my days always better and my evenings always foolish, and for all the crazy conversations that we had.

Thank you Daniele and Florio for keeping our precious relation always alive.

Thank you Squenqui, Roscio, Alice, Sara, Vestaja, Almona, Bionda, Claudia piccola, Claudia alta, Salvatore, Mettiu, Ele, Giulio, Leonardo and Lollo, for making my life so funny.

Thank you Danae for sharing with me this unbelievable friendship that never get old, no matter what; thank you Claudia, for being my longest-time

best friend, and thank you Mele and Johnny for always having a hug to share with me.

Thank you Valentina for the time we spent together this year, you totally contributed to my survival with your presence and I am so happy to have shared that time with you!

Thank you Laura, Martina, Andrea and Eleonora for being such nice workmates and friends and thanks to Alessandro, Elena, Max and all the other people in the Lab for making me miss the place, despite the cryopump!

Thanks to my supervisor Alessandro that helped me in every way he could, thanks to Marco that took so much care of me and thanks to Luca for being the best I could hope for.

Thanks to all the other people with whom I cooperated, Matteo, Alessandra, Carlo and David, for being so nice with me.

Thanks to my teacher Angela and my dancers all, for making me rediscover how dance helps you see things clearly, and thanks to all the guys of the Insomnia-Lab, for having spent all those nights working side by side.

Thanks to the places that surrounded me, comforted me and also made me sad, because I remember all of them with love in the end.

Hard periods in life are unavoidable, and useful too, not only because you are pushed to think, learn and rediscover your strength, but also because when the pain is over you recognize the good part of them.

For this reason thank you Gino for the beautiful time spent together, and thank you Alessandro, for making me question my needs, and for all the precious moments we had.

At the end of it all, these years were tough, but also full of great moments that I will never forget. This is because of all the people that stepped on my way, that more or less contributed in their own way to create such a beautiful overall result. I surely forgot someone, I apologize for that.

Bibliography

[1] K. A. Olive; *The Violent Universe: The Big Bang*; CERN Yellow Report CERN-2010-002, 149-196; 2010.

[2] A. D. Dolgov; *Baryogenesis and cosmological antimatter*; AIP Conf. Proc. **1116**, 155; 2009.

[3] L. Amendola, S. Tsujikawa; *Dark Energy - Theory and Observation*; Cambridge University Press; 2010.

[4] G. Hinshaw et al.; *Nine-Year Wilkinson Microwave Anisotropy Probe (WMAP) Observations: Cosmological Parameter Results*; arXiv:1212.5226; 2012.

[5] P. A. R. Ade et al.; *Planck 2013 results. XV. CMB power spectra and likelihood*; arXiv:1303.5075; 2013.

[6] P. A. R. Ade et al.; *Planck 2013 results. XVI. Cosmological Parameters*; arXiv:1303.5076; 2013.

[7] P. A. R. Ade et al.; *Planck 2013 results. XX. Cosmology from Sunyaev-Zeldovich cluster counts*; arXiv:1303.5080; 2013.

[8] R.A. Battye et al.; *Evidence for massive neutrinos from CMB and lensing observations*; arXiv:1308.5870; 2013.

[9] B. Leistedt et al.; *No new cosmological concordance with massive sterile neutrinos*; arXiv:1404.5950; 2013.

[10] P. Giannone; *Elementi di Astronomia*; Pitagora Editrice Bologna; 2004.

[11] D. A. Howell; *A Review of Type Ia Supernovae as Stellar Endpoints and Cosmological Tools*; arXiv:1011.0441v1; 2010;

[12] L. Greggio; *The rates of type Ia supernovae*; A&A 441, 1055-1078; 2005.

[13] N. Suntzeff; *Supernovae and Supernova Remnants - Observation of Type Ia Supernovae*; Proceedings International Astronomical Union Colloquium 145, Xian, China; 1993.

[14] P. A. Pinto; *Type Ia Supernovae as Distance Indicators*; Steward Observatory, University of Arizona; 2003

[15] R. Amanullah et al.; *Spectra and Light Curves of Six Type Ia Supernovae at 0.511 ¡ z ¡ 1.12 and the Union2 Compilation*; Astrophys.J.716:712-738; 2010.

[16] D. J. Eisenstein et. al.; *Baryonic features in the matter transfer function*; Astrophys. J. **496**, 605; 1998.

[17] D. J. Eisenstein et al.; *On the Robustness of the Acoustic Scale in the Low-red-shift Clustering of Matter*; Astrophys. J. **664**, 660; 2007.

[18] C. Blake et al.; *The WiggleZ Dark Energy Survey: testing the cosmological model with baryon acoustic oscillations at z=0.6*; arXiv:1105.2862; 2011.

[19] A. Conley et al.; *Supernova Constraints and Systematic Uncertainties from the First 3 Years of the Supernova Legacy Survey*; ApJS, 192, 1; 2011.

[20] J. Guy et al.; *SALT2: using distant supernovae to improve the use of type Ia supernovae as distance indicators*; A& A 466,11-21; 2007.

[21] A. Conley et al.; *SiFTO: An Empirical Method for Fitting SN Ia Light Curves*; Astrophys. J., 681:482Y 498; 2008.

[22] M. Kowalski et al.; *Improved Cosmological Constraints from New, Old and Combined Supernova Datasets*; Astrophys. J. **686**, 749; 2008.

[23] J. Guy et al.; *SALT: A Spectral adaptive Light curve Template for Type Ia supernovae*; Astron. Astrophys. **443**, 781; 2005.

[24] N. Suzuki et al.; *The Hubble Space Telescope Cluster Supernova Survey: V. Improving the Dark Energy Constraints Above z¿1 and Building an Early-Type-Hosted Supernova Sample*; Astrophys. J. **746**, 85; 2012.

[25] F. Beutler et al.; *The 6dF Galaxy Survey: Baryon Acoustic Oscillations and the Local Hubble Constant*; Mon. Not. Roy. Astron. Soc. **416**, 3017; 2011.

[26] W. J. Percival et al.; *Baryon Acoustic Oscillations in the Sloan Digital Sky Survey Data Release 7 Galaxy Sample*; Mon. Not. Roy. Astron. Soc. **401**, 2148; 2010.

[27] L. Anderson et al.; *The clustering of galaxies in the SDSS-III Baryon Oscillation Spectroscopic Survey: Measuring D-A and H at z=0.57 from the Baryon Acoustic Peak in the Data Release 9 Spectroscopic Galaxy Sample*; arXiv:1303.4666 [astro-ph.CO], 2013.

[28] C. Blake et al.; *The WiggleZ Dark Energy Survey: Joint measurements of the expansion and growth history at z ¡ 1*; Mon. Not. Roy. Astron. Soc. **425**, 405; 2012.

[29] R.Tojeiro; *Understanding the Cosmic Microwave Background Temperature Power Spectrum*; lecture; 2006.

[30] M. Tegmark; *Doppler peaks and all that: cmb anisotropies and what they can tell us*; Proc. Enrico Fermi, Course CXXXII, Varenna; 1995.

[31] W. Hu et al.; *COSMIC MICROWAVE BACKGROUND ANISOTROPIES* Annu. Rev. Astron. Astrophys. 40: 171-216; 2002.

[32] G.E. Addison et al.; *Modelling the correlation between the thermal Sunyaev Zel'dovich effect and the cosmic infrared background*; arXiv:1204.5927; 2012.

[33] M. Zaldarriaga; *The polarization of the cosmic microwave background*; astro-ph/0305272; 2003.

[34] H. C. Chiang et al.; *Measurement of CMB Polarization Power Spectra from Two Years of BICEP Data*; Astrophys. J. **711**, 1123; 2010.

[35] P. A. R. Ade et al.; *Planck 2013 results. XVII. Gravitational lensing by large-scale structure* arXiv:1303.5077; 2013.

[36] E. Komatsu et al.; *Seven-Year Wilkinson Microwave Anisotropy Probe (WMAP) Observations: Cosmological Interpretation*; Astrophys. J. Supp. **192**, 1; 2011.

[37] J. L. Sievers et al.; *The Atacama Cosmology Telescope: Cosmological parameters from three seasons of data*; arXiv:1301.0824; 2013.

[38] Z. Hou et al.; *Constraints on Cosmology from the Cosmic Microwave Background Power Spectrum of the 2500-square degree SPT-SZ Survey*; arXiv:1212.6267; 2012.

[39] L. Samushia, et al.; *The Clustering of Galaxies in the SDSS-III Baryon Oscillation Spectroscopic Survey (BOSS): measuring growth rate and geometry with anisotropic clustering*; Mon. Not. Roy. Astron. Soc. **439**, 3504; 2014.

[40] W. J. Percival et al.; *The 2dF Galaxy red-shift Survey: Spherical harmonics analysis of fluctuations in the final catalogue*; Mon. Not. Roy. Astron. Soc. **353**, 1201; 2004.

[41] C. Blake et al.; *The WiggleZ Dark Energy Survey: the growth rate of cosmic structure since red-shift z=0.9*; Mon. Not. Roy. Astron. Soc. **415**, 2876; 2011.

[42] B. A. Reid et al.; *The clustering of galaxies in the SDSS-III Baryon Oscillation Spectroscopic Survey: measurements of the growth of structure and expansion rate at z=0.57 from anisotropic clustering*; arXiv:1203.6641; 2012.

[43] S. de la Torre et al.; *The VIMOS Public Extragalactic red-shift Survey (VIPERS). Galaxy clustering and red-shift-space distortions at z=0.8 in the first data release*; arXiv:1303.2622; 2013.

[44] A.G. Riess et al.; *A 3% Solution: Determination of the Hubble Constant with the Hubble Space Telescope and Wide Field Camera 3*; ApJ, 730, 119; 2011.

[45] M. Moresco et al.; *New constraints on cosmological parameters and neutrino properties using the expansion rate of the Universe to z 1.75*; JCAP07 053; 2012.

[46] R. Jimenez et al.; *Constraining Cosmological Parameters Based on Relative Galaxy Ages*; Astrophys.J. 573 37-42; 2002.

[47] A. Lewis et al.; *Efficient computation of CMB anisotropies in closed FRW models*; Astrophys. J. **538**, 473; 2000.

[48] C. P. Ma et al; *Cosmological perturbation theory in the synchronous and conformal Newtonian gauges*; Astrophys. J. **455**, 7; 1995.

[49] T. Padmanabhan; *After the First Three Minutes- The Story of Our Universe*; Cambridge University Press; 1996.

[50] M. D. Messier; *Review of neutrino oscllations experiments*; eConf C **060409**, 018; 2006.

[51] K. N. Abazajian et al.; *Cosmological and Astrophysical Neutrino Mass Measurements*; Astropart. Phys. **35**, 177; 2011.

[52] M. Shaposhnikov; *Dark Matter: The Case of Sterile Neutrino*; In *Rhodos 2006, The Identification of Dark Matter* 403-411; 2006.

[53] L. Bergstrom; *Dark Matter Evidence, Particle Physics Candidates and Detection Methods*; Annalen Phys. **524**, 479; 2012.

[54] M. Roos; *Dark Matter: The evidence from astronomy, astrophysics and cosmology*; arXiv:1001.0316; 2010.

[55] Volker Springel et al.; *Simulations of the formation, evolution and clustering of galaxies and quasars*; Nature, 435, 629; 2005.

[56] W. Rau; *Dark Matter Search Experiments*; Phys. Part. Nucl. **42**, 650; 2011.

[57] D. H. Weinberg et al.; *Observational Probes of Cosmic Acceleration*; Phys. Rept. **530**, 87; 2013.

[58] D. Rubin et al.; *Looking Beyond Lambda with the Union Supernova Compilation*; Astrophys.J.695:391-403; 2009.

[59] E. V. Linder; *The Dynamics of Quintessence, The Quintessence of Dynamics*; Gen.Rel.Grav.40:329-356; 2008.

[60] B. C. Paul et al.; *Accelerating Universe in Modified Theories of Gravity*; Phys. Rev. D **79**, 083534; 2009.

[61] W. Hu et al.; *A Parameterized Post-Friedmann Framework for Modified Gravity*; Phys. Rev. D **76**, 104043; 2007.

[62] W. Fang et al.; *Crossing the Phantom Divide with Parameterized Post-Friedmann Dark Energy*; Phys. Rev. D **78**, 087303; 2008.

[63] R. Trotta; *Bayes in the sky: Bayesian inference and model selection in cosmology*; Contemp. Phys. **49**, 71; 2008.

[64] A. Lewis et al.; *Cosmological parameters from CMB and other data: A Monte Carlo approach*; Phys. Rev. D **66**, 103511; 2002.

[65] A. Lewis; *Efficient sampling of fast and slow cosmological parameters*; Phys. Rev. D **87**, no. 10, 103529; 2013.

[66] A. Gelman et al.; *Inference from iterative simulation using multiple sequences*; Statistical Science **7**, 457–511; 1992.

[67] I. Verdinelli et al.; *Computing Bayes factors using a generalisation of the Savage-Dickey density ratio*; J. Amer. Stat. Assoc. 90 614–618; 1995.

[68] A. R. Liddle; *Information criteria for astrophysical model selection*; Mon. Not. Roy. Astron. Soc. **377**, L74; 2007.

[69] D. Huterer et al.; *Parameterization of dark-energy properties: A Principal-component approach*; Phys. Rev. Lett. **90**, 031301; 2003.

[70] D. Huterer et al.; *Uncorrelated estimates of dark energy evolution*; Phys. Rev. D **71**, 023506; 2005.

[71] R. de Putter et al.; *To Bin or Not To Bin: Decorrelating the Cosmic Equation of State*; Astropart. Phys. **29**, 424; 2008.

[72] G. Mangano et al.; *Relic neutrino decoupling including flavor oscillations*; Nucl. Phys. B **729**, 221; 2005.

[73] E. Calabrese et al.; *CMB Lensing Constraints on Dark Energy and Modified Gravity Scenarios*; Phys. Rev. D **80**, 103516; 2009.

[74] E. Di Valentino et al.; *Tickling the CMB damping tail: Scrutinizing the tension between the Atacama Cosmology Telescope and South Pole Telescope experiments*; Phys. Rev. D **88**, no. 2, 023501; 2013.

[75] N. Said et al.; *Planck constraints on the effective neutrino number and the CMB power spectrum lensing amplitude*; Phys. Rev. D **88**, no. 2, 023513; 2013.

[76] W. Hu; *Structure formation with generalized dark matter*; Astrophys. J. **506**, 485; 1998.

[77] M. Archidiacono et al.; *The Case for Dark Radiation*; Phys. Rev. D **84**, 123008; 2011.

[78] M. Gerbino et al.; *Neutrino Anisotropies after Planck*; Phys. Rev. D **88**, no. 6, 063538; 2013.

[79] F. Iocco et al.; *Primordial Nucleosynthesis: from precision cosmology to fundamental physics*; Phys. Rept. **472**, 1; 2009.

[80] O. Pisanti et al.; *PArthENoPE: Public Algorithm Evaluating the Nucleosynthesis of Primordial Elements*; Comput. Phys. Commun. **178**, 956; 2008.

[81] M. Pettini et al.; *A new, precise measurement of the primordial abundance of Deuterium*; Mon. Not. Roy. Astron. Soc. **425**, 2477; 2012.

[82] M. Tegmark; *Measuring the metric: A Parametrized postFriedmanian approach to the cosmic dark energy problem*; Phys. Rev. D **66**, 103507; 2002.

[83] G. -B. Zhao et al.; *Examining the evidence for dynamical dark energy*; Phys. Rev. Lett. **109** 171301; 2012.

[84] W. Hu et al.; *Models of f(R) Cosmic Acceleration that Evade Solar-System Tests*; Phys. Rev. D **76**, 064004; 2007.

[85] A. De Felice et al.; *Cosmological constraints on extended Galileon models*; JCAP **1203** 025; 2012.

[86] P. Brax et al.; *The Robustness of quintessence*; Phys. Rev. D **61** 103502; 2000.

[87] A. R. Liddle et al.; *A Classification of scalar field potentials with cosmological scaling solutions*; Phys. Rev. D **59** 023509; 1999.

[88] A. Hojjati et al.; *Cosmological tests of General Relativity: a principal component analysis*; Phys. Rev. D **85** 043508; 2012.

[89] Y. Wang et al.; *Observational Constraints on Dark Energy and Cosmic Curvature*; Phys. Rev. D **76**, 103533; 2007.

[90] B. Hu et al.; *Effective Field Theory of Cosmic Acceleration: an implementation in CAMB*; Phys. Rev. D **89**, 103530; 2014.

[91] O. F. Piattella et al.; *Unified Dark Matter models with fast transition*; JCAP **1001**, 014; 2010.

[92] M. Bruni et al.; *Phenomenological models for Unified Dark Matter with fast transition*; Mon. Not. Roy. Astron. Soc. **431**, 2907; 2013.

[93] D. Wands et al.; *Inhomogeneous vacuum energy*; Class. Quant. Grav. **29**, 145017; 2012.

[94] C. Quercellini et al.; *Late universe dynamics with scale-independent linear couplings in the dark sector*; Phys. Rev. D **78**, 063527; 2008.

[95] M. B. Gavela et al.; *Dark coupling*; JCAP **0907**, 034; 2009.

[96] R. A. Daly et al.; *Cosmological Studies with Radio Galaxies and Supernovae*; Astrophys. J. **691**, 1058; 2009.